



DISSERTATION

Classical many-body dynamics: Clusters in strong laser fields

ausgeführt zum Zwecke der Erlangung des akademischen Grades eines Doktors der technischen
Wissenschaften unter der Leitung von

Thomas Brabec

*Center for Photonics Research, University of Ottawa,
150 Louis Pasteur, Ottawa, ON, K1N 6N5 Canada*

eingereicht an der Technischen Universität Wien
Fakultät für Elektrotechnik und Informationstechnik
von

Christian Jungreuthmayer

*Matrikelnummer 9226118
Gugitzgasse 6/12/2, A-1190 Wien, Austria*

Wien, im Februar 2005

Abstract

Many interesting effects result from the ionization of atoms by very intense, ultrashort, laser pulses. For an ensemble of a large number of atoms in a strong laser field, macroscopic dynamical effects emerge in the resulting ionized plasma that are a direct result of microscopic interactions, yet cannot be foreseen by understanding the atomic system alone. The standard computational method of addressing many-particle dynamics in a strong laser field involves explicitly calculating the interactions between each particle in the system with every other particle, leading to a computational load that scales as the square of the total number of particles. The largest systems that can be reasonably addressed with this method can include no more than 1000 atoms.

In this thesis two computational approaches are used to increase the computable system size. First, a 3d microscopic particle in cell (MPIC) code is introduced which takes into account all important microscopic effects in the evolution of laser driven large clusters. Second, a treecode has been implemented which overcomes the unfavorable N^2 scaling of conventional molecular dynamics (MD) simulations by approximating the force of a group of distant particles by multipole expansion. Both approaches have their advantages and disadvantages and differ in their range of application.

The MPIC code is an enhancement of regular particle in cell (PIC) codes. Regular PIC codes solve the Maxwell equations and the relativistic classical equations of motion on a stationary grid using the mean field approximation. The charged particles are represented by boxes with macroscopic dimensions that represent the average over many particles. As a result, microscopic effects such as inverse bremsstrahlung heating, impact ionization, electron-electron scattering, electron-ion scattering, and charge enhanced ionization (CEI) cannot be taken into account. In the MPIC code the box size is shrunk to the order of 1 a.u. containing only one charged particle. In this limit, the microscopic interaction of all charged particles are taken care of by the PIC formalism. The MPIC code is inherently relativistic and opens the possibility to look microscopically at relativistic plasma dynamics. It contains no free parameters and presents a virtual experiment. To test its reliability recent experiments reporting an asymmetric explosion of Ar and Xe clusters with $N \geq 10.000$ have been calculated. The calculated spectra and angular distributions of electrons and ions are found to be in good agreement with the experiments. The MPIC simulations reveal the first complete picture of the explosion of large clusters with several 10.000

atoms.

Treecodes use the fact the the force of a group of distant particles can be well approximated by a low-order multipole expansion. Computing time of a treecode scales with $N \log(N)$ compared to the N^2 scaling of conventional MD codes. In this work a treecode has been used to simulate a recent experiment performed with the first free electron laser at DESY in Hamburg. The calculated charge state distribution and energy absorption rates show a good agreement with the experiment and reveals that the electron heating is a consequence of the strongly coupled plasma dynamics in which collisional processes are strongly modified.

Understanding the dynamics of cluster explosions can be seen as a stepping stone to understanding intense laser-induced phase transitions in solids. By further extending these novel numerical tools, it will be possible to address the dynamics of macroscopic systems – that is, with a size of the order of the laser wavelength – in the near future.

**If at first the idea is not absurd,
then there is no hope for it.**

Albert Einstein

**The three chief virtues of a programmer are:
Laziness, Impatience and Hubris**

Larry Wall

Acknowledgments

First and foremost I would like to thank my supervisor Thomas Brabec for his support and guidance and for showing me the qualities an outstanding physicist must have.

Many thanks to Armin Scrinzi, Siegfried Benkner, Vladimir Krainov, and Béla Joós for their help and support.

My coworkers of the Photonics Center at the University of Ottawa were often helpful and always patient when I couldn't hide my sympathy for free and open source software. I am sure some of them had a hard time when I banned proprietary software from the lab in my function as computer and network administrator. Alexander Pegarkov, Carlos Destefani, Neera Treesler, Zhongxi Zhang, Adrian Pegoraro, Chris McDonald, Julien Bertrand, Patrick Bergeron - thank you.

I also would like to thank Martin Kenward and Nabil Benabbou for pretending to listen to me and for sharing the joy of using Linux.

Thanks also to my coworkers in Vienna: Christian Fabian, Michael Geissler, and Nenand Milosevic.

I owe a debt of gratitude to my friends and coworkers Lora Ramunno, Markus Kitzler, and Jürgen Zanghellini for their help, support and honesty. Special thanks to Jürgen for trying to improve my chess and sharing a passion for Earl Grey tea.

My gratitude also to Marianne O'Sullivan, Ania and Dariusz Burzynski for their friendship, kindness and help: Our stay in Canada would not have been the same without you.

I would also like to take this opportunity to say thank you to all free software/open source software developers. You have changed the world. I do not even want to imagine how my work day would look without all the excellent programs you have written. Keep up the good work.

I am extremely grateful to my parents-in-law, Christa and Gerhard Illetschko, for their never-ending support, their understanding, and their interest in my work.

Very special thanks to my parents Margrit and Horst Jungreuthmayer - thank you for everything.

Most of all I wish to thank my wife Daniela and my little daughter Annika. Annika for cheering up my day and showing me what is really important in life

after a hard day in the office. To Daniela: It is impossible to express in words how deeply grateful I am to know you and to enjoy your company. Thank you.

Contents

1	Introduction and basics	1
1.1	Motivation and goals	1
1.2	Clusters	2
1.2.1	Definition	2
1.2.2	Binding	2
1.2.3	Cluster dynamics	3
1.3	Plasma	5
1.3.1	Definition	5
1.3.2	Heating mechanism	6
2	Models	8
2.1	Particle in cell codes	8
2.1.1	Regular PIC codes	8
2.1.2	Microscopic PIC code	11
2.1.3	Parallelization	17
2.1.4	Implementation	17
2.1.5	Special hardware	17
2.2	Treecode	19
2.2.1	Principles	19
2.2.2	Implementation	32
2.2.3	Parallelization	32
2.2.4	Future improvements	33
2.3	Comparison of treecodes with MPIC Codes	33
2.3.1	Advantages of MPIC codes	33
2.3.2	Advantages of treecodes	33
2.3.3	Drawbacks shared by both methods	35
2.4	Computer equipment	35
2.5	Cross sections and ionization potentials	36
3	Asymmetric explosion of large rare gas clusters	37
3.1	Introduction	37
3.2	Results	38
3.3	Heating mechanism	44
3.4	Conclusion	44

4	Charge state distribution of ions formed in Coulomb explosions of Argon clusters in intense laser fields	47
4.1	Introduction	47
4.2	Experimental and theoretical methods	49
4.3	Results and discussion	50
4.4	Conclusion	53
5	Plasma physics in the strong coupling regime: Intense soft X-ray cluster interaction	55
5.1	The Experiment, and What is known	55
5.2	Results	56
5.3	Conclusion	65
6	Conclusion and outlook	66
A	<i>N log(N)</i>-scaling of treecodes	68
B	Derivation of vicinity probability	71
C	Common abbreviations	75
D	Conversion table	77
E	Physical constants	78
E.1	Atomic units	78
E.2	SI units	78
E.3	cgs units	79
	List of figures	80
	List of tables	81
	Bibliography	82

Chapter 1

Introduction and basics

This chapter is divided into 3 sections. The first section is about the motivation and goals of this work. Sections two and three of the chapter give an introduction to and general overview of the two major concepts used throughout this thesis, namely clusters and plasmas. The part about clusters deals with the definition, classification, binding mechanism, geometrical structures, dynamics, ionization, and polarization of atomic clusters. The section about plasmas also provides a definition and is mainly about the mechanisms of plasma heating, which are relevant for this work.

1.1 Motivation and goals

Virtually since the invention of lasers [1] the field of laser-matter-interaction has been subject of intensive research [2]. Laser-matter-interaction has strongly influenced many fields of science such as physics, chemistry, biology and medicine [3]. It has innumerable applications in technology and has changed our everyday's live. One of the subfields of laser-matter-interaction is the interaction of intensive ultrashort laser pulses with atomic clusters. Ultrashort laser pulses are characterized by their ability to create peak intensities which easily reach hundreds of Terawatts per square centimeter [4, 5]. These intensities are the reason for numerous effects which are unique to ultrashort laser pulses. In addition to the pure fundamental physical interests they also have a variety of technological applications e.g. material processing, micromachining [6], spectroscopy [7], X-ray generation [8], nuclear fusion [9] and many more. Clusters on the other hand are characterized by a unique set of features which cannot be found in atomic/molecular physics nor solid state physics [10]. The combination of ultrashort laser pulses and atomic clusters offers the possibility to gain insight into new effects, which cannot be observed anywhere else in physics.

There are many ways to investigate theoretically the dynamics of clusters irradiated by intense laser pulses. There are quantum mechanical and classical approaches which can both be applied to numerical or analytical methods. One

main advantage of investigating the interaction of ultrashort laser pulses with atomic clusters is that clusters can be easily created in experiments and that they are still small enough to be numerically simulated by diverse N-body solvers. Furthermore, the simulation time is rather short because of the shortness of the pulse. To have access to experimental data and be able to calculate the N-body problems for these experiments allows us to get a complete picture of the dynamics of clusters exposed to intensive ultrashort laser pulses. However, these simulations are still very challenging and require efficient computer programs and high performance computing equipment.

Throughout this thesis two numerical tools are introduced to perform simulations of the interaction of ultrashort laser pulses with rare gas clusters, namely MPIC [11] codes and treecodes [12]. Both methods are described in detail in chapter 2. They have their advantages and disadvantages and hence differ in their range of applications. The final goal of N-body solvers in laser-matter-interaction is to microscopically simulate macroscopic systems as solids. The investigation of clusters can be seen as the stepping stone to this final goal.

1.2 Clusters

1.2.1 Definition

According to the Concise Oxford Dictionary clusters are defined as "a group of similar things" [13]. In this thesis clusters are aggregates of atoms (or molecules) containing between 3 and up to 10^7 atoms. In atomic and molecular physics systems usually have less than a few hundreds of constituents, whereas in solid state physics samples are virtually infinite. The size of clusters can be varied between atoms and bulk. Clusters have properties intermediate between those of isolated atoms or molecules and solid state materials. Hence they can bridge the gap between atomic/molecular physics and solid state physics. Clusters are a species of their own which show physical effects unknown to atoms/molecules and solid states. These effects have created a new field: cluster physics, which combines the expertise of various fields of physics and chemistry. The study of clusters has become an increasingly active research field in recent years (since ca. 1980). This activity is not only based on the potential technological interests in cluster as in the field of material science and the design of new materials, photography, and artwork, but also on the fundamental physical point of view [10].

1.2.2 Binding

Binding in clusters can be classified into four types: ionic, covalent, metallic, and van-der-Waals bonding (for details see 1.1). Throughout this thesis rare gas clusters are used for the numerical experiments. Rare gas clusters, as e.g. Ar, are of the van-der-Waals type. Figure 1.1 shows the geometrical icosahedral configuration of an Ar_{561} cluster. If an Argon cluster contains more than $N =$

Table 1.1: Classification of binding in clusters (from Reinhard and Suraud [10])

Type	Examples	Nature of binding	Binding energy
Ionic clusters	$(\text{NaCl})_n, \text{Na}_n\text{F}_{n-1}, \dots$	Ionic bonds Strong binding	$\sim 2 - 4 \text{ eV}$
Covalent clusters	$\text{C}_{60}, \text{S}_n, \dots$	Covalent bonding Strong binding	$\sim 1 - 4 \text{ eV}$
Metal clusters	$\text{Na}_n, \text{Al}_n, \text{Ag}_n, \dots$	Metallic bond Moderate to strong binding	$\sim 0.5 - 3 \text{ eV}$
van der Waals	Rare gas clusters $\text{Ar}_n, \text{Xe}_n, \dots$	Polarization effects Weak binding	$\lesssim 0.3 \text{ eV}$

Table 1.2: Structural data of condensed rare gases (from [14])

	${}^4\text{He}_{\text{solid}}$	Ne	Ar	Kr	Xe
atomic number	4	20	40	84	132
crystal structure	hpc	fcc	fcc	fcc	fcc
density of particle [$10^{22}/\text{cm}^3$]	2.7	4.54	2.67	2.22	1.72
avg. next neighbor distance [\AA]	3.57	3.16	3.75	3.98	4.34

750 particles then the cluster atoms form a fcc (face-centered cubic) lattice [13]. Rare gas clusters correspond to a closed atomic shell, which means atoms keep their electrons tightly bound. Hence, they can be simulated by effective atom-atom potentials, which are simple to use.

Structural and physical data

The key feature of clusters is their size. Reinhard and Suraud [10] and Bergman and Schäfer [13] propose the following classification:

1. **Very small cluster or microcluster**, $3 \leq N \leq 20$. For $N \leq 12$ all atoms are on the surface. Concepts and methods of molecular physics are still useable.
2. **Small cluster**, $20 \leq N \leq 500$. Molecular concepts loose their usability.
3. **Large cluster**, $500 \leq N \leq 10^7$. Gradual change to features of solids.

1.2.3 Cluster dynamics

One major field of cluster physics deals with cluster dynamics. As in atomic and molecular physics, studies of dynamics of clusters were mainly driven by the rapid progress of laser technology. Especially the newly developed high-power ultrashort laser pulses with field strengths that exceed the electric field strength

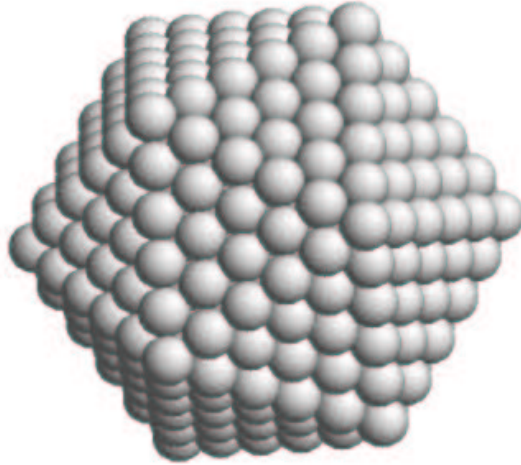


Figure 1.1: Illustration of the geometrical configuration (icosahedral) of an Ar₅₆₁ cluster (from [13]).

in an atom and the generation of shorter and shorter pulses [15] boosted the field of cluster dynamics. Laser-heated clusters explode producing x-ray and extreme ultraviolet (XUV) radiation [16] and energetic particles [17]. The dynamics of exploding clusters also give rise to interesting non-linear optical effects such as harmonic generation [18].

Ionization of clusters

In this thesis the concept of *inner* and *outer ionization* [19] is used. *Inner ionization* is the ionization of an electron from its mother atom or mother ion, whereas *outer ionization* is the process of an electron leaving the cluster as a whole.

Polarizability of ionized clusters

A rare-gas cluster containing electrons and ions resembles a metal. The plasma electrons can move freely. If the electrons are driven by a laser electric field they are pushed up and down along the laser polarization axes. The ion movement caused by the laser electric field can be neglected because of the high ion mass. This up and down pushing of the electrons against the ions results in a polarization. On one side the electron density is enhanced while at the same time an electron depletion occurs on the other side (see figure 1.2). In the area where electrons can be found they shield the electric fields of the ions, whereas

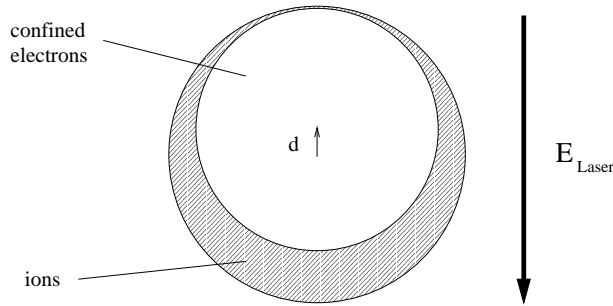


Figure 1.2: Polarization of a spherical cluster in the presence of an electric field. The shaded circle represents the ion bulk. The inner circle marks the electron cloud, which is displaced by d . d is the distance between the centers of the ion and electron spheres.

in areas where electron depletion occurs the electric field acting on the ions can reach much higher values than the driving laser electric field.

1.3 Plasma

1.3.1 Definition

The word *plasma* has a Greek root ($\pi\lambda\alpha\sigma\mu\alpha$) which means "formed" or "molded" (the word *plastic* shares this root) and has a few definitions [20]:

- in geology, a green type of chalcedony
- in medicine, the fluid part of blood (blood plasma)
- lymph or milk
- an ionized gas

In physics and chemistry, plasma is an energetic gas-phase state of matter in which some or all of the electrons in the outer atomic orbitals have become separated from the atom or molecule. The result is a collection of ions and electrons which are no longer bound to each other. This state of matter was first identified by Sir William Crookes in 1879 and dubbed plasma by Irving Langmuir. Since a plasma is a gas containing free ions and electrons it is capable of conducting electric currents. There may also be many neutral particles, as is the case for the ionosphere. A plasma can be produced from a gas if enough energy is added to cause the electrically neutral atoms of the gas to split into positively and negatively charged atoms and electrons. One way to produce a plasma from a neutral gas is by optical-field-induced ionization (OFI). Plasma is often considered the fourth state of matter (beside solid, liquid, and gas).

Most of the matter in the Universe is in the plasma state. The plasmas in nature and the man-made plasmas cover an extremely wide range of physical parameters like temperature, particle density and plasma generated magnetic field strengths.

1.3.2 Heating mechanism

The mechanism of heat transport in laser produced plasmas has been a topic of extensive research [21]. Several mechanisms can lead to heating of OFI plasmas, including above-threshold-ionization, collisional heating (inverse bremsstrahlung), stimulated Raman or Compton scattering, and space-charge or plasma oscillations [22]. Heating processes relevant for this work are briefly described in the following section. All of the mechanisms described in this chapter are well known. In chapter 3 and 5 two so far unknown heating mechanisms are introduced.

Single free electron exposed to a laser electric field

Following force acts on a single free electron with an original velocity \mathbf{v}_0 exposed to a laser electric field $\mathbf{E} = \mathbf{E}(t)$

$$\mathbf{F}(t) = e \mathbf{E}(t), \quad (1.1)$$

if the non-relativistic case is considered and therefore the magnetic field can be neglected. After the laser pulse the electron velocity is given by

$$\mathbf{v} = \int_0^T \frac{e}{m_e} \mathbf{E}(t) dt + \mathbf{v}_0, \quad (1.2)$$

if the laser pulse is defined from $t = 0$ to $t = T$. Since the dc-component of the field strength of laser pulses $\int_0^T \mathbf{E}(t) dt$ always equals zero [15, page 581] a single free electron cannot gain energy by being exposed to a laser pulse.

Above Threshold Ionization (ATI)

In the case of single photon or multi photon ionization ATI is a strong-field phenomenon in which an atom or ion absorbs more photon energy than the necessary amount to ionize. This extra energy is given by $E_{el} = n E_{photon} - I_p$, where E_{el} is the energy of the newly created electron, n is the number of absorbed photons, E_{photon} is the energy of the photons, and I_p is the ionization potential of the atom or ion.

In the case of tunnel ionization the electron is created with energy zero [23], then the electron is accelerated by the laser electric field. Most of the electron energy during the laser pulse comes from the quiver motion in the laser field and is returned to the field once the pulse passes. The relatively small residual energy after the pulse has left is the ATI energy [24]. The magnitude of the energy acquired during the ionization process is determined by the exact phase

of the electric field at which the electron is freed [25]. Consider an electron that is created at rest at time t_0 in an electric field $E_x = E_0 \sin \omega t$. The electron motion is given by [26]

$$\dot{x} = \frac{eE_0}{m\omega}(\cos \omega t - \cos \omega t_0) \quad (1.3)$$

and the corresponding average kinetic energy is

$$\frac{1}{2}m \langle \dot{x}^2 \rangle = \frac{e^2 E_0^2}{4m\omega^2}(1 + 2 \cos^2 \omega t_0). \quad (1.4)$$

The first term in the parenthesis is the energy of the oscillatory motion and the second term is the energy of the direct translation motion. The second term represents the surplus electron energy, in excess of the quiver energy, and is what has come to be known as the ATI energy [26]. If the ionization occurs when $E_0 \sin \omega t$ is maximum, i.e. when $\omega t_0 = \pi/2$, then the electron has no energy other than its quiver energy E_q . On the other hand, an electron ionized at some arbitrary phase mismatch $\Delta\varphi$ will acquire a residual kinetic energy $E_{ati} = E_q \cos^2 \Delta\varphi$.

Inverse Bremsstrahlung Heating (IBH)

Inverse bremsstrahlung (IBS) is the absorption of a photon by an electron in the field of a nucleus or an atomic ion. The total rate of inverse bremsstrahlung is equal to the difference between the rate w_e of stimulated emission and the rate w_a of stimulated absorption. The averaged rate over the direction of the final electron momentum p_f and over the angle between the initial electron momentum p_i and the polarization of the electric field is given by [27]

$$w_T \equiv w_e - w_a = -\frac{4\pi n_i \epsilon^2 Z^2}{3p_i^3 \omega^3} < 0. \quad (1.5)$$

Here n_i is the ion density and Z is the charge state of the ions. ω and ϵ are the frequency and the electric field strength of the linearly polarized light, respectively. For a detailed description of electron heating through inverse bremsstrahlung refer to [21]. Equation 1.5 is valid for rapid electrons, whereas the averaged rate for slow electrons is given by [28]

$$w_T \equiv w_e - w_a = -\frac{2\pi^2 n_i \epsilon^2 Z^2}{15 \cdot 3^{5/6} p_i \omega^2} \left(\frac{2}{Z\omega} \right)^{2/3} \frac{\Gamma(\frac{1}{3})}{\Gamma(\frac{2}{3})} < 0. \quad (1.6)$$

The conclusion of equations 1.5 and 1.6 is that the larger the ion density, the charge state of the ions and the laser intensity are the stronger is the electron heating. On the other hand, the heating is reduced by a larger laser frequency and larger initial momentum of the electrons.

Chapter 2

Models

In this chapter two numerical tools for investigating the interaction of ultra short laser pulses with clusters are introduced: microscopic particle in cell (MPIC) codes and treecodes. In sections 1 and 2 the theoretical background of both methods is described in detail. Section 3 of this chapter compares MPIC codes with treecodes. Section 4 is about the computer equipment used throughout this thesis and section 5 lists some references where physical data like cross sections and ionization potentials for atoms and ions can be found.

2.1 Particle in cell codes

Particle codes [29] and 3d particle in cell (PIC) codes have been used for several years to simulate laser plasma interactions in the non-relativistic and relativistic regime [30, 31]. PIC-Codes are also used for investigating the interaction of laser pulses with atomic and molecular clusters [32]. However, these simulations are based on the mean field approximation which lacks simulation of microscopic effects like inverse bremsstrahlung, impact ionization, and scattering. In this chapter a microscopic particle in cell (MPIC) code is introduced which overcomes the limitations of regular PIC-codes.

2.1.1 Regular PIC codes

PIC codes simulate the relativistic motion of charged particles in a self-consistently calculated electromagnetic field [33]. The volume of a PIC simulation is subdivided into a stationary grid of rectangular prisms. Electric field values and current densities are defined at the centers of the surface of the grid cells. Magnetic field values are defined at the centers of the edges of the grid boxes [34, page 76] as shown in figure 2.1. In PIC-codes particles are represented by charged boxes. These boxes may be located at arbitrary places and have the same size and shape as the stationary grid boxes [35]. Particles can move in the simulation volume driven by an electromagnetic field.

The electromagnetic field values are updated every timestep by solving Maxwell's equations of vacuum [36, page 2].

$$\nabla \times \mathbf{B} - \frac{1}{c} \frac{\partial \mathbf{E}}{\partial t} = \frac{4\pi}{c} \mathbf{J} \quad (2.1)$$

$$\nabla \times \mathbf{E} + \frac{1}{c} \frac{\partial \mathbf{B}}{\partial t} = 0 \quad (2.2)$$

$$\nabla \cdot \mathbf{E} = 4\pi\rho \quad (2.3)$$

$$\nabla \cdot \mathbf{B} = 0 \quad (2.4)$$

Implicitly included in the Maxwell's equations is the continuity of the equation for charge density and current density

$$\frac{\partial \rho}{\partial t} = -\nabla \cdot \mathbf{J} \quad (2.5)$$

The dynamic problem of field evolution can be solved by means of the local equations 2.1 and 2.2 alone after solving the divergence equations 2.3 and 2.4 only as initial conditions [33].

Discretization of equation 2.1 for the grid box at position (i, j, k) of a 3d

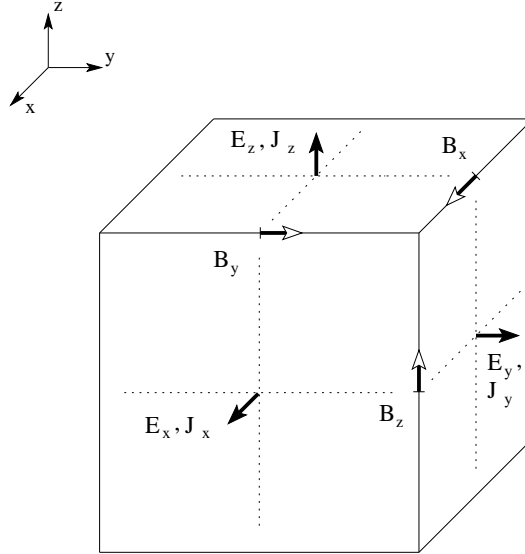


Figure 2.1: Position of electric and magnetic field values on a PIC grid box.

simulation volume results in

$$E_x^{t+\Delta t}(i, j, k) = E_x^t(i, j, k) - 4\pi\Delta t J_x^t(i, j, k) + c\Delta t \left[\frac{B_z^t(i, j, k) - B_z^t(i, j-1, k)}{h_y} - \frac{B_y^t(i, j, k) - B_y^t(i, j, k-1)}{h_z} \right] \quad (2.6)$$

$$E_y^{t+\Delta t}(i, j, k) = E_y^t(i, j, k) - 4\pi\Delta t J_y^t(i, j, k) + c\Delta t \left[\frac{B_x^t(i, j, k) - B_x^t(i, j, k-1)}{h_z} - \frac{B_z^t(i, j, k) - B_z^t(i-1, j, k)}{h_x} \right] \quad (2.7)$$

$$E_z^{t+\Delta t}(i, j, k) = E_z^t(i, j, k) - 4\pi\Delta t J_z^t(i, j, k) + c\Delta t \left[\frac{B_y^t(i, j, k) - B_y^t(i-1, j, k)}{h_x} - \frac{B_x^t(i, j, k) - B_x^t(i, j-1, k)}{h_y} \right], \quad (2.8)$$

where c is the velocity of light in vacuum and h_x , h_y and h_z is the length of a grid box in x , y and z direction, respectively.

Similarly we obtain for the discretization of equation 2.2

$$B_x^{t+\Delta t}(i, j, k) = B_x^t(i, j, k) - c\Delta t \left[\frac{E_z^t(i, j, k) - E_z^t(i, j-1, k)}{h_y} - \frac{E_y^t(i, j, k) - E_y^t(i, j, k-1)}{h_z} \right] \quad (2.9)$$

$$B_y^{t+\Delta t}(i, j, k) = B_y^t(i, j, k) - c\Delta t \left[\frac{E_x^t(i, j, k) - E_x^t(i, j, k-1)}{h_z} - \frac{E_z^t(i, j, k) - E_z^t(i-1, j, k)}{h_x} \right] \quad (2.10)$$

$$B_z^{t+\Delta t}(i, j, k) = B_z^t(i, j, k) - c\Delta t \left[\frac{E_y^t(i, j, k) - E_y^t(i-1, j, k)}{h_x} - \frac{E_x^t(i, j, k) - E_x^t(i, j-1, k)}{h_y} \right]. \quad (2.11)$$

Velocity and position of charged particles are updated with each timestep of the simulation by applying the Lorentz force

$$\mathbf{F} = q(\mathbf{E} + \frac{\mathbf{v}}{c} \times \mathbf{B}), \quad (2.12)$$

which is the force acting on the point charge q in the presence of electromagnetic fields [36, page 3]. Driven by the Lorentz force, charged particles move in the simulation volume (see figure 2.2) and cause a current at each boundary they pass through. The 2d example in figure 2.3 shows a particle which creates a current on seven boundaries. Since current density in the discrete case is represented by the motion of charge into or out of a grid box, it can be seen by the divergence equation 2.5 that each boundary will be swept over by an area of the square charge that exactly corresponds to the current in a given direction into or out of a cell [33].

The considerations given above result in program flow as shown in figure 2.4. After the initialization of electromagnetic fields, current densities, particle positions, and velocities, the program enters the timestep loop. With each

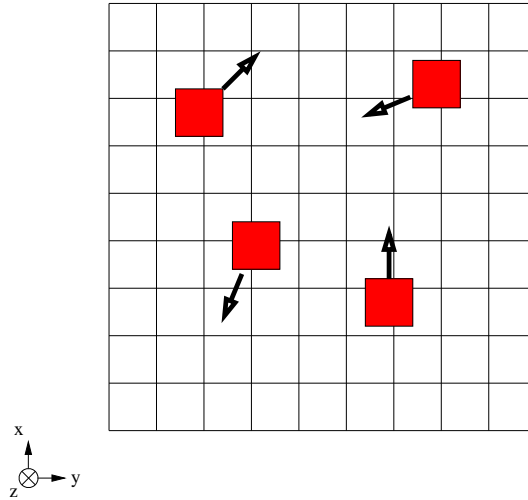


Figure 2.2: Charged particles with square cross-section moving in simulation volume.

timestep the electromagnetic field is updated for each cell by solving equations 2.6 - 2.11. After the field update the new particle velocities and positions are determined by using the Lorentz force (2.12). The motion of particles creates a current density on the boundaries. The current density is calculated by adding up the charges that pass through each boundary. The current density values are used in the next timestep to update the electric field. Hence, in PIC simulations matter acts on the electromagnetic field only via the current.

The laser pulse is fed into the simulation volume by defining the electromagnetic field values at the front plane of the simulation volume. The laser pulse automatically propagates into the volume by solving equations 2.6 - 2.11. The electromagnetic field values at the front plane vary with each timestep according to the spatial profile and time evolution of the laser pulse.

2.1.2 Microscopic PIC code

In regular PIC codes charged particles are represented by boxes with macroscopic dimensions that represent the average over many particles. As a result, microscopic effects such as inverse bremsstrahlung heating, impact ionization, and charge enhanced ionization cannot be taken into account. In the MPIC code the box size is shrunk to the order of 1 a.u. containing only one charged particle. In this limit, the microscopic interactions of all charged particles are taken care of by the PIC formalism.

The MPIC code calculates the classical dynamics of all charged particles. Quantum mechanical phenomena, such as ionization, have to be added. In the next four subchapters the implementation of tunnel ionization, above barrier

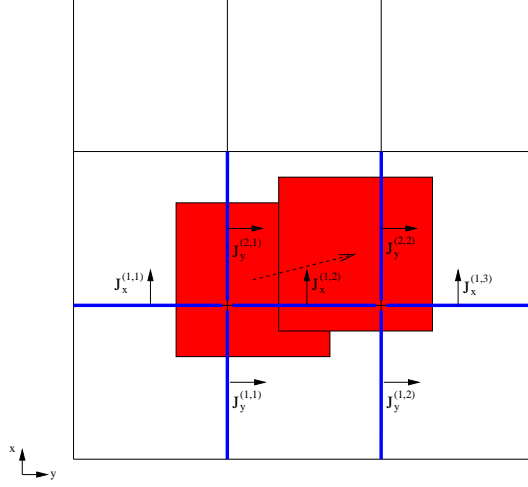


Figure 2.3: A moving particle creates an electric current at each grid box surface it sweeps over.

ionization, impact ionization, and single photon ionization is described. These four types of ionization are so-called inner ionization processes (see chapter 1.2.3). Outer ionization of electrons is described by classical mechanics.

Tunnel ionization

An electric field acting on an atom is bending the Coulomb potential. If the electric field is sufficiently high the electron will be able to tunnel through the Coulomb barrier (see figure 2.5). This mechanism is called tunnel ionization or (optical) field ionization. The electron is born at the position $r_b = I_p/E$ with a kinetic energy $E_{kin} = 0$. The ionization of an atom in an intense laser field has been investigated extensively in the last decades, both theoretically and experimentally. One of the commonly used models for calculating the ionization rate is the so-called ADK (Ammosov-Delone-Krainov) model [37]. This model is based on the ionization rate of a hydrogenlike atom in a static electric field, with modifications for real many-electron atoms [38].

The rate of tunnel ionization using the quasi-static approximation is [39]

$$\begin{aligned}
 W_{qs} = & A_{n^*,l^*} B_{l,|m|} I_p \left(\frac{2(2I_P)^{3/2}}{E_0 f(t) \cos(\omega_L t + \phi_0)} \right)^{2n^* - |m| - 1} \\
 & \times \exp \left(- \frac{2(2I_P)^{3/2}}{3E_0 f(t) \cos(\omega_L t + \phi_0)} \right). \quad (2.13)
 \end{aligned}$$

Here E_0 is the amplitude, $f(t)$ is the envelope, w_L is the frequency of the laser field, and ϕ_0 is the absolute phase. The effective principal quantum number

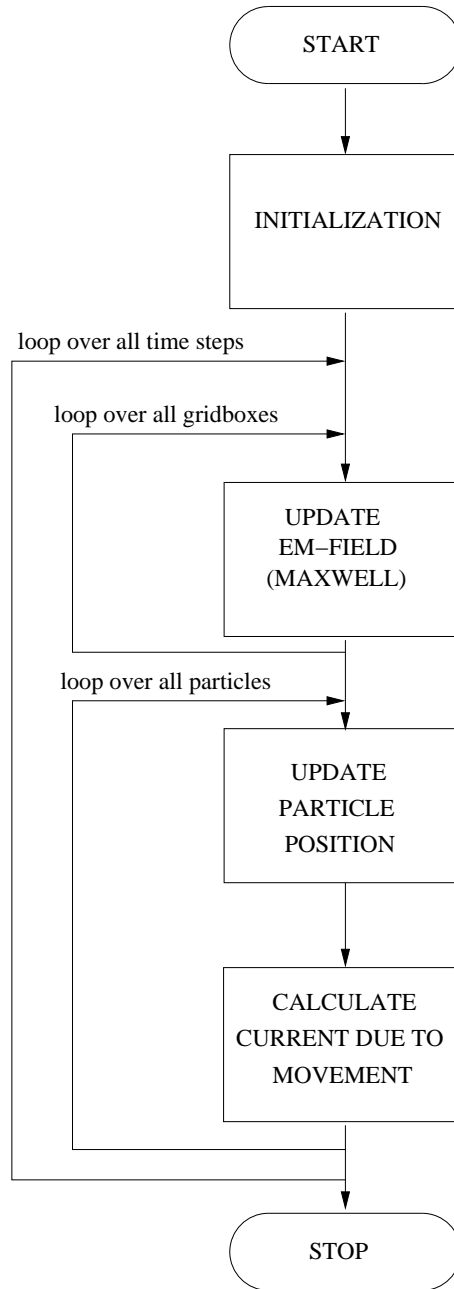


Figure 2.4: Flow chart of a PIC simulation.

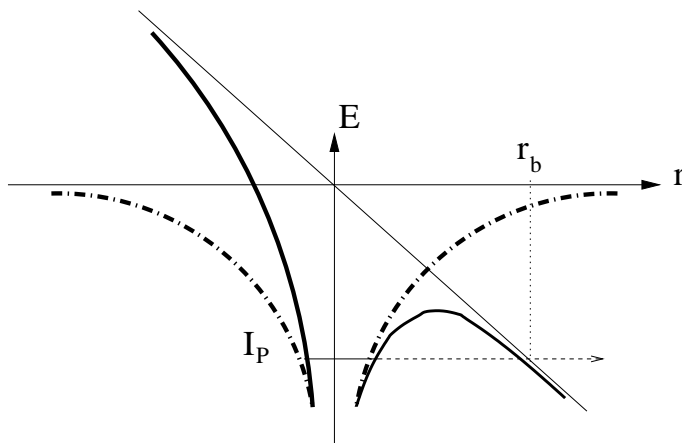


Figure 2.5: Schematic illustration of tunnel ionization. At a sufficiently high field strength the Coulomb barrier becomes narrow and allows tunneling ionization.

$n^* = Z/\sqrt{2I_P}$ (Z is the ion charge) and the effective angular quantum number l^* is given by $l^* = 0$ for $l^* \ll n$ and $l^* = n^* - 1$ otherwise [40]. m represents the magnetic quantum number. The coefficients A_{n^*,l^*} and $B_{l,|m|}$ are

$$A_{n^*,l^*} = \frac{2^{2n^*}}{n^* \Gamma(n^* + l^* + 1) \Gamma(n^* - l^*)}, \quad (2.14)$$

$$B_{l,|m|} = \frac{(2l+1)(l+|m|)!}{2^{|m|} |m|! (l-|m|)!}, \quad (2.15)$$

where $\Gamma(z)$ is the gamma function.

The probability of an ionization event during a timestep dt is given by

$$p = 1 - \exp(-W_{qs} dt). \quad (2.16)$$

The probability p is calculated for each atom/ion at each timestep. A Monte-Carlo technique is used to determine whether an electron will be ionized: A random number is created and compared with the ionization probability. Only if the random number is less than the ionization probability ionization occurs.

Above barrier ionization (ABI)

At very high field strengths the electric field amplitude reaches values sufficient to suppress the Coulomb barrier below the energy level of the ground state, opening the way to above-barrier ionization. Whenever the barrier is lower than the ionization potential an electron is ionized. In this case the new electron is placed at a distance of 1 Bohr from the parent ion.

Single photon ionization

Single photon ionization may occur if the energy of a laser photon $E_{Ph} = \hbar\omega$ exceeds slightly the ionization potential I_P of a neutral atom or an ion. The cross section of the single photon ionization of an atom near threshold can be estimated with high accuracy using the hydrogen-like approximation [41, page 68]

$$\sigma_{SPI} = 0.23 \left[1 - \frac{8}{3} \frac{E_{Ph} - I_P}{I_P} \right]. \quad (2.17)$$

Here and thereafter the atomic system of units is used. The single photon ionization rate is given by

$$W_{SPI} = \sigma_{SPI} \frac{cF^2}{8\pi\omega}, \quad (2.18)$$

where F is the electric field strength amplitude of the laser radiation, and c is the speed of light. Similar to tunnel ionization the probability is calculated with equation 2.16 and again a Monte-Carlo approach is used to determine whether single photon ionization occurs.

Electron-impact ionization

During the simulation free electrons may appear in the cluster by field or single photon ionization. These free electrons may create new electrons through electron-impact ionization (collisional ionization). The probability of the electron-impact ionization of a single atom or ion can be estimated by the formula of Lotz [42, 43]. Lotz's expression provides an empirical formula of the cross section σ_{EII} for electron-impact ionization

$$\sigma_{EII} = a q \frac{\ln(E_e/I_P)}{E_e I_P} \quad (E_e > I_P) \quad (2.19)$$

where $a = 4.5 \times 10^{-14} \text{cm}^2 \text{eV}^2$, q is the number of electrons in the outer shell of the ion, I_P is the ionization potential and E_e is the energy of the impact electron [44, 45]. The ionization takes place when the impact parameter

$$b < \sqrt{\frac{\sigma_{EII}}{\pi}}. \quad (2.20)$$

The impact parameter b and the formula of Lotz are related to an infinite initial electron-ion distance. However, when performing large-cluster simulations the parameters of the incident electron are only available at a finite distance. The connection between the local parameters and those at infinity for the incident electron is found by using an analytical expression reported by Last and Jortner

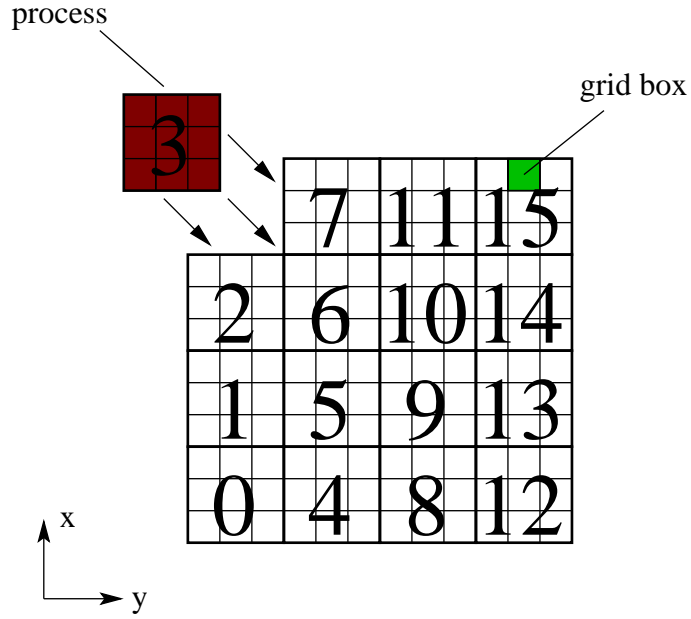


Figure 2.6: Parallelizing MPIC-Code by dividing the simulation volume into equally sized subvolumes

in [19]

$$E_e = E_l - \frac{q}{r_l} \quad (2.21)$$

$$b = \frac{1 + \xi}{\xi} \left[1 + \frac{\eta}{1 + \eta} \right] b_l \quad (2.22)$$

$$\xi = 0.159 r_l \frac{E_e}{q} \quad (2.23)$$

$$\eta = 0.4 \left(\frac{b_l}{r_l} \right)^2, \quad (2.24)$$

where b_l is the local (at finite distance) impact parameter, E_l is the local electron energy and r_l the distance between ion and incident electron. An electron impact is assumed to occur as soon as an electron approaches an ion closer than $r_l = 1.6 \times 10^{-8}$ cm. The particular choice of r_l is found to be of insignificant influence on the relative ionization probabilities of different atomic shells [46]. To determine if an electron is close to an atom or ion the MPIC code makes and continuously updates a map of all ion positions, similar to the linked list method in MD simulations [47, page 149].

2.1.3 Parallelization

Shrinking the grid box size to the order of the Bohr radius also has some drawbacks. For one, the integration timestep is approximately 10^{-19} s, which leads to a large number of timesteps for laser pulses in the range of 100 fs. Furthermore, the volume that can be simulated is restricted to a few hundred nanometer cube. To overcome these obstacles substantial computational resources are required. One way to decrease the time of program execution is to parallelize the program and use a multi-processor computer system for performing numerical experiments. The key to a successful algorithm is a good load balance and a minimum of data to be transferred. A common way of achieving load balance on parallel machines is through *domain decomposition* [48]. The physical domain of the problem is partitioned into smaller subdomains and the physical quantities of these subdomains are assigned to each processor.

To parallelize the MPIC-Code the simulation volume is divided into equally sized subvolumes as shown in figure 2.6. The simulation of each subvolume is performed by its own process. To perform the simulation a process has to have access to data calculated by other processes. In a PIC program a process transfers most of its data to neighboring processes it shares a surface with, e.g. process 6 in figure 2.6 sends and receives most of the data to and from processes 2, 5, 7 and 10. Much less data has to be transferred to diagonally neighboring processes (e.g. diagonal neighbors of process 6 are processes 1, 3, 9, and 11).

The MPIC program can either use open or periodic boundary conditions. When periodic boundary conditions are used the electric field values at the border of the simulation volume are fed back at the opposite side. Equally, particles which would leave the volume at one side are fed back to the process at the opposite side.

2.1.4 Implementation

The MPIC implementation used for the numerical experiments reported in this thesis is based on the regular PIC-Code program ILLUMINATION by Michael Geissler [49]. The program is written in Fortran 77 and Fortran 90 [50, 51]. The interprocess communication between the processes is performed via the Message Passing Interface (MPI) [52, 53]. A good introduction to MPI is given by Hoffman in [54, 55, 56].

2.1.5 Special hardware

The tendency in high performance computing moves towards clustering inexpensive off-the-shelf computer hardware [57]. Each computer works independently and communications software allows rapid data exchanges with other computers. The biggest bottleneck for any multiprocessor computer is the communications infrastructure, be it a shared bus or shared main memory. All inter-CPU communication must traverse this communications infrastructure, and a single CPU's processing will be delayed while it contends for access to this resource.

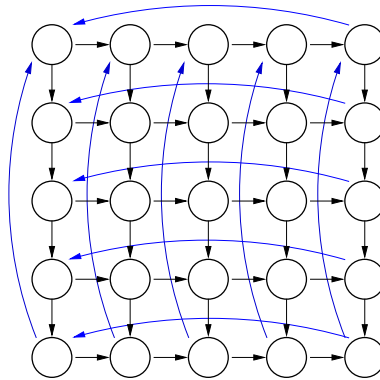


Figure 2.7: 2d point-to-point torus network. Circles represent computing nodes, arrows show point-to-point connections between two nodes. Parallelized PIC codes are an ideal application for this kind of computer networks, because PIC processes mainly communicate with their neighboring processes.

Parallelized PIC codes depend on a fast method of interprocess communication because of the large amount of data which is sent between the processes at each timestep (mainly the magnetic and electric field values at the process borders). Since processes in parallelized PIC codes mainly communicate with their neighboring processes it is an ideal candidate for computer systems using point-to-point networks like the scalable coherent interconnect (SCI) technology [58]. A collection of fast point-to-point unidirectional links [59] as shown in figure 2.7 overcomes the bottleneck of systems which use a bus for interprocess communication, because the resources for communication do not have to be shared between all nodes connected to the bus but only between two neighboring processors.

A new technology called InfiniBand Architecture (IBA) [60] promises an even greater bandwidth and almost unlimited expandability. InfiniBand is an architecture and specification for data flow between processors and I/O devices. InfiniBand overcomes the bandwidth and fanout limitations of the PCI bus by migrating from the traditional shared bus architecture into a switched fabric architecture. The point-to-point nature of an InfiniBand connection provides the full capacity of the connection to the two endpoints because the link is dedicated to the two endpoints. This eliminates the contention for the bus as well as the resulting delays that emerge under heavy loading conditions in the shared bus architecture.

2.2 Treecode

2.2.1 Principles

A large number of physical and chemical systems can be investigated by simulating the interaction between all particles constituting the system. In general, each particle in the systems interacts with all other particles. The interaction is often based on inverse square laws as Coulomb's law or Newton's law. Typically, these kinds of systems can be found in astrophysics, plasma physics, and molecular dynamics. Since the simulation involves following the trajectories of motion of a set of N particles, the problem is called the N-body problem. In the simplest algorithm the force on each particle is determined by direct summation of the contributions from all of the other $N - 1$ particles. In a discrete time integration, the forces at each timestep are then used to advance the particles along their trajectories according to a numerical integration scheme such as the leap-frog method. Computational costs of the direct summation scale as N^2 making this algorithm expensive. Treecodes are N-body programs which use a tree data structure to organize the particles into a hierarchy of clusters, starting from a cluster containing all the particles to clusters containing the individual particles. The first one who proposed a hierarchical method to efficiently solve many-body problems was Appel [61] in 1985. Treecode algorithms use the fact that the force of a group of distant particles can be well approximated by a low-order multipole expansion. Grouping the particles reduces the number of direct summations and results in a scaling proportional to $N \log(N)$ [12]. For more details about the scaling of treecodes see appendix A.

Figure 2.8 shows the flow chart for a treecode simulation. After initialization the timestep loop is entered. For each timestep the tree is first constructed inserting all N particles by a step-by-step division of the simulation volume. Then the electric field strength acting on each particle is calculated by walking through the tree. The last step is the calculation of the new velocity and position of each particle.

Tree construction

The tree construction starts by finding the smallest box that surrounds all particles. This box is called the root box or root cell. In figure 2.9 the root cell is the four-part rectangle on the top. The tree is built by inserting particle after particle to the growing tree. The search for a free spot in the tree starts at the root cell and is performed recursively from the top to the bottom. Inserting is done by finding a cell in the tree that is not occupied by another particle. If such a cell is found then the particle is stored as a leaf in the tree structure. If a leaf cell is already occupied by a particle then the cell is divided into 4 subareas (or 8 subvolumes in a 3d simulation). Hence, trees in 2d simulations are called *quad-tree* and in 3d simulations *oct-tree*. The new cells are stored as branches of the current leaf cell. This subdivision process is repeated recursively until both particles can be assigned to cells of their own. Figure 2.10 shows the fully

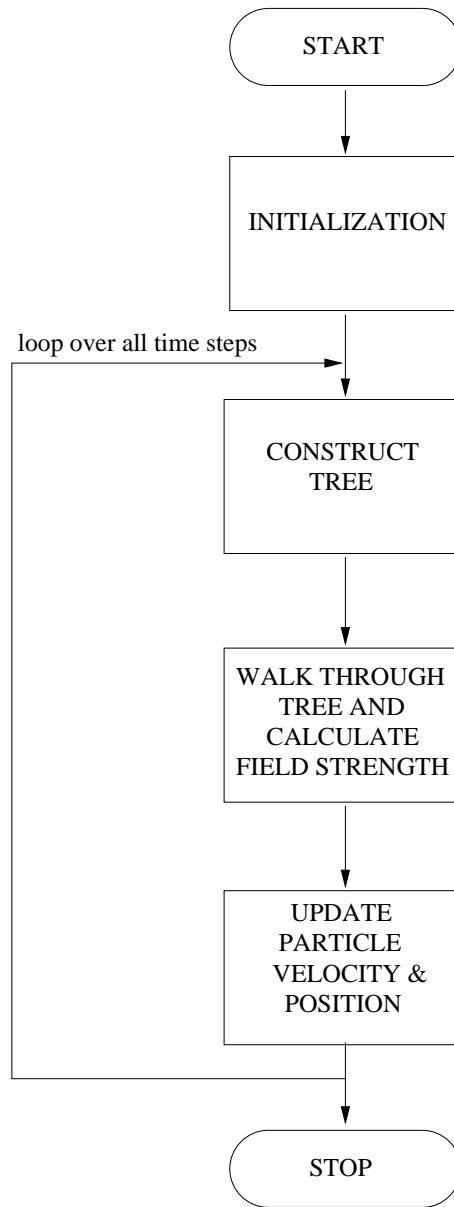


Figure 2.8: Flow chart of a treecode simulation.

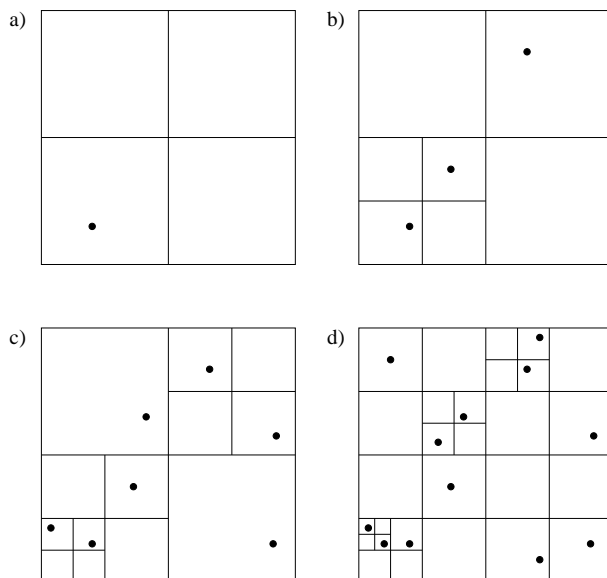


Figure 2.9: Example of tree construction for a 2d simulation.

constructed tree according to the particle ensemble depicted in figure 2.9. The constructed tree consists of two types of nodes. A node can either be a particle or a cell. A particle is always a leaf, whereas a cell is never a leaf.

After finishing the tree construction the total charge and the center of charge for all cells are calculated. This is also done recursively by starting at the root cell and walking from top to the bottom of the tree. The total charge of a cell is given by

$$q_c = \sum_{i=1}^N q_{c_i} + \sum_{j=1}^P q_j, \quad (2.25)$$

where i runs over all direct subcells and j over all particle nodes directly attached to the cell. Hence N and P are the number of direct subcells and particles, respectively. The center of charge is calculated by

$$\mathbf{r}_{\text{coc}} = \frac{\sum_{i=1}^N |q_{c_i}| \mathbf{r}_{\text{coc}_i} + \sum_{j=1}^P |q_j| \mathbf{r}_j}{\sum_{i=1}^N |q_{c_i}| + \sum_{j=1}^P |q_j|}. \quad (2.26)$$

If multipole expansion is used then higher order multipole moments are calculated at this stage, too.

In general, the tree construction and the calculation of multipole moments take approximately 3-10% percent of a typical timestep [62, page 76]. Therefore optimizing the tree construction is not very rewarding. Still, there exist faster ways of building the tree. Some of them are especially useful if a parallel treecode is implemented [62, chapter 4.3].

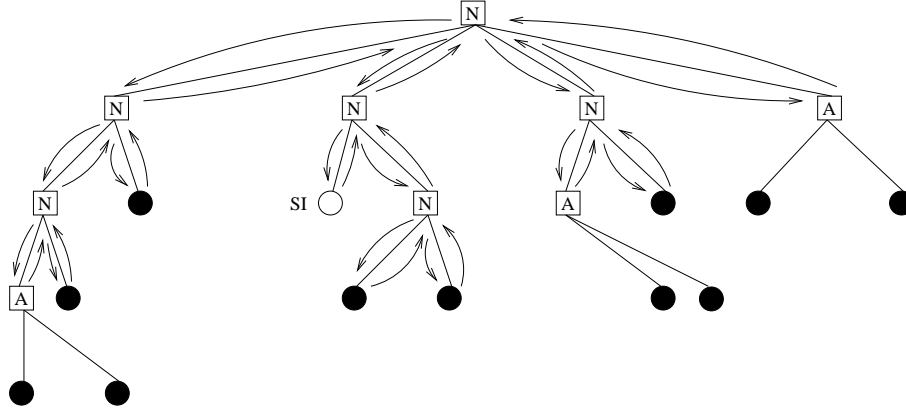


Figure 2.11: Example of a recursive tree walk to update electric field strength. The unfilled dot shows the particle the field strength is updated for. The filled dots denote the other particles. The rectangles represent the cells. A stands for *accepted*, N for *not accepted*. SI stands for *self interaction*. Self interaction is prevented by checking whether a particle would contribute to its own field strength.

algorithm. The case $\Theta \rightarrow \infty$ is called particle-pseudoparticle interaction and scales proportional to N .

More advanced multipole acceptance criteria (MAC) are reported in [12, 63]. These methods reduce the possibility of unbound errors in return of a higher computational effort.

Multipole expansion

One way of improving the accuracy of the treecode is to decrease the tolerance parameter Θ . Unfortunately, this measure deteriorates the performance of the treecode. A better way of increasing the accuracy is to use also the multipole moments of a cell rather than treating a cell as a point charge. According to figure 2.13 the electric field strength acting on particle P is

$$\mathbf{E}(\mathbf{R}) = \sum_i \mathbf{E}_i(\mathbf{R} - \mathbf{r}_i) = k_C \sum_i q_i \frac{\mathbf{R} - \mathbf{r}_i}{|\mathbf{R} - \mathbf{r}_i|^3}. \quad (2.29)$$

The Taylor expansion in vector notation [64, page 160] is defined by

$$\mathbf{F}(\mathbf{r} + \Delta\mathbf{r}) = \mathbf{F}(\mathbf{r}) + (\Delta\mathbf{r} \cdot \nabla)\mathbf{F}(\mathbf{r})\Big|_r + \frac{1}{2!}(\Delta\mathbf{r} \cdot \nabla)^2\mathbf{F}(\mathbf{r})\Big|_r + \dots \quad (2.30)$$

Applying equation 2.30 to the electric field strength in equation 2.29 considering a 3d implementation and only taking into account terms up to the quadrupole

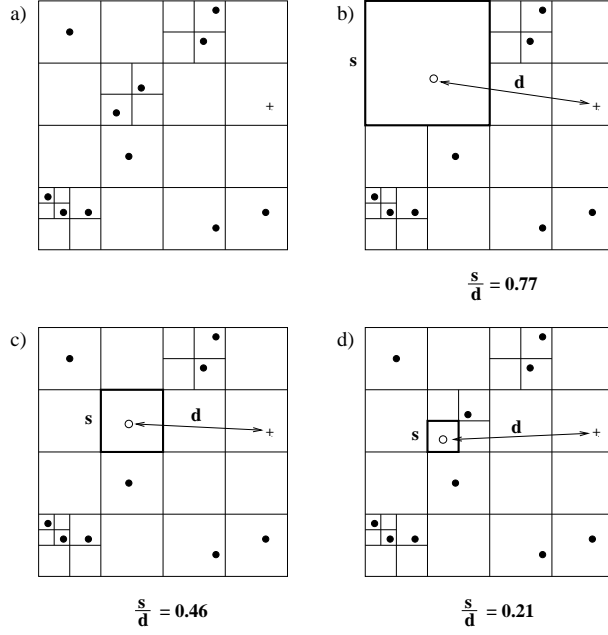


Figure 2.12: Distance to cell size ratio for different tree levels. The cross represents the particle the electric field strength is updated for. The filled dots indicate particles and the unfilled dots show the position of center of charge of the current cell.

moment results in

$$\begin{aligned}
E(\mathbf{R}) = & k_C \sum_i q_i \left[1 - x_i \frac{\partial}{\partial x} - y_i \frac{\partial}{\partial y} - z_i \frac{\partial}{\partial z} + \right. \\
& \frac{1}{2} x_i^2 \frac{\partial^2}{\partial x^2} + \frac{1}{2} y_i^2 \frac{\partial^2}{\partial y^2} + \frac{1}{2} z_i^2 \frac{\partial^2}{\partial z^2} + \\
& \frac{1}{2} x_i y_i \left(\frac{\partial}{\partial x} \frac{\partial}{\partial y} + \frac{\partial}{\partial y} \frac{\partial}{\partial x} \right) + \\
& \frac{1}{2} y_i z_i \left(\frac{\partial}{\partial y} \frac{\partial}{\partial z} + \frac{\partial}{\partial z} \frac{\partial}{\partial y} \right) + \\
& \left. \frac{1}{2} z_i x_i \left(\frac{\partial}{\partial z} \frac{\partial}{\partial x} + \frac{\partial}{\partial x} \frac{\partial}{\partial z} \right) \right] \frac{R}{R^3}. \tag{2.31}
\end{aligned}$$

R and \mathbf{r}_i are defined as follows

$$R = \sqrt{(x - x_i)^2 + (y - y_i)^2 + (z - z_i)^2} \quad (2.32)$$

$$\mathbf{r}_i = \begin{pmatrix} x_i \\ y_i \\ z_i \end{pmatrix} \quad (2.33)$$

Considering only the x-component of the electric field strength the derivatives of equation 2.31 give:

$$\frac{\partial}{\partial x} \frac{x}{R^3} = \frac{1}{R^3} - \frac{3x^2}{R^5} \quad (2.34)$$

$$\frac{\partial}{\partial y} \frac{x}{R^3} = -\frac{3xy}{R^5} \quad (2.35)$$

$$\frac{\partial}{\partial z} \frac{x}{R^3} = -\frac{3xz}{R^5} \quad (2.36)$$

$$\frac{\partial^2}{\partial x^2} \frac{x}{R^3} = \frac{15x^3}{R^7} - \frac{9x}{R^5} \quad (2.37)$$

$$\frac{\partial^2}{\partial y^2} \frac{x}{R^3} = \frac{15xy^2}{R^7} - \frac{3x}{R^5} \quad (2.38)$$

$$\frac{\partial^2}{\partial z^2} \frac{x}{R^3} = \frac{15xz^2}{R^7} - \frac{3x}{R^5} \quad (2.39)$$

$$\frac{\partial}{\partial y} \frac{\partial}{\partial x} \frac{x}{R^3} = \frac{15x^2y}{R^7} - \frac{3y}{R^5} \quad (2.40)$$

$$\frac{\partial}{\partial z} \frac{\partial}{\partial x} \frac{x}{R^3} = \frac{15x^2z}{R^7} - \frac{3z}{R^5} \quad (2.41)$$

$$\frac{\partial}{\partial z} \frac{\partial}{\partial y} \frac{x}{R^3} = \frac{15xyz}{R^7} \quad (2.42)$$

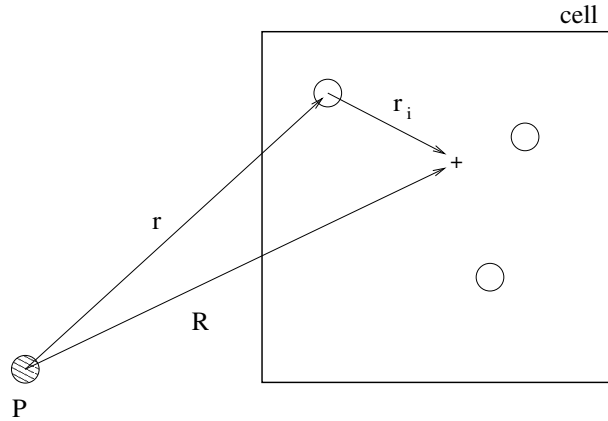


Figure 2.13: The cell contains three particles, which are represented by unfilled circles. The vector from particle P to the center of charge of the cell is \mathbf{R} . \mathbf{r}_i is the vector from a single particle to the center of charge and \mathbf{r} is the vector from the particle P to a single particle.

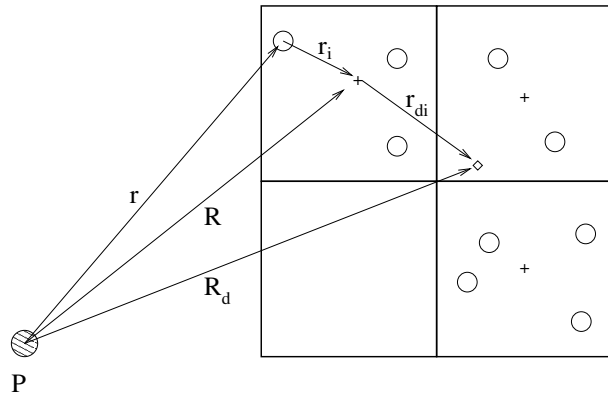


Figure 2.14: Displacement of multipole moments: The unfilled circles represent the particles the '+' denotes the center of charge of the subcells, the diamond symbol \diamond shows the center of charge of the parent cell. \mathbf{r}_i is the vector of a single particle to the center of charge of its parent cell. The vector from particle P to the center of charge of the daughter cell is \mathbf{R} . \mathbf{R}_d is the vector from particle P to the parent cell and \mathbf{r}_{di} is the vector from the center of charge of a daughter cell to the center of charge of its parent cell.

The above considerations result in an approximated electric field strength given by

$$\begin{aligned}
E_x &= k_C \left[\right. \\
\text{Monopole:} & \quad \frac{x}{R^3} \sum_i q_i \\
\text{Dipole:} & \quad - \left(\frac{1}{R^3} - \frac{3x^2}{R^5} \right) \sum_i q_i x_i + \frac{3xy}{R^5} \sum_i q_i y_i + \frac{3xz}{R^5} \sum_i q_i z_i + \\
\text{Quadrupole:} & \quad \frac{1}{2} \left(\frac{15x^3}{R^7} - \frac{9x}{R^5} \right) \sum_i q_i x_i^2 + \\
& \quad \frac{1}{2} \left(\frac{15xy^2}{R^7} - \frac{3x}{R^5} \right) \sum_i q_i y_i^2 + \\
& \quad \frac{1}{2} \left(\frac{15xz^2}{R^7} - \frac{3x}{R^5} \right) \sum_i q_i z_i^2 + \\
& \quad \left(\frac{15x^2y}{R^7} - \frac{3y}{R^5} \right) \sum_i q_i x_i y_i + \\
& \quad \left(\frac{15x^2z}{R^7} - \frac{3z}{R^5} \right) \sum_i q_i x_i z_i + \\
& \quad \left. \frac{15xyz}{R^7} \sum_i q_i y_i z_i \right] \tag{2.43}
\end{aligned}$$

The other components of the electric field strength can easily be obtained by cyclic rotation. The calculation of the sums ($\sum_i q_i x_i, \sum_i q_i y_i, \dots$) is simple for cells which only contain particles and no subcells. If a cell has daughter cells then the displacement of the centers of charge has to be taken into account as shown in figure 2.14. The x_i -contribution of the dipole moment for E_x for a daughter cell is calculated by

$$D_x^{daughter} = \sum_i q_i x_i. \tag{2.44}$$

For the parent cell the shift of the center of charge has to be considered. Therefore the contribution to the dipole moment has the form of

$$\begin{aligned}
D_x^{parent} &= \sum_d \left(\sum_i q_i (x_i + x_{di}) \right) \\
&= \sum_d \left(\sum_i q_i x_i + x_{di} \sum_i q_i \right) \\
&= \sum_d (D_x^d + x_d q_c^d) \tag{2.45}
\end{aligned}$$

Equation 2.45 shows that the dipole moment of a parent cell can be determined by using the dipole moments of the daughter cells, the total charge of the daughters, and the displacement vector r_d . The shift of origin of the quadrupole moments can be obtained by the same way. The x_i - x_i - and x_i - y_i contributions to the quadrupole moment of the electric field strength in x-direction for daughter cells are

$$\begin{aligned} Q_{xx}^{daughter} &= \sum_i q_i x_i x_i, \\ Q_{xy}^{daughter} &= \sum_i q_i x_i y_i. \end{aligned} \quad (2.46)$$

Equation 2.46 transforms to

$$\begin{aligned} Q_{xx}^{parent} &= \sum_d \left(\sum_i q_i (x_i + x_d)^2 \right) \\ &= \sum_d \left(\sum_i q_i x_i^2 + 2x_d \sum_i q_i x_i + x_d^2 \sum_i q_i \right) \\ &= \sum_d (Q_{xx}^d + 2x_d D_x^d + x_d^2 Q_c^d) \end{aligned} \quad (2.47)$$

$$\begin{aligned} Q_{xy}^{parent} &= \sum_d \left(\sum_i q_i (x_i + x_d)(y_i + y_d) \right) \\ &= \sum_d \left(\sum_i q_i x_i y_i + x_d \sum_i q_i y_i + y_d \sum_i q_i x_i + x_d y_d \sum_i q_i \right) \\ &= \sum_d (Q_{xy}^d + y_d D_x^d + x_d D_y^d + x_d y_d Q_c^d) \end{aligned} \quad (2.48)$$

for the parent cells. Similarly, to the dipole moment the quadrupole moment for a parent cell can be calculated by its daughter's multipole moments and the displacement vector. Hence, these moments are usually calculated recursively by starting at the top.

In treecodes typically the highest term of multipole expansion is the quadrupole term, because a further increase in the multipole order is computationally more expensive than an equivalent decrease of Θ [62].

Update of velocity and position

Position and velocity updates of particles are performed by the so-called leap-frog method [65]. The particle velocity is calculated with an offset of $\Delta t/2$ to

the particle position:

$$\mathbf{v}_i(t + \frac{\Delta t}{2}) = \mathbf{v}_i(t - \frac{\Delta t}{2}) + \mathbf{a}_i(t)\Delta t, \quad (2.49)$$

$$\mathbf{r}_i(t + \Delta t) = \mathbf{r}_i(t - \Delta t) + \mathbf{v}_i(t + \frac{\Delta t}{2})\Delta t, \quad (2.50)$$

$$\mathbf{v}_i(t) = \frac{\mathbf{v}_i(t + \frac{\Delta t}{2}) + \mathbf{v}_i(t - \frac{\Delta t}{2})}{2}. \quad (2.51)$$

Here i denotes the particle. The acceleration of particle i is given by

$$\mathbf{a}_i(t) = \frac{\mathbf{E}_i(t) * q_i(t)}{m_i}, \quad (2.52)$$

where m_i and q_i are the mass and the charge of particle i , respectively. \mathbf{E}_i is the electric field strength action on particle i , which was calculated by traversing through the tree.

The leap-frog scheme is second order accurate in time for a constant integration timestep Δt . It is the preferred scheme and widely adapted in treecode simulations [62].

Non-recursive tree walk

One way of speeding up treecodes without changing the accuracy was proposed at the same time in [66, 67, 68]. Recursive tree walks produce a considerable overhead because the tree walk is invoked many times for each timestep. One way to reduce the number of invocations is to eliminate the recursion which can be achieved by using an optimized order of nodes during the tree traversal. A non-recursive walk can be performed by arranging the tree in a linked list. Figure 2.15 shows a fully balanced binary tree and its linked list. Each node in the tree has a link to its first child, which is labeled with M in figure 2.15 and each child contains a pointer to its next sibling, which is denoted by N . The last child of a level points to its parent's sibling. Particles only have a *Next*-pointer, because they are always leaf nodes.

The numbers show the index of the node in the linked list. The electric field strength calculation is done by walking through this list. If a cell has to be opened it uses the *More*-pointer to walk down the tree. If the cell is accepted then the *Next*-pointer is used to jump to the next sibling. Barnes [66] accomplishes the non-recursive tree walk by managing two lists of pointers. One array - called *interaction* list - contains pointers to all nodes (cells and particles) which interact with the particle to be updated. The other list - called *active* list - contains pointers to all nodes which will be examined when constructing interaction lists. All particles in the *active* list are put into the *interaction* list unless it is the particle to be updated itself. Cells are only appended to the *interaction* list if they obey the acceptance criterion. If some active cells have been rejected the examining continues at the next level of the tree, taking the descendents of the rejected cells as *active*.

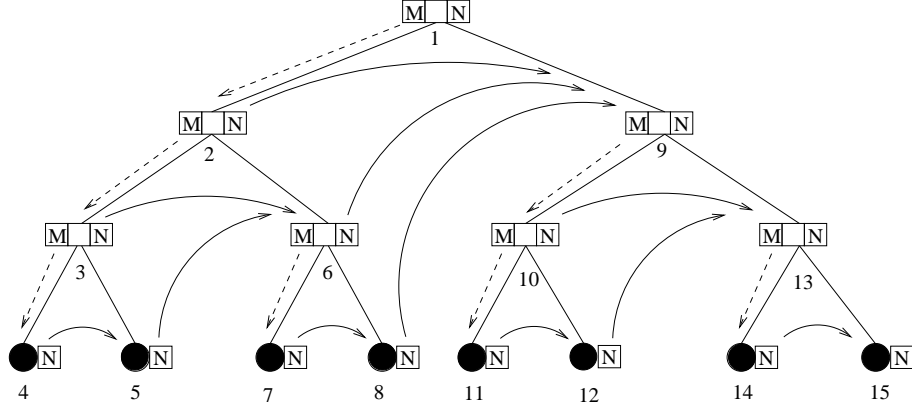


Figure 2.15: Idealized balanced binary tree showing the order of nodes for a non-recursive tree walk. The rectangles represent cells and particles are denoted as filled circles. N and M are pointers to other nodes and stand for *Next* and *More*, respectively.

Figure 2.16 illustrates the performance gain of a non-recursive treewalk compared to a recursive approach. The recursive tree traversal requires 20 steps whereas the non-recursive tree walk only needs 10.

Energy conserving particle creation

During the simulation, ionization events occur which result in the creation of new electrons and incrementing the charge state of the mother atom or ion. To prevent artificial heating the total energy of the particle ensemble before and after the creation process has to be equal

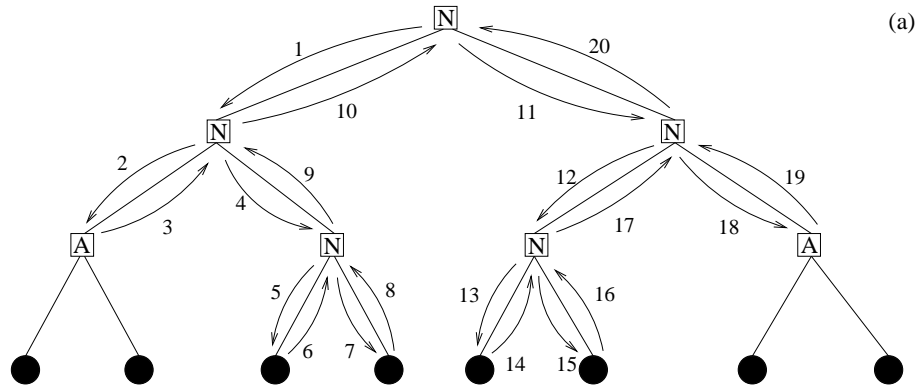
$$E_{kin}^b + E_{pot}^b = E_{kin}^a + E_{pot}^a, \quad (2.53)$$

where E_{kin}^b and E_{pot}^b are the total kinetic and total potential energies of the system before the ionization of an electron, and E_{kin}^a and E_{pot}^a are the energies afterwards. Assuming a given electron position this can be achieved by setting the new electron velocity to a proper value. Presuming that the creation is done infinitely fast the velocity of the already existing particles remains constant and

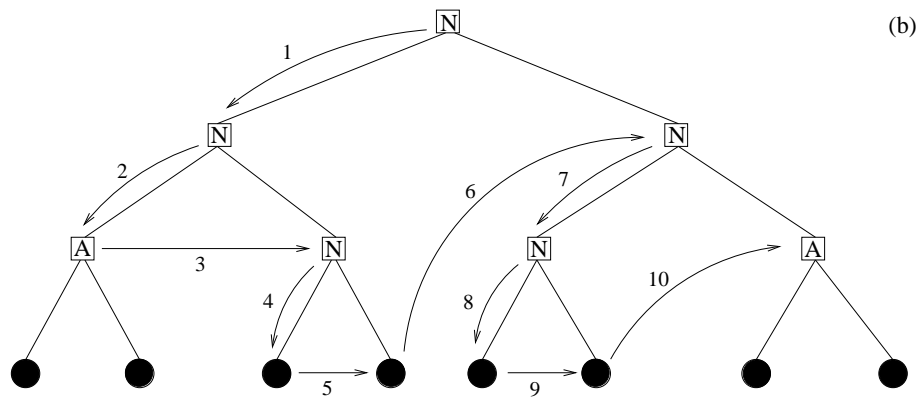
$$E_{kin}^a = E_{kin}^b + E_{kin}^{el}, \quad (2.54)$$

where E_{kin}^{el} is the kinetic energy of the electron to be created. The potential energy after the ionization is given by

$$E_{pot}^a = E_{pot}^b + \sum_{j=1, j \neq ion}^N \frac{q_j(q_{ion}^a - q_{ion}^b)}{|\mathbf{r}_j - \mathbf{r}_{ion}|} + \sum_{j=1, j \neq ion}^N \frac{q_j q_{el}}{|\mathbf{r}_j - \mathbf{r}_{el}|} + \frac{q_{el} q_{ion}^a}{|\mathbf{r}_{el} - \mathbf{r}_{ion}|}, \quad (2.55)$$



(a)



(b)

Figure 2.16: Comparison of a recursive and a non-recursive tree walk. (a) shows an example of a recursive tree walk with 20 steps. For a non-recursive tree traversal (b) only 10 steps are needed.

where q and \mathbf{r} are the charge and the position of the particle, respectively and N is the number of particles in the system. Using equation 2.53, 2.54, and 2.55 we obtain the kinetic energy for the new electron as follows

$$E_{kin}^{el} = - \sum_{j=1, j \neq ion}^N \frac{q_j(q_{ion}^a - q_{ion}^b)}{|\mathbf{r}_j - \mathbf{r}_{ion}|} - \sum_{j=1, j \neq ion}^N \frac{q_j q_{el}}{|\mathbf{r}_j - \mathbf{r}_{el}|} - \frac{q_{el} q_{ion}^a}{|\mathbf{r}_{el} - \mathbf{r}_{ion}|}. \quad (2.56)$$

2.2.2 Implementation

The treecode implementation used throughout this thesis is based on a treecode written by Joshua Barnes. It can be downloaded from [69]. The original version by Barnes uses a hierarchical force calculation algorithm and is designed for astrophysical applications, which means the acting forces are the result of gravitational interactions and are proportional to the mass of particles. To be able to perform laser-cluster simulations three major changes have been performed (a) the forces between the particles are of electrostatic and not of gravitational origin therefore the force calculation routine was modified, (b) implementation of ionization was added, and (c) the program was parallelized.

2.2.3 Parallelization

For the parallelization the following approach was chosen: each processor holds a copy of the entire particle array and tree structure. A certain processor is only responsible for updating a subset of the particles. After the calculation of the new electric field strength values acting on the particles these values are transmitted via MPI to all other processors. Knowing the field strength values of all particles each processor advances the trajectories of all particles and also calculates ionization and recombination events of each atom and ion. When the new positions and velocities are known all processors build the new tree. This means that parallelization is only implemented in updating the electric field strength values. The rest of the program is executed sequentially. This approach is justified since the number of particles is small and therefore sending and receiving the new field strength values takes less the 8 % of the computation time. Furthermore, building the tree and calculating the ionization and recombination events only takes a fraction of time consumed by computing the field strength. Nevertheless, according to Amdahl's law [70], the maximum performance gain G one can expect from the parallelization is given by

$$G = \frac{t_s + t_p}{t_s + \frac{t_p}{N}}, \quad (2.57)$$

where N is the number of processors, s is the amount of time spent (by a serial processor) on serial parts of a program and p is the amount of time spent (by a serial processor) on parts of the program that can be done in parallel.

To further decrease the execution time a second level of parallelization was introduced. Each MPI process spawned two threads for traversing the tree

and updating the electric field strength. This approach was chosen to ideally adapt the code to the computer equipment used. Since the used Linux cluster consists of 32 dual processor servers the amount of data transferred over the GBit Ethernet network was minimized by just having 32 processes transferring data over the network. The data shared between the threads does not require interprocess communication because all threads belong to the same process and hence share the same memory.

2.2.4 Future improvements

Different timesteps for electrons and ions could be used because electrons move much faster than ions. The use of adaptive timesteps Δt which take into account the particle velocity would be even better.

A better approach for parallelizing was suggested by Barnes and requires to order particles as they would be encountered in a tree-walk, estimate the computational work required to calculate the force on each, and give each processor the job of computing forces for a contiguous block of bodies.

2.3 Comparison of treecodes with MPIC Codes

2.3.1 Advantages of MPIC codes

The main advantage of MPIC codes over treecodes is the better numerical scaling. In the case of laser cluster interaction simulations ($N \ll M$) MPIC codes scale as $\sim \mathcal{O}(M)$, where M is the number of grid cells and N is the number of particles. Commonly the simulation volume V_{sim} increases linearly with the cluster volume $V_{cluster}$. As V_{sim} is proportional to M^3 and $V_{cluster}$ is proportional to N^3 MPIC codes scale approximately as $\sim \mathcal{O}(N)$. Whereas treecodes scale as $\sim \mathcal{O}(N \log(N))$.

Furthermore in MPIC codes the propagation of the laser pulse is performed inherently by calculating the electromagnetic field. This means that not only the effect of the laser field on the simulated matter is performed but also the effect of the matter on the propagation of the laser pulse.

In the relativistic regime, which starts at intensities higher than 10^{17} W/cm² (at 800nm), the particle velocities are high enough that the $(\mathbf{v} \times \mathbf{B})$ -term in equation 2.12 leads to a particle motion in direction of the wave vector [71]. Since treecodes do not include magnetic fields, they are limited to non-relativistic simulations where the magnetic field does not play a role.

2.3.2 Advantages of treecodes

In MPIC codes the electric and magnetic fields are only defined at fixed positions. In between the discrete grid the field values are averaged. The discrete nature of the field values is the reason that MPIC codes automatically include a form of shielding that is directly related to the grid box size as shown in figure

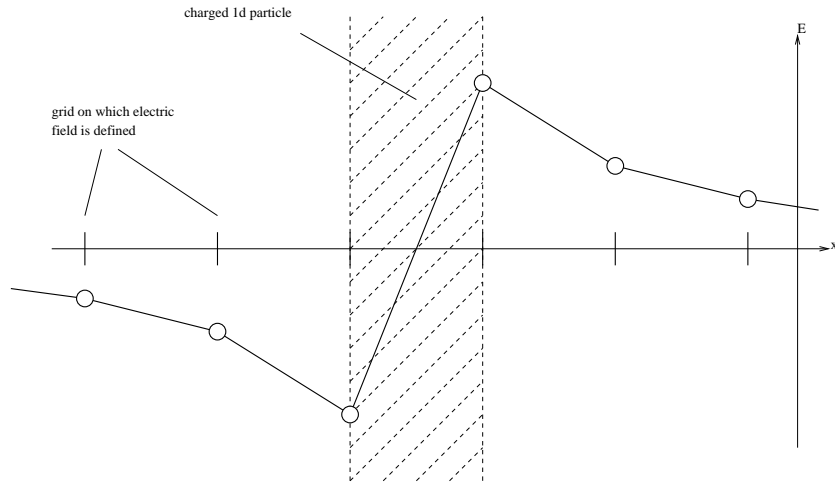


Figure 2.17: Illustration of the electric field strength of a charged 1d particle in an MPIC simulation. The electric field is only defined on grid points. In between the electric field is averaged. The discrete nature of the grid inherently adds a shielding to the MPIC algorithm. The shielding depends on the size of the grid cells. The larger the cells the stronger the shielding.

2.17. Type and size of the shielding are critical parameters in particle codes and are preferably tunable independently from the grid box size.

Another problem of MPIC codes is the asymmetric Coulomb potential of charged particles as shown in figure 2.18. Depending on the relative position of the particle in a grid cell the spatial asymmetry varies. This can cause artificial heating (and cooling) when an electron passes by an ion. The potential the electron experiences when approaching might be higher than it is when the electron is departing (see figure 2.18 (b)).

In MPIC codes the timestep size cannot be chosen independently from the grid box size. Since the propagation of light is automatically included by solving the Maxwell's equations one timestep Δt has to be less than h/c_0 , where h is the length of a gridbox and c_0 is the velocity of light. Whereas in treecodes the timestep size can be chosen freely as long as it is not reason for numerical heating and instabilities.

Another drawback of MPIC codes is the fixed simulation volume. The simulation volume of MPIC codes cannot grow during simulation - at least not without a lot of extra work. This means that at some point particles leave the simulation volume and are not subject to the computation anymore. Post-processing of particles which have left the volume can be time consuming and complex. Treecodes do not have this limitation because the simulation volume is adapted for each timestep when the tree is constructed. A growing simulation volume is extremely useful when electrons leave the cluster or the cluster

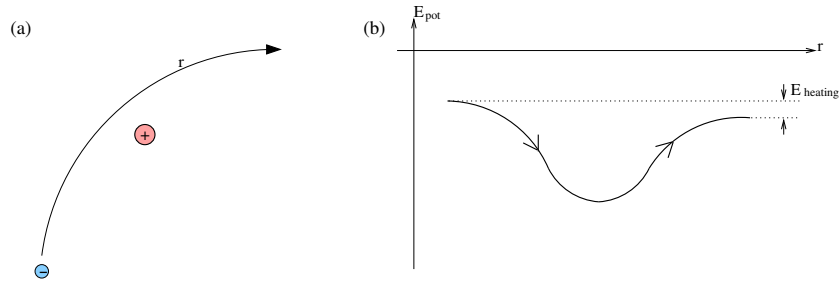


Figure 2.18: (a) Schematic illustration of an electron trajectory r . (b) depicts the potential energy of the ion acting on the electron moving along trajectory r . Because of the spatial asymmetry of the potential the electron gains energy E_{heating} .

explodes.

2.3.3 Drawbacks shared by both methods

Both approaches have limited freedom where a new particle can be created. In MPIC codes new electrons have to be put exactly at the same position as the parent ion. Otherwise the equation of charge continuity is disobeyed and the MPIC code produces wrong results. On the other hand in treecode simulations a new electron must not be set at the position of the parent ion because this would result in an infinite long branch in the tree and would cause failure of the treecode algorithm.

A major limitation of both methods and also of all other particle codes is the small timestep that has to be used to avoid numerical heating. The particle velocities depend on the kind of simulation which is performed. But even in the non-relativistic regime electron velocities are high enough that timesteps in the sub-attosecond range are required to minimize numerical heating. In the simulations done throughout this thesis timesteps typically have been set to $\sim 10^{-20}$ seconds. Assuming a laser pulse with \sin^2 -envelope and a full width half maximum of 100fs results in $\sim 10^7$ steps for one simulation.

2.4 Computer equipment

Most of the numerical experiments were performed on two systems. First, on a SUN Fire computer cluster [72] which was composed of several symmetric multiprocessor (SMP) systems based on 1.05 GHz UltraSPARC III processors and Solaris 9 Operating Environment. Second, on a Linux cluster with 64 Intel Xeon processors with a clock rate of 2.4 GHz. The 32 dual Xeon processor servers were interconnected via a Gigabit Ethernet. The operating system was Redhat 8.0 and the Intel Fortran and Intel C Compiler were used for compiling

the programs. On the Linux cluster 3 different implementations of MPI were tested, namely, MPICH [73], LAM MPI [74] and MP_Lite [75, 76]. The best results were obtained using the lightweight message passing library MP_Lite. On the SUN cluster the native Fortran and C compiler and MPI environment were used.

2.5 Cross sections and ionization potentials

One main issue of computational physics is to have access to reliable physical constants as cross sections for impact ionization and ionization potentials for neutral atoms and ions. The following sources turned out to be useful: Ionization potentials for many atoms and ions can be found at the website of the National Institute for Standards and Technology [77]. Calculated values of ionization potentials of multiply charged ions are reported in [78, 79]. Values of ionization potentials of highly charged many-electron elements are listed in [80].

Cross section of ionization by electron impact for atoms and ions of many elements can be found in [81].

Chapter 3

Asymmetric explosion of large rare gas clusters

In this chapter a three dimensional microscopic particle in cell (MPIC) code is presented. The code simulates nanoplazmas in intense laser fields, taking account of all relevant microscopic interactions. The simulation reveals the physical processes determining the laser induced explosion of large clusters with several 10000 atoms.

3.1 Introduction

Atomic clusters exposed to intense laser pulses explode and create a hot, dense plasma [21]. This process is of interest for the generation of x-rays [16], for electron and ion acceleration [82], and for the creation of nuclear particles [17]. For the design of such experiments, a thorough understanding of the cluster explosion dynamics is essential.

In small clusters, containing only a few 100 atoms, laser heated electrons can escape easily. The positive space charge of the remaining ions leads to a Coulomb explosion. Small clusters are accessible to molecular dynamics (MD) simulations [46, 83, 84, 45]. As a result, their explosion dynamics is relatively well understood. In clusters with more than 1000 atoms the situation becomes more complicated. MD simulations are limited to about $N = 1000$ atoms [19], because the workload increases with N^2 . Therefore, analysis of the explosion of large clusters relies on phenomenological models [85, 86]. Currently, there are no numerical methods that can properly take into account both, microscopic and hydrodynamic macroscopic phenomena. As a result, the physical mechanisms determining the explosion of large clusters could not be identified unambiguously so far.

The MPIC code contains no free parameters and presents a virtual experiment. To test its reliability recent experiments reporting an asymmetric explosion of Ar and Xe clusters [87, 88] with $N \geq 10000$ have been calculated. The

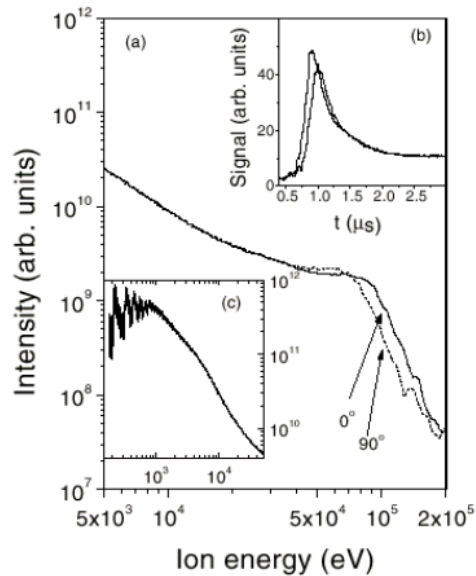


Figure 3.1: Measured ion energy spectrum for a Ar_{40000} cluster after Kumarap-pan et al. [87].

computed spectra and angular distributions of electrons and ions are found to be in good agreement with the experiments.

3.2 Results

The MPIC simulations reveal the first complete picture of the explosion of large clusters. The essential new findings are: (i) The explosion is driven by a combination of electrostatic (Coulomb explosion) forces [89] and hydrodynamic processes [85, 86]. The analysis does not confirm resonant laser plasma coupling predicted by hydrodynamic models [85, 86]. (ii) CEI plays a major role in the Coulomb explosion of molecules [90, 91] and small clusters [84]. CEI and a related mechanism dubbed polarization enhanced ionization (PEI) dominate the ionization process in large clusters, too. PEI also explains the asymmetric explosion observed in recent experiments [87, 88]. (iii) The main electron heating mechanism is laser dephasing heating (LDH). The macroscopic, electric field of the cluster causes dephasing between the laser driven motion of the electrons and the laser field which allows electrons to absorb energy from the laser.

The MPIC code calculates the classical dynamics of all charged particles. Quantum mechanical phenomena, such as ionization, have to be added. The ionization of atoms and ions [84] is calculated by using the ADK (Ammosov-Delone-Krainov) tunneling rate [37]. The MPIC code solves the Maxwell's equa-

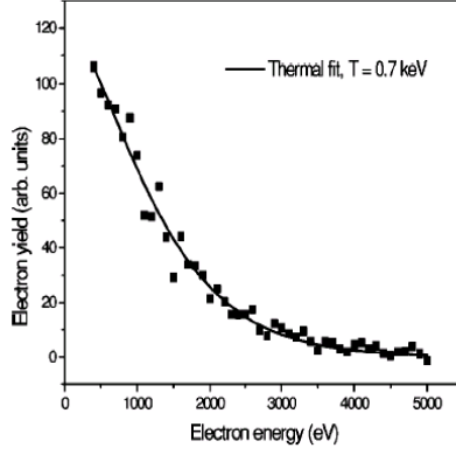


Figure 3.2: Measured electron energy spectrum for a Xe_{25000} cluster after Kumarappan et al. [88]

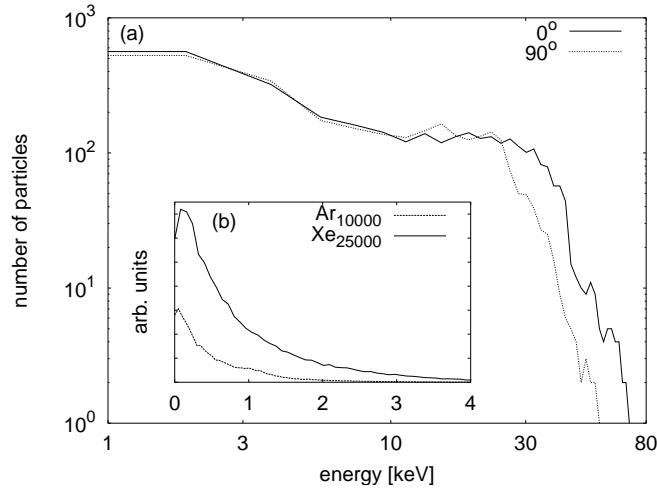


Figure 3.3: (a) Energy spectra of ions emitted by an Ar_{10000} cluster after irradiation with an 100 fs FWHM (full width at half maximum) laser pulse, \sin^2 pulse envelope, peak intensity $I = 8 \times 10^{15} \text{ W/cm}^2$, wavelength $\lambda = 800\text{nm}$. The laser field propagates in z -direction and is linearly polarized in x -direction. The solid and dotted lines refer to ion emissions parallel and perpendicular to the laser electric field. (b) Electron energy spectrum for Ar_{10000} and Xe_{25000} . The exponentially decaying part of the spectrum can be described by a single temperature that is 580 eV and 800 eV for the Ar and Xe cluster, respectively.

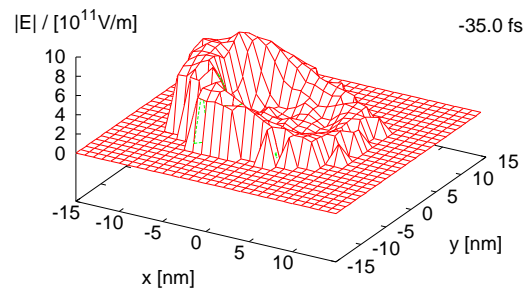
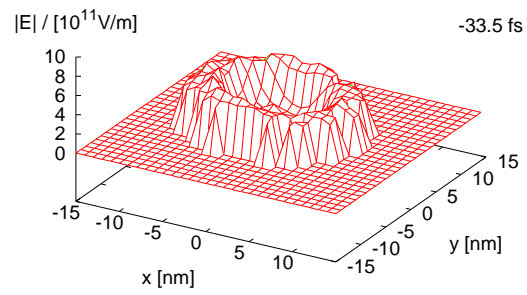
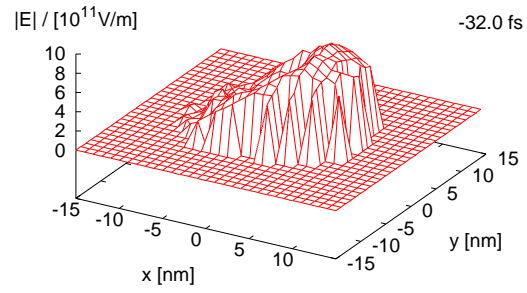


Figure 3.4: Electric field strength acting on the ions of an Ar_{10000} cluster for $t = -32.0$, $t = -33.5$ fs, and $t = -35.0$ fs. Pulse parameters are the same as described in caption of figure 3.3.

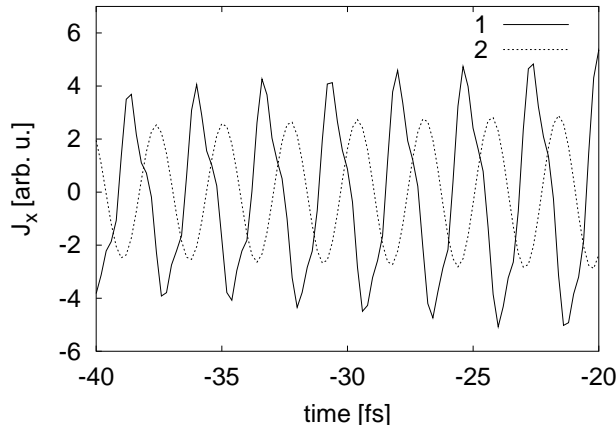


Figure 3.5: This figure shows the macroscopic electron current J_x (1), as defined in the text and the current of a single free electron (2) in direction of the laser electric field. The currents were scaled to similar size to facilitate comparison. The phase difference between free electron current and cluster current and the non-sinusoidal (nonlinear) contributions (corresponding to higher harmonics of the laser field) lead to polarization dephasing heating (PDH) of the electrons.

tions and calculates the complete electromagnetic field of the laser and of all charged particles in the whole simulation volume at each timestep. The value of this field at the position of the individual atoms/ions, E , is inserted into the ADK theory, from which the actual ionization events are calculated with a Monte-Carlo technique. The ionized electron is born by putting the center of gravity of the corresponding box a distance I_p/E away from the ion, along the direction of the electric field vector. At this point the tunneling electron wavepacket penetrates the barrier. Here, I_p is the ionization potential. The electron velocity at the time of birth is assumed to be zero. Further, impact ionization is taken into account by the Lotz formula [42, 45]. The MPIC code makes and continuously updates a map of all ion positions, similar to the linked list method in MD simulations [47]. The map is used to determine the nearest ions surrounding each electron. Impact ionization occurs, whenever a free electron moves into the area around an ion determined by the Lotz cross section. Tunnel ionization is disabled as long as the electron is within this area. Finally, all other microscopic effects can, to a good approximation, be treated classically and are taken into account by the MPIC formalism.

The analysis presented in this chapter is performed for the parameters of recently published experiments [87, 88]. The neutral cluster is modelled by atoms at rest that are arranged in an fcc-lattice. However, the choice of the initial condition is uncritical, as the explosion of large clusters is dominated by the macroscopic dynamics of the nanoplasma. The experiments are performed

in the limit of low cluster density, where the interaction between neighboring clusters is negligible. The length of the simulation box is chosen five times the cluster diameter with open boundary conditions. The particles leaving the simulation volume before the end of the laser pulse have to be post-processed in order to determine the ion and electron spectra. This is done by using a mean field PIC approach outside the simulation volume. The laser pulse propagates in z-direction and is linearly polarized in x-direction. The pulse duration is 100fs and the peak intensity $8 \times 10^{15} \text{W/cm}^2$. An Ar cluster with 10000 atoms and a Xe cluster with 25000 particles have been calculated. The cluster diameters are 9nm and 14nm and the inter-atomic distances are 0.375nm and 0.434nm, respectively. The size of the box representing one particle (atom, ion, electron) is 0.1 nm. The calculations were performed on 16 SUN Ultra Sparc III processors and took 20 days for the Ar₁₀₀₀₀ cluster.

The ion spectrum in figure 3.3(a) was calculated for an Ar₁₀₀₀₀ cluster. In the low energy range the ion spectra in and perpendicular to the laser polarization coincide. In the cut-off region, for energies greater than 2×10^4 eV, the spectra differ. Ions emitted along the laser electric field are shifted to higher energies in agreement with the experiments reported in [87]. The 16 processors were not sufficient to calculate an Ar₄₀₀₀₀ cluster to make a quantitative comparison with Ref. [87]. However, the electron spectrum of the Xe₂₅₀₀₀ cluster experiment in [88] could be calculated by choosing a larger box size of 0.15nm. The exponentially decaying part of the spectrum in figure 3.3(b) can be described by a single temperature that is 800 eV. This is slightly higher than the 700 eV measured in Ref. [88]. The good agreement demonstrates the predictive power of the MPIC code.

The essential elements of the cluster explosion dynamics can be understood from figure 3.6. The calculation shows that ionization is dominated by field ionization and collisional ionization is negligibly small during the whole cluster explosion in agreement with conclusions obtained from small cluster simulations [45]. Figure 3.6(a1) shows a snapshot of the ion charge states at the leading edge of the laser pulse, where the laser intensity is $4.4 \times 10^{14} \text{W/cm}^2$. Singly and doubly charged ions are created in the cluster core. This is at first sight surprising as the laser intensity is too small for the creation of doubly charged ions. The mechanism becomes clear by inspecting the electric field in the cluster, depicted in figure 3.6(a3). Electrons are heated and leave the cluster. The heating mechanism is discussed below. The net positive charge of the excess ions gives rise to the buildup of an electric field. Electron density fluctuations locally increase the field strength to values comparable to laser intensities of 10^{15}W/cm^2 . The electric field causes CEI, similar to CEI in molecules [90, 91], however, with an additional stochastic component. Similar mechanisms might also play a role in the ionization and damage of dielectric materials.

Figure 3.4 illustrates the change of the electric field strength acting on the ions of an Ar₁₀₀₀₀ cluster during one laser cycle ($t = -32.0$, $t = -33.5 \text{fs}$, and $t = -35.0 \text{fs}$). At the maximum of the laser electric field ($t = -32.0$ and $t = -35.0 \text{fs}$) the electrons are pushed to one side of the cluster leaving the other side depleted. This depletion causes an electric field much higher than

the laser electric field. As the electric field strength at the maxima looks like the caldera of the Greek island Santorini this effect was termed Santorini effect. The electrons are located at the center of the cluster if the driving laser electric field is small (at $t = -33.5fs$). The shielding effect of the electrons causes a low electric field in the center of the cluster. A ring of high electric field values at $t = -33.5fs$ can be observed because some of the electrons have already left the cluster. The electrons still inside are pushed to the center by the positive charges of the ions leaving the outer sphere depleted.

Figures 3.6(a1)-(a3) reveal another ionization mechanism related to CEI. The red spots in figure 3.6(a1) indicate enhanced ionization at the cluster poles. The enhanced ionization originates in the laser induced polarization of the electron cloud. The laser field is strong enough to push the electron cloud over the cluster boundary as depicted in figure 3.6(a2). As a result, an electric field is generated at the opposite pole of the cluster by electron depletion as shown in figure 3.6(a3). The polarization induced electric field at the poles exceeds the laser electric field by up to an order of magnitude, and causes PEI. PEI is responsible for the creation of the highest charge states and creates the high energy end of the ion spectrum. The different ionization states at the poles and at the equator are responsible for the asymmetric ion spectrum in figure 3.3.

With increasing time more electrons are heated and escape the cluster. In contrast to figure 3.6(a2), where the electrons are still evenly distributed over the cluster core, the remaining bound electrons are no longer sufficient to shield the whole cluster. As a result, only the center of the cluster is shielded and the electron density drops to zero towards the cluster surface. The reduced electron shielding towards the cluster surface creates an ion electric field which is represented by the green ring in figure 3.6(b3). The ion electric field dominates the laser field, however, is weaker than the field at the cluster poles. It causes CEI, creating the green colored shell of higher charged ions around the cluster center in figure 3.6(b1). The resulting positive space charge ejects ions symmetrically from the cluster and creates the intermediate energy ions in figure 3.3.

The cluster core keeps its shape and size over a significant fraction of the laser pulse as shown in figures 3.6(b1) and (b2). The reason is that due to electron shielding the positive space charge in the cluster is kept small. After the peak of the laser pulse no new electrons are created by ionization. The continuous ejection of hot electrons starts to deplete the cluster center. As a result, the ion core starts to expand, further facilitating the escape of the remaining electrons. The cluster is completely depleted of electrons 50fs after the laser pulse peak. In the absence of electrons CEI takes place again, creating charge states up to $3+$ in the cluster center. The cluster center undergoes symmetric Coulomb explosion and forms the low energy part of the ion spectrum in figure 3.3.

There has been an ongoing discussion whether hydrodynamic pressure or electrostatic forces drive the explosion of large clusters [85, 86, 89]. Which of the two mechanisms prevails depends on the rate at which electrons are heated and can leave the cluster. The MPIC simulations reveal that all electrons are removed from the cluster. However, in contrast to small clusters where all electrons are emitted at early stages, electrons in large clusters are removed grad-

ually. Depletion starts at the cluster boundary and then gradually progresses towards the center. As a result, the explosion dynamics is determined by an interplay between electrostatic forces (Coulomb explosion and CEI) and plasma processes which shield parts of the cluster. The analysis does not confirm the resonant electric field enhancement predicted by hydrodynamic models [85, 86].

3.3 Heating mechanism

A surprising element of the simulations is that all electrons are heated sufficiently to leave the cluster core. Inverse Bremsstrahlung can be ruled out as the dominant electron heating mechanism. The electrons follow the laser electric field and do not exhibit an isotropic angular distribution, as would be the case for inverse Bremsstrahlung heating. LDH has been identified as the dominant mechanism. Electron energy absorption is determined by the integral

$$L = \int \mathbf{J}\mathbf{E}dt = \int J_x E_x dt. \quad (3.1)$$

The electron current in the direction of the laser electric field is determined by the sum over all electrons,

$$J_x = dP_x/dt = e \sum_i dx_i/dt \delta(\mathbf{r} - \mathbf{r}_i), \quad (3.2)$$

where e is the electron charge, P_x is the polarization in x-direction, \mathbf{r}_i is the position vector of the i -th electron and x_i its x -component. For free electrons,

$$dx/dt = \int_{-\infty}^t E_x(t') dt', \quad (3.3)$$

and the cycle averaged energy absorption is zero. During the intense laser cluster interaction a macroscopic charge- and electric field-gradient builds up in and around the cluster, see figures 3.6(b1) and (b3). The resulting electric field leads to dephasing between laser field and polarization, and to nonlinear polarization terms, see figure 3.5. Both effects result in nonzero contributions to the cycle averaged integral L and therewith, cause LDH. Note that the basic mechanism of LDH is related to inverse Bremsstrahlung. However, whereas in inverse Bremsstrahlung, energy absorption is caused by the dephasing in the microscopic Coulomb field of an ion, LDH is caused by dephasing of electrons in the macroscopic electric field of the cluster.

3.4 Conclusion

Concluding a microscopic particle in cell (MPIC) code was introduced, which presents a powerful tool for the analysis of nanoplasmas. Calculations for clusters of up to $N = 25.000$ atoms have been performed, taking all microscopic

interactions into account. The simulations revealed good agreement with experiments and a complete picture of the explosion dynamics of large clusters. This progress was made possible by the fact that the numerical load of the MPIC code increases with N , whereas commonly used molecular dynamic codes scale as N^2 . The calculation of nanoplasmas with up to 10^6 atoms appears feasible on large scale computers. Finally, the MPIC concept presents a first step towards an exact kinetic theory of macroscopic plasma volumes with dimensions comparable to the (μm) laser wavelength.

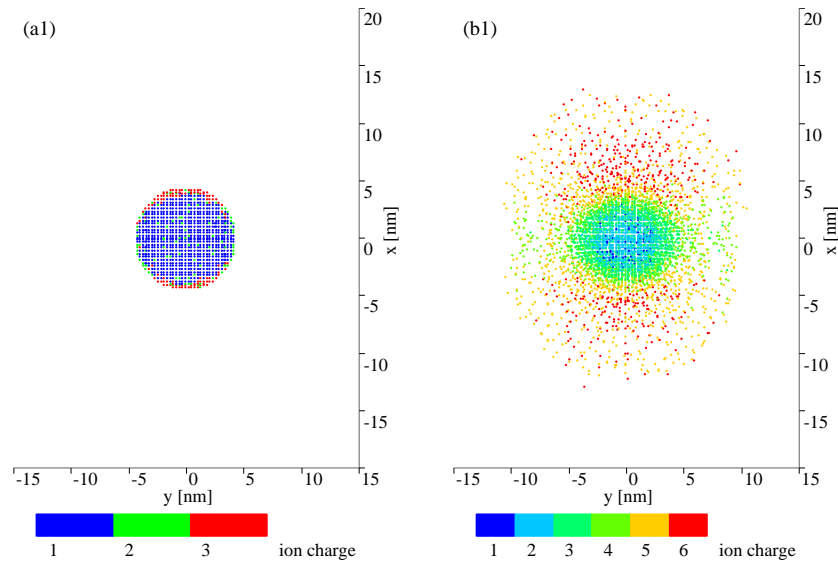


Figure 3.6: This figure shows the x-y plane going through the cluster center; (1) charge state of ions versus position, (2) position of ions (red dots) and electrons (blue dots), (3) electric field at the position of the ions for the parameters of figure 3.3; (a) and (b) refer to the times of observation $t = -92.9$ fs, -25.9 fs, where $t = 0$ marks the peak of the laser pulse. The laser intensities for (a) and (b) are $I = 4.4 \times 10^{14}$ W/cm² ($E = 5.7 \times 10^{10}$ V/m), and $I = 6.7 \times 10^{15}$ W/cm² ($E = 2.2 \times 10^{11}$ V/m), respectively.

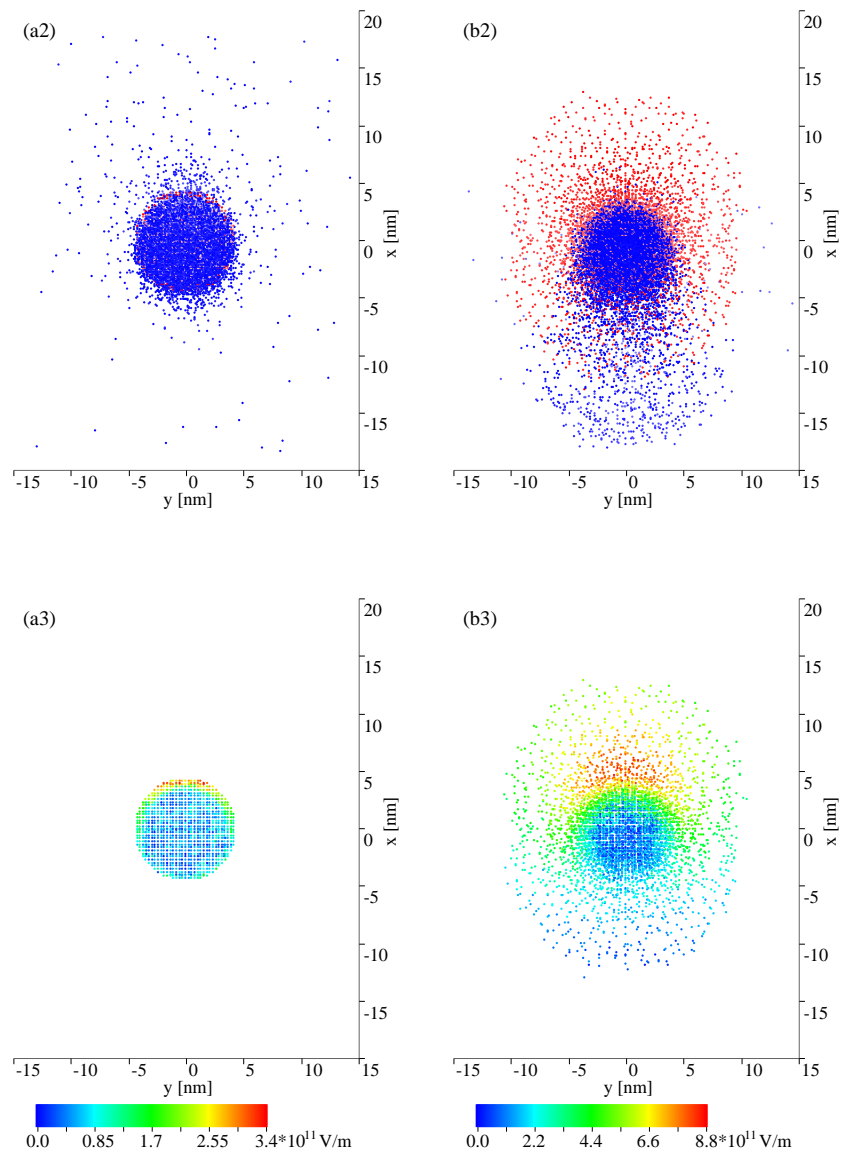


Figure 3.6: (continued)

Chapter 4

Charge state distribution of ions formed in Coulomb explosions of Argon clusters in intense laser fields

In this chapter the ion emission resulting from Coulomb explosion of highly-charged Ar_{40000} clusters is studied experimentally and numerically at laser intensities up to $10^{16}\text{W}/\text{cm}^2$. The experimentally measured ion emission spectrum shows a pronounced knee-like feature which defines the maximum energy of isotropically emitted ions in the Coulomb explosion. The variation of the knee energy with laser intensity is investigated using 3d MPIC simulations and enables deduction of the charge distributions of ions produced in the cluster explosion. It was found that more than 64% of the ions are produced in very high charge states (8+ or higher), an unexpected situation for intensities below $10^{16}\text{W}/\text{cm}^2$.

4.1 Introduction

The physics governing the disassembly of highly charged cluster ions has been of immense interest in the last decade [21], mainly because matter in the form of nanometer-sized clusters appears to be extraordinarily efficient at absorbing energy from an optical field when intense femtosecond pulses are used [92]. The absorbed energy is expended in creating a hot nanoplasma comprising clusters in very high charge states that, subsequently, Coulomb explode and give rise to ions and electrons that are very energetic [93]. The absorbed energy is also efficiently channeled into photoemission that extends from the vacuum ultraviolet (VUV) regime to the hard X-ray regime [21, 94]. The physics of such light-matter interactions has attracted attention not only from a fundamental viewpoint but

also due to a number of tantalizing applications. Several analytical and semi-analytical models have been developed in attempts to understand and rationalize the experimental observations [21]. Most recently, numerical computational methods, such as the three dimensional microscopic particle in cells (3d MPIC) technique, have been employed in identifying the dominant process involved in the cluster explosion dynamics. The growing importance of such techniques can be ascribed to their ability to numerically compute, in fairly successful fashion, experimentally observables like ion and electron emission spectra [11]. From the viewpoint of applications like tabletop acceleration schemes, recent experiments have indicated that energetic ions, possessing up to an MeV of energy, can be produced anisotropically with the direction of emission being controlled by the polarization vector of the incident linearly polarized laser radiation [87]. The possibility of accelerating D^+ beyond the D-D fusion threshold, giving rise to fusion yields that are comparable with those obtained in very large-scale experiments, provide further impetus to developing novel application schemes like a tabletop neutron source [95].

One of the new facets of the interaction of intense laser light with matter involves the possibility that intense soft X-ray laser beams might be produced upon irradiation by ultrashort infrared laser pulses. The ability to produce higher harmonics (non-linear orders of about 300 or more) has been successfully demonstrated by using femtosecond pulses that are of duration shorter than 10fs [96]. Use of hollow fiber columns to increase the efficiency of the harmonic generation is also starting to be exploited [4]. Most recently, the first experiments have been reported in which such harmonics are used as seed pulses that become amplified in a laser-produced plasma [97]. Transitions of highly charged ions like Kr^{8+} , that closely match with the 25th harmonic of the incident infrared laser, were utilized in these experiments. A multi-Terawatt laser beam, possessing up to a Joule of energy, was applied to produce large populations of Kr^{8+} ions that were used as the amplifying medium. One of the key elements that are essential in boosting these amplifiers is to efficiently populate sufficiently large fractions of ions that are in very high charge states. It is known that the threshold intensity for producing Kr^{8+} is 1.6×10^{16} W/cm² [98]. To produce large populations of Kr-atoms in charge states of 8+ or higher incident laser intensities that are more than an order of magnitude larger than this value become essential.

It is demonstrated that matter in the form of clusters might be a better amplifying medium due to the fact that, as already noted, a very large fraction of the energy from the incident optical field (in excess of 90%) can be absorbed in light-cluster interactions [92], giving rise to a multiply ionized nanoplasma whose disassembly might yield a larger than expected fraction of energetic ions in very high charge states. In this chapter the results of a combined experimental and theoretical study of the Coulomb explosion of Ar_{40000} clusters are presented indicating that it is possible to have more than 50% of the emitted argon ions in charge states of 8+ or higher. Krishnamurthy et al. report in [99] that the ion emission spectra in Coulomb explosions exhibit a ‘knee’ pattern which distinguishes isotropically-exploded ions from the anisotropically-emitted ions in higher charge states. They infer that the ‘knee energy’ denotes the max-

imum kinetic energy gained by those ions that are accelerated due to Coulomb repulsion of the total charge acquired on the cluster. The variation of the ‘knee energy’ as a function of the incident laser intensity for Ar_{40000} clusters is investigated in this chapter. The ‘knee energy’ variation essentially yields information on how the total Coulomb charge that is induced on the cluster varies as a function of the intensity of the incident optical radiation. A 3d MPIC method is used to numerically compute the ion spectra and these results are correlated with the experimental measurements.

4.2 Experimental and theoretical methods

The experimental apparatus that was used to make the measurements has been described in [93]. Briefly, the clusters were produced by a supersonic jet expansion system fitted with a $500\ \mu\text{m}$ nozzle. The cluster size was characterized by Rayleigh scattering measurements in conjunction with the use of the Hagen parameter [93, 94]. A $500\ \mu\text{m}$ skimmer was used to sample the central portion of the supersonic beam; the clusters were delivered into a differentially pumped chamber that was maintained at pressures in the range of 10^{-7} Torr. The intense laser pulses were obtained from a chirped pulse amplification system capable of delivering 100 fs duration pulses of 806 nm wavelength at an energy of up to 50 mJ. Typically, energies only up to about 10 mJ are used in the present series of experiments so that intensities up to $10^{16}\text{W}/\text{cm}^2$ within the laser focal volume could be readily achieved by employing a plano-convex lens of a focal length of 25 cm. Temporal correlation of the laser pulse with the gas pulse was achieved by externally triggering the laser and adjusting time delays between the laser trigger and the gas pulse trigger by means of a digital delay generator. The ion energy spectrum was deduced using conventional ion arrival time measurement techniques with a microchannel plate detector placed 58 cm downstream of the skimmer used for detecting the ions. Arrival times for the charged particles incident on the detector were measured with a 1 GHz digital storage oscilloscope.

The theoretical analysis is based on the MPIC approach [11]. The MPIC code calculates the motion of charged particles by solving Maxwell’s equations. In contrast to traditional PIC codes, here, each particle is represented by one cell. The box size in the MPIC code is chosen to be of the order of one atomic unit (a.u.). In this limit, the microscopic interactions of all charged particles are taken care of by the particle in cell formalism. The MPIC code contains no free parameters and presents a virtual experiment. In order to be able to calculate the explosion dynamics of clusters with $N = 40000$ atoms, a cell size of 4 a.u. is chosen. Convergence of the numerical results have been studied as a function of cell size by performing calculations with various cell sizes for a smaller cluster, with $N = 10000$. As long as the cell size is smaller than the interatomic distance within the cluster (≈ 7 a.u.), the influence of the cell size is found to be weak. This can be understood from the following argument. The charged particles are represented by boxes with uniform charge density,

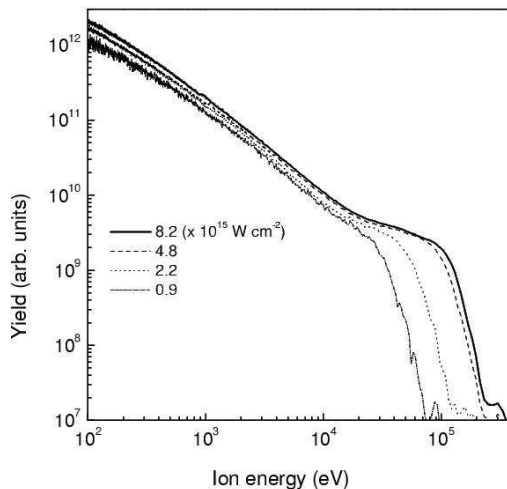


Figure 4.1: Experimentally measured ion energy spectra obtained when Ar_{40000} clusters are exposed to 100fs laser pulses with a wavelength of 806nm. The peak intensity varies from 0.9 to $8.2 \times 10^{15} \text{W/cm}^2$.

the size of which is equal to the cell size. The cell size defines the volume over which the Coulomb interaction between charged particles is shielded. Due to the shielding within the particle box the cell size defines the smallest impact parameter at which inverse bremsstrahlung can take place. Therefore, the box size of the particle defines the degree to which inverse bremsstrahlung is taken into account. The weak dependence on the cell size results from the fact that inverse bremsstrahlung heating plays only a minor role in infrared laser-driven explosions of large clusters [11].

4.3 Results and discussion

In [87] it has been established that ion emission from the Coulomb explosion of clusters like Ar_{40000} gives rise to an energy distribution function that has two components: an isotropic component and an anisotropic high energy component, with a knee-like feature that distinguishes the two different slopes in the ion emission spectra. From previous experiments it has been found that the ‘knee energy’ denotes the *maximum* that the emitted ions can obtain from pure Coulomb explosions of the cluster nanoplasma. The ‘knee energy’ E_{knee} is represented by

$$E_{knee} \propto \frac{Q\bar{q}n_c}{R}, \quad (4.1)$$

where \bar{q} is the average charge per atom in a cluster of radius R with n_c atoms, and Q is the charge on the ion that is detected.

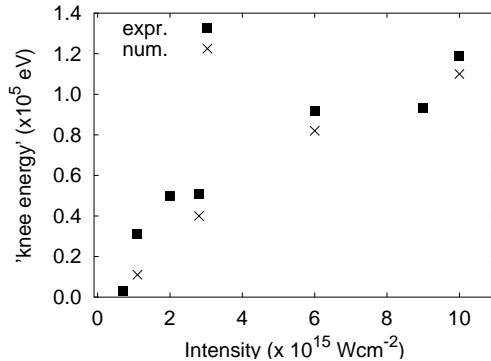


Figure 4.2: Comparison of experimentally (expr.) and numerically (num.) obtained knee energies for different laser peak intensities. The pulse duration was 100fs and the wavelength set to 806nm.

In this chapter results of experiments are presented that probe how the ion emission spectrum changes with the incident laser energy. In particular, it is examined how the magnitude of the ‘knee energy’ varies with the incident laser intensity for Ar_{40000} . Figure 4.1 shows typical ion kinetic energy spectra that are obtained when Ar_{40000} clusters are irradiated by laser pulses with four different values of peak laser intensity. When the laser intensity is lowered the value of the ‘knee energy’ is also lowered, even though the general shape of the ion energy distribution function remains the same. The unaltered cluster size in the four spectra depicted in figure 4.1 indicates that the decreased intensity of the ‘knee energy’ that is observed is essentially due to the decrease in \bar{q} for lower intensities. Thus, these measurements can be used to determine how the ‘charging’ of the cluster changes as the intensity of the incident laser pulses is varied. In figure 4.2 the change in the ‘knee energy’ that is measured for a number of different incident laser intensities is shown. The results depicted here contain a more specific signature of how the charge on the cluster increases with the incident laser intensity.

Several analytical models have been proposed to understand the dynamics of cluster ionization and cluster explosion [21]. The degree of ionization in the cluster has been shown to increase with the dimensionless field strength parameter x ; the degree of ionization saturates at unity as $x \rightarrow 1$. The field strength parameter is defined as

$$x = \frac{ER^2}{nZ}, \quad (4.2)$$

where E is the time-dependent external field strength, that is both due to the incident laser field and the electrostatic field experienced by the cluster, n denotes the number of atoms in the cluster of radius R , and Z is the charge multiplicity of the atomic ions within the cluster. Although predictions based on such simpli-

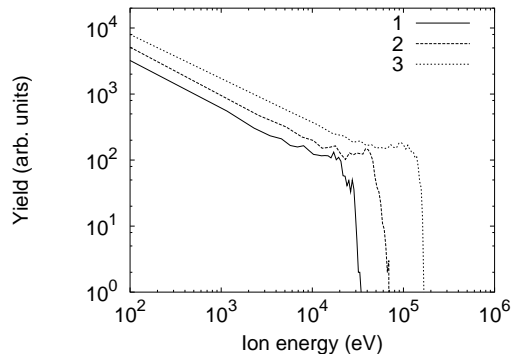


Figure 4.3: Simulated ion energy spectra for Ar_{40000} clusters irradiated by a laser pulse with a wavelength of 806nm and a pulse duration of 100fs. The laser peak intensity for (1), (2), and (3) was 10^{15} , 3×10^{15} , and $10^{16} \text{W}/\text{cm}^2$, respectively.

fied analytical models exist in literature, there has been very little experimental information on the charging of clusters to correlate measured information with such models. The 3d MPIC simulations reveals that the explosion of Ar_{40000} is driven in two steps. At first, the neutral cluster atoms are ionized (inner ionization) but the electrons remain confined within the cluster by the positive field of the ions. Inner ionization is a mixture of electron impact ionization and tunnel ionization that is enhanced by the presence of positively charged neighbor ions. Charge states of up to 11+ are created in the simulations. In a second step, the ejected electrons are heated and leave the cluster when their kinetic energy exceeds the binding energy of the cluster (outer ionization). The extent of outer ionization determines the positive space charge that is created within the cluster and, therewith, the force that acts on the exploding ions and, hence, the final kinetic energy that the ejected ions possess. Outer ionization is driven by laser dephasing heating, where the macroscopic electric field of the cluster causes dephasing between the laser driven motion of the electrons and the laser field which allows electrons to absorb energy from the laser.

Figure 4.3 shows simulated ion energy spectra for an Ar_{40000} cluster interacting with laser pulses of intensities of up to $10^{16} \text{W}/\text{cm}^2$. The ion emission spectra show a knee-like feature. Furthermore, the simulations show that the value of the ‘knee’ energy decreases as laser intensity is lowered. Both these results are in accord with the experimental measurements.

With the establishment of the excellent correlation between the results from the experiments and the simulations, the computational results can be used to obtain the charge state distributions of the ions in the cluster. Figure 4.4 shows how the charge state distributions of the atomic ions change with the incident laser intensity. As the laser intensity is increased a larger propensity to produce

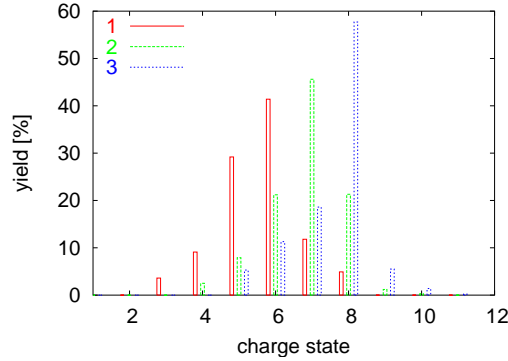


Figure 4.4: Computed charge distribution of argon ions formed when Ar_{40000} clusters are exposed to laser pulses with a pulse duration of 100fs and a wavelength of 806nm. For (1), (2), and (3) the laser peak intensity was 10^{15} , 3×10^{15} , and 10^{16}W/cm^2 , respectively.

ions in higher charge states can be observed. At a laser intensity of 10^{16}W/cm^2 every atom in the cluster is ionized and, most significantly, more than 64% of the ions are found in charge state 8+ or higher. The sharp drop in the yield of ions beyond charge state 8+ is due to shell effects that bring about a large rise in the ionization energy of Ar^{8+} compared to that of Ar^{7+} .

In a cluster explosion at intensities similar to those used in the experiments reported here, it is indeed very difficult to obtain quantitative information of the charge states of *all* ions emitted in the Coulomb explosion. The difficulty lies in the fact that ions are emitted with a very wide range of energies, ranging from a few eV to values that lie close to one MeV. Most of the experiments that have reported the measurement of charge state distributions [100, 101] have been measurements only of ions that possessed large values of kinetic energy. In arrival time measurements, or energy measurements that rely on the Thompson parabola, low energy ions (that may be multiply charged) are discriminated against and/or are detected with very low efficiency. A large fraction of ions that possess energies of only a few hundred eV, or less, escape measurement due to the low efficiency of detectors for such ions, or due to the low transmission efficiency for such ions through the energy filter, or by virtue of encountering electronic difficulties in reliably measuring large arrival times that are taken by low-energy ions. This may well be the reason why strong shell effects have not been unambiguously observed in earlier experimental measurements.

4.4 Conclusion

From the viewpoint of the applications, which were mentioned in the introduction of this chapter, that seek to use laser plasmas to produce highly charged

ions to be used as an amplifier medium, it is important to have knowledge of the charge distribution of all the ions that are formed in the cluster. This study shows that even at relatively modest intensities that are less than $10^{16}\text{W}/\text{cm}^2$ a population distribution is obtained where more than 64% of the total atoms are in charge states 8+ and higher. This might be considered to be a somewhat unexpected result because the intensity threshold for observing Ar^{8+} in low density (atomic) gases is at least $2.3 \times 10^{16}\text{W}/\text{cm}^2$ [102]. It might well be that clusters turn out to be the best option to produce large populations of the very highly ionized atoms for subsequent use as amplifying media.

Chapter 5

Plasma physics in the strong coupling regime: Intense soft X-ray cluster interaction

In this chapter the interaction of noble gas clusters with intense soft X-ray radiation is investigated by molecular dynamics simulations. It is shown that the free electron laser cluster interaction creates a strongly coupled plasma. A new heating mechanism is identified that explains the observation of unusually high charge states in recent experiments at DESY. The heating mechanism is a consequence of the strongly coupled plasma dynamics in which collisional processes are strongly modified.

5.1 The Experiment, and What is known

The first X-ray free electron laser (XFEL) experiments in the soft X-ray regime, with photon energy of 12.7eV and unprecedented peak intensities of nearly $10^{14}\text{W}/\text{cm}^2$, were recently performed at DESY [103]. Unexpectedly, when cold Xe clusters were exposed to such radiation, high ion charge states up to Xe^{8+} were observed. This has raised considerable interest, as the high charge states cannot be explained by conventional ionization nor heating mechanisms.

The XFEL intensity is too low for nonlinear processes, such as multi-photon ionization, to create charge states up to $8+$. Heating by a plasmon resonance was ruled out experimentally [104]. Laser dephasing heating [11], the macroscopic mechanism responsible for light absorption of clusters exposed to near-infrared lasers, must be ruled out as well, as it requires a free electron quiver motion amplitude that extends over a significant fraction of the cluster. The maximum quiver amplitude reached in the DESY experiment is below 1 Bohr.

A strong candidate for high charge state creation is inverse Bremsstrahlung heating (IBH) of the valence electrons set free by single-photon ionization, and subsequent impact ionization of deeper bound electrons. However, it has been shown recently that conventional IBH rates are an order of magnitude too low to account for the observed charge states [105, 106].

5.2 Results

The key to understanding the DESY experiment is the observation that the intense soft X-ray pulse creates a strongly coupled electron-ion plasma. This is the first major result of this chapter. A strongly coupled plasma (SCP) appears in the limit of high density and low temperature [107]. In conventional weakly coupled plasmas fluctuations resulting from the discrete nature of charges, and therewith collisions and Coulomb correlations, are kept at a low level through Debye shielding. In SCPs however, statistical mean field interactions are dominated by the microscopic nature of the Coulomb interaction. Strong coupling can exist between ions, between electrons, and between electrons and ions. Most of the investigations so far were performed in plasmas with strongly coupled ions. The creation and investigation of strongly coupled electron plasmas is one of the goals of ultra-cold plasma physics. However this has not been successful so far, as heating effects make the creation of strongly coupled electron-ion plasmas challenging [108, 109, 110]. In contrast, strong coupling between electrons and ions, and between electrons, is maintained in the DESY experiment over the laser pulse duration, as electron heating is offset by an increase in free electron density by impact ionization. Therewith, intense soft X-ray sources present a powerful, novel tool for the investigation of strongly coupled electron plasmas.

The second major result is that energy absorption in a SCP is dominated by a novel heating mechanism termed many-body recombination heating (MRH). It was found that for the parameters of the DESY experiment, MRH is an order of magnitude stronger than IBH. A schematic of MRH is depicted in figure 5.1. In a SCP, ion-electron correlation increases the probability of finding one or more electrons in the vicinity of an ion [111]. Due to the larger local density around the ions, many-body (i.e. multi-electron ion) collisions become much more likely. Many-body collisions result in an enhanced recombination of electrons to excited bound states, see figures 5.1(a) and (b). This process was termed many-body recombination (MR). In a SCP, MR is much more efficient than three-body recombination in a weakly coupled plasma. As figure 5.1 illustrates, the remaining free electrons absorb the energy set free during the electron transition to the bound excited state (b). Further collisions either reionize the recombined electron or scatter it from highly excited into deeper bound states. As a result, a broad range of the excited state spectrum is populated. The MRH-cycle is closed when the recombined electron is re-ionized by photon absorption (c). As the recombined electrons revolve continuously around an ion, light can be absorbed much more efficiently than in IBH, where free electrons first need to find an ionic partner to absorb radiation.

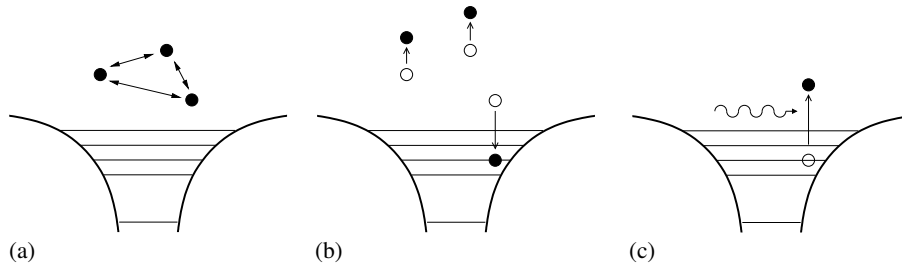


Figure 5.1: Schematic of MRH. MRH takes place in a cycle consisting of three processes. Collisions of two or more electrons close to an ion (a) result in MBR to a Rydberg state (b). The total energy of the multi-electron-ion system remains conserved (b). Energy is absorbed when the Rydberg electron is re-ionized by photon absorption (c).

The XFEL cluster interaction was modelled through a treecode [12] which scales more favorably ($\mathcal{O}(N \log N)$) with the number of particles N than a direct molecular dynamics (MD) approach ($\mathcal{O}(N^2)$). The better scaling is achieved by approximating the force of a group of distant particles by a multipole expansion. Expansion terms are included up to a quadrupole order. The distance at which the exact Coulomb interaction is approximated by the multipole expansion is determined by a tolerance parameter Θ , defined e.g. in [63]. In the limit of $\Theta = 0$, the tree-calculation becomes an exact MD analysis. To eliminate numerical heating, a shielded electron and ion Coulomb potentials with a shielding radius of 1 Bohr are used. The results are insensitive to a further reduction of the shielding parameter. Convergence of the presented calculations is obtained for $\Theta = 0.3$ and a timestep $\Delta t = 5 \times 10^{-20}$ s. A further decrease of Δt or Θ changes electron kinetic energies and ion charge states by less than 3%.

The simulation begins with a set of neutral Xe-atoms in fcc-structure with an interatomic distance $d = 8.2$ Bohr. Individual electrons and ions are created through ionization. When an electron is removed from its ground state, the charge of the ion is increased by one. In the DESY experiment, single photon ionization is the predominant process for the ionization of the first electron. Quantum mechanical single photon ionization rates for the Xe ground state are taken from [41]. The subsequent electrons bound in ionic ground states are ionized by impact ionization as determined by the Lotz cross section [42], where the single atom/ion ionization potential is used. This presents a lower bound to impact ionization in solid density plasmas since in a positively charged cluster the net field of the ions reduces the ionization potential. The clusters investigated here are weakly charged, which makes the use of the unperturbed ionization potential a reasonable approximation.

Ionization does not only take place from the atomic or ionic ground state. Due to collisions, free electrons may recombine to ionic excited bound states, from where they can again be ionized. Once an electron is created initially, it

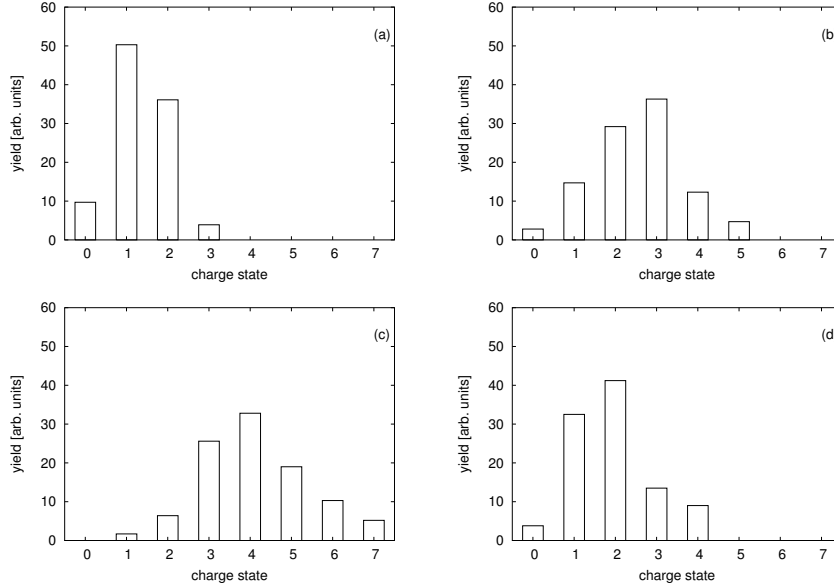


Figure 5.2: Ion charge state distributions of a Xe cluster interacting with a XFEL pulse with $\lambda = 98\text{nm}$ and full width half maximum of 100fs. A sin-squared pulse envelope was used; (a) - (c) Xe_{1000} and intensities of $1.5 \times 10^{12}\text{W/cm}^2$, $1.5 \times 10^{13}\text{W/cm}^2$, and $7 \times 10^{13}\text{W/cm}^2$, respectively; (d) Xe_{80} and an intensity of $1.5 \times 10^{13}\text{W/cm}^2$. No averaging over the transversal pulse profile was done.

remains in the calculation, even during recombination with an ion. Recombination and reionization are fully contained in the classical calculation.

The analysis focuses on a Xe_{1000} cluster. This is somewhat smaller than the Xe_{1500} clusters used in the DESY experiment [103], but is at the limit of available computer capacity. The parameters are close enough to the DESY experiment to allow a reasonable qualitative comparison. A quantitative comparison is difficult in any case due to the large uncertainty in the measurement of cluster size, XFEL pulse shape, and peak intensity [112].

The Xe ion distribution for a Xe_{1000} cluster with intensities of $7 \times 10^{13}\text{W/cm}^2$, $1.5 \times 10^{13}\text{W/cm}^2$, $1.5 \times 10^{12}\text{W/cm}^2$, and for a Xe_{80} cluster with an intensity of $2 \times 10^{13}\text{W/cm}^2$, is plotted in figures 5.2(a)-(d) respectively. All calculations used $\lambda = 98\text{nm}$, and an FWHM of 100fs. A reasonable agreement was found between the calculations and figures 1 and 2 of [103], see figures 5.5 and 5.3. In (a) and (b) charge states up to 3 and 5 are created, respectively, in agreement with the DESY experiment. In (c) we observe ions up to Xe^{7+} , which is one charge state lower than observed in the experiment. In general, the calculated distribution functions peak around higher charge states than in the experiment.

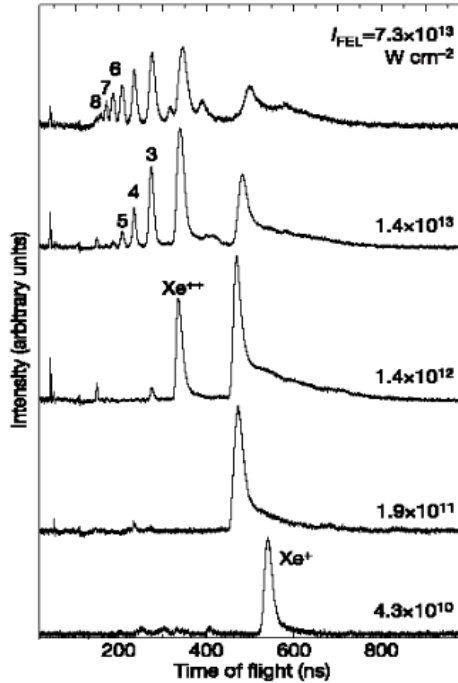


Figure 5.3: TOF mass spectra recorded after irradiation of a Xe_{1500} cluster as a function of power density after Wabnitz et al. [103].

This is because the calculations are not averaged over the transversal intensity distribution of the pulse. Such averaging would shift the population towards lower charge states, further improving the agreement.

The creation of "intermediate" charge states up to $8+$ has been suggested as a mechanism for enhancing IBH in the Xe_{80} cluster [106] (figure 5.2(d)). These high charge states are created in the following way. The field of surrounding ions lowers the ionization barrier to an extent that single photon ionization can also take place from deeper bound states. It is arguable that this is the dominant mechanism. First, most of the field of adjacent ions is shielded by ionized electrons. The DESY clusters are weakly charged. As a result barrier suppression is too weak to account for a substantial creation of high charge states. Second, although ionization barrier lowering is neglected, a highest charge state of $4+$ in agreement with the Xe_{80} DESY experiment is obtained.

Alternatively, it has been proposed that non-Coulomb contributions to electron-ion collisions enhance IBH [105], since near the atom the positive charge of the nucleus is not completely shielded by the bound electrons. It is also arguable that this is the dominant mechanism. First, enhanced IBH has been imbedded within a plasma dynamics calculation valid only for weakly coupled plasmas

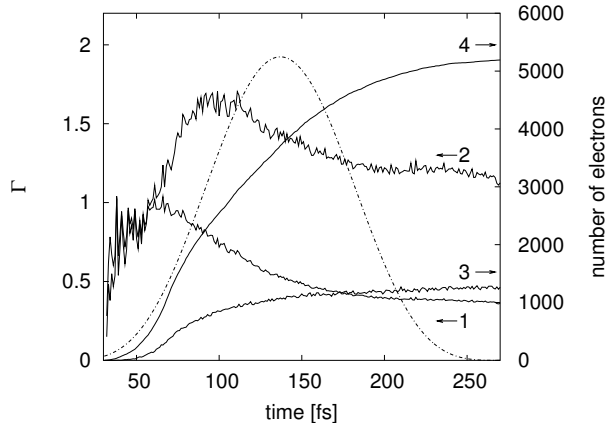


Figure 5.4: Graphs (1) and (2) denote the electron-electron (Γ_{ee}) and electron-ion (Γ_{ei}) coupling parameter versus time, respectively, for the parameters of figure 5.2(c). Graphs (3) and (4) show the number of electrons bound in a Rydberg state and the total number of (ionized) electrons created during the calculation, respectively. The dash-dotted line indicates the XFEL pulse shape.

close to thermodynamic equilibrium. Second, the electron-ion Coulomb interaction provides sufficient electron heating to obtain the high charge states observed in the DESY experiment.

To demonstrate that the XFEL driven cluster dynamics takes place in the SCP regime, in figure 5.4 are plotted the electron-electron, $\Gamma_{ee} = V_{ee}/k_B T_e$, and the electron-ion, $\Gamma_{ei} = Z\Gamma_{ee}^{3/2}$, coupling parameters as a function of time [111]. The parameters of 5.2(c) are used. Here, Z denotes the average ion charge state, $k_B T_e$ the average thermal energy, and $V_{ee} = e^2/(4\pi\epsilon_0 a)$ the average electrostatic energy between neighboring electrons. The average distance between electrons $a = (3/(4\pi n_e))^{1/3}$ is determined by the electron density n_e . The parameter Γ_{ei} represents the ratio of ion charge to electron charge within the Debye-sphere. The Debye length $\lambda_d = (\epsilon_0 k_B T_e / (e^2 n_e))^{1/2}$ determines the length over which charge fluctuations are screened by the electron plasma. A plasma is strongly coupled when $\Gamma_{ee} \gtrsim 0.1$ and $\Gamma_{ei} \gtrsim 1$ [111]. From figure 5.4, it can be seen that both coupling parameters fulfill the conditions for a SCP. Although laser heating increases the electron temperature to 25eV after the laser pulse, the strong coupling is maintained throughout, since a higher electron temperature results in an increase in electron density through impact ionization. The kinetic energy distribution is non-Maxwellian with the hottest electrons around 100eV.

In a SCP large Coulomb correlations build up since ions have the tendency to gather free electrons around them (see figure 5.6). This also happens in the system simulated. Analysis of the cluster dynamics for the parameters of figure

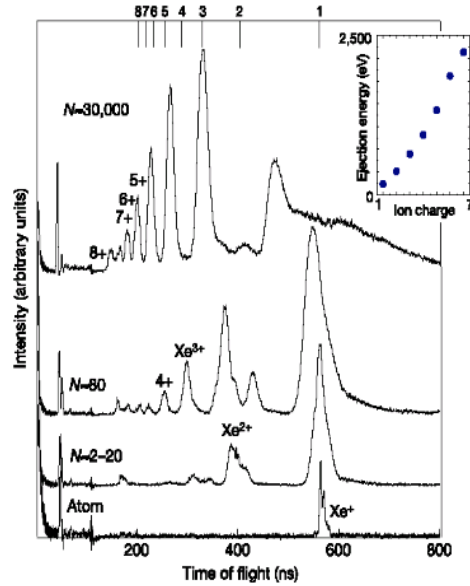


Figure 5.5: Time-of-flight (TOF) mass spectra of ionization products of Xe atoms and clusters after Wabnitz et al. [103]. The average power density was $2^{13}\text{W}/\text{cm}^2$ and the wavelength 98 nm. The cluster size varied from $N = 2$ to up to $N = 30000$.

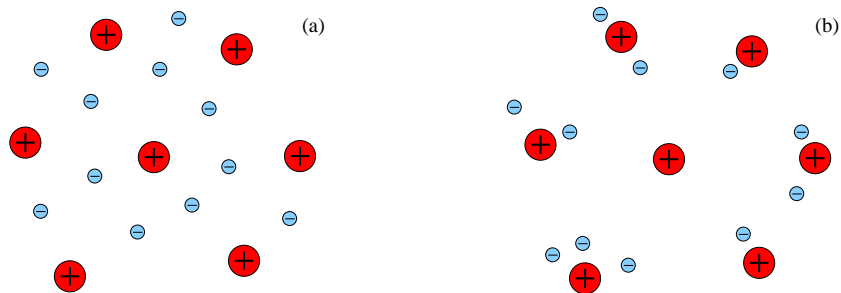


Figure 5.6: Schematic illustration of a weakly (a) and a strongly (b) coupled plasma. In weakly coupled plasmas electrons are equally distributed over space keeping collisions and Coulomb interaction at a low level through Debye shielding. Whereas in strongly coupled plasmas ions have the tendency to gather free electrons around them resulting in a build up of large Coulomb correlations.

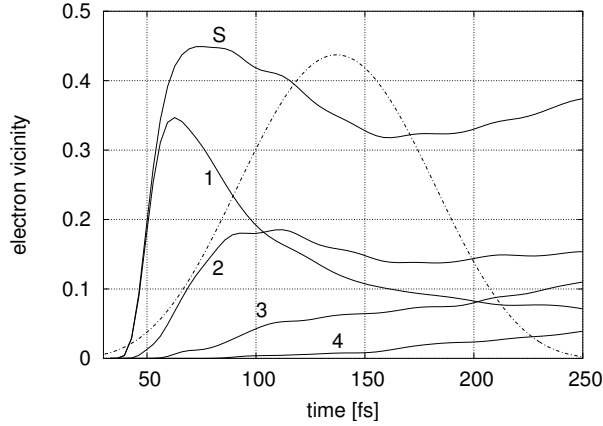


Figure 5.7: Probability to find an electron close to an ion versus time for a Xe_{1000} cluster and pulse parameters as defined in figure 5.2(a). Graphs (1)-(4) show the probability w_n to find an electrons around an ion which has $n - 1$ further electrons in its vicinity. Graph (S) is the sum over graphs (1)-(4). The dash-dotted line indicates the XFEL pulse shape.

5.1(c) reveals that the probability to find one electron in a detection sphere of radius $d/4$ around an ion is much higher than in the uncorrelated case, where the electrons are spread with equal probability over the cluster volume. This can be seen in figure 5.7, where the time evolution of the probability w_n to find an electron in the vicinity of an ion is plotted for the parameters of figure 5.2(a). The probability is determined from the number of electrons being in a detection sphere of radius $a/4$ around an ion normalized to the total number of created electrons. The n in w_n stands for the number of electrons in the vicinity of the ion the electron is close to. This means that w_1 gives the probability that an electron is close to an ion and that it is the only electron in its vicinity. w_2 represents the probability that an electron is close to an ion and there is a second electron in the vicinity of the ion, and so on. The ratio of detection volume to total volume is ≈ 0.1 (for details see appendix B). Graphs (1)-(4) show the probability w_n to find an electrons around an ion which has $n-1$ further electrons in its vicinity. The maximum number of electrons found around an ion in the simulation is five. Graph (S) is the sum over graphs (1)-(4) and represents the probability to find at least one electron in the vicinity of an ion. The affinity of the electrons to gather around ions is surprisingly strong. Over most of the laser pulse every fourth electron is found together with one or more electrons in the vicinity of an ion. This clearly demonstrates a strongly coupled plasma dynamics creating high order correlations between electrons and ions.

In order to get a measure of the correlation, the probabilities in figure 5.7 have to be compared with the uncorrelated limit. This is done in figure 5.8. This

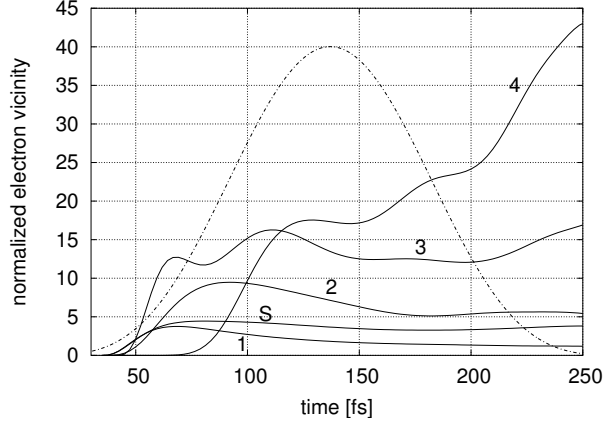


Figure 5.8: Normalized electron vicinity probability w_n/p_n versus time for a Xe_{1000} cluster and pulse parameter as defined in figure 5.2(a). w_n is the probability retrieved from the simulation to find an electron close to an ion which has $n - 1$ further electrons in its vicinity. p_n is the same probability for an uncorrelated plasma. The dash-dotted line indicates the XFEL pulse shape.

figure contains the normalized probabilities w_n/p_n , where p_n is the probability that an electron is close to an ion when the electrons are uniformly spread over the volume. For the calculation of the probabilities p_n the same number of ions N_i and electrons N_e are used as were detected in the correlated case. A combinatorial analysis gives the probability

$$p_n = \frac{n}{N_e} N_i \binom{N_e}{n} p_i^n \sum_{l=0}^{N_e-n} p_i^l \bar{p}_o^{N_e-n-l} (N_i - 1)^l \binom{N_e - n}{l} \quad (5.1)$$

to find an electron close to an ion, which has $n-1$ further electrons in its vicinity. For a detailed derivation of the probability p_n see appendix B. Graphs (1)-(4) of figure 5.8 show the normalized probability w_n/p_n to find $n = 1 - 4$ electrons around an ion. Graph (S) of figure 5.8 is the normalized sum of the probabilities. Figure 5.8 shows that it is up to four times more likely to find an electron close to an ion which has no other electron in its vicinity than in the uncorrelated plasma. For more electrons around an ion the normalized probability is even higher. For $n = 4$ it is up to 45 times higher.

As a result of the strong electron-ion correlation, many-body collisions between several electrons and an ion are much more likely to occur, often leading to MR to excited bound states. Graphs 3 and 4 in figure 5.4 show the number of electrons recombined to an excited bound state, and the total number of ionized (and of ionized-and-recombined) electrons as a function of time. At the peak of the laser pulse every fourth ionized electron is found to have recombined to an excited bound state. The distortion of the Coulomb potential by the rapidly

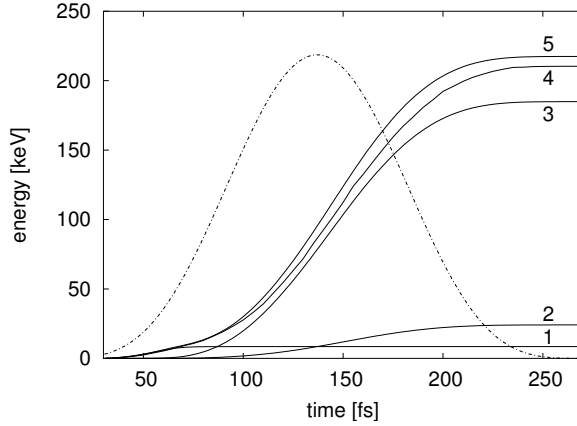


Figure 5.9: Energy absorption versus time for various heating mechanisms for the parameters of figure 5.2(c); graph (1) single photon absorption, graph (2) IBH, graph (3) MRH, graph (4) sum over graphs (1)-(3), graph (5) total energy absorption as calculated from the MD analysis. The dash-dotted line indicates the XFEL pulse shape.

fluctuating field of the adjacent electrons makes it difficult to identify an excited bound electron from its total energy. Therefore, they were identified in a two-step process. First, the total energy of an electron in the vicinity of an ion is calculated by using the single-ion Coulomb potential. Second, when the total energy is negative, the electron is observed over 1fs. The electron is counted as a bound electron, when it remains in the vicinity of the original ion or its nearest neighbors during this time interval. This takes into account extended, molecule-like excited states that can exist due to the complex potential energy structure of the cluster. An electron with a thermal kinetic energy of 1eV traverses the interatomic distance d in a time interval < 1 fs. The number of free electrons that remain in this vicinity for a time longer than 1fs is negligible.

The importance of MR is shown in figure 5.9, where the energy absorption for the parameters of figure 5.2(c) is plotted. Graph 5 shows the total absorbed energy obtained directly from the simulation. In order to identify the dominant light absorption process, in graphs 1-3 of figure 5.9 are plotted the absorption from the individual heating processes that are found to be the most relevant. Graphs 1 and 2 show the energy absorption due to single photon ionization and IBH, as calculated from the rates in [41, 28], respectively. In the calculation of IBH the average ion charge state and the thermal velocity extracted from the simulation were used. The total light absorption is close to an order of magnitude more efficient than is predicted by IBH. Graph (3) shows the energy absorbed by electrons recombined to excited states, which is about an order of magnitude larger than (1) and (2). This shows that MRH provides the

bulk of the cluster heating. As collision physics is changed so profoundly in SCPs, it is not surprising that IBH is no longer the dominant light absorption mechanism. Graph (3) was determined in the following way. First, the number of electrons recombined to an ion with charge state Z as a function of time from the simulation was used. Next, the photo absorption rate as a function of Z , binding energy, and angular momentum was obtained from classical analysis. The rate was averaged over angular momentum and binding energies extending from the first excited state to 10% of the first excited state. The resulting rate depends only weakly on the boundaries of the energy interval. The energy absorption was calculated by multiplying the number of electrons bound in an excited state of a Z ion with the appropriate Z -dependent photo-absorption rate, then summing over all charge states. Finally, graph 4 plots the total absorbed energy obtained by adding graphs 1-3. The good agreement with graph 5 corroborates the fact that the three heating mechanisms depicted by graphs 1-3 largely determine the total energy absorption.

5.3 Conclusion

In conclusion, the analysis reveals that intense soft X-ray sources can create strongly coupled plasmas. Dynamics in strongly coupled plasmas is dominated by high-order correlations between electrons and ions. Strongly coupled plasmas occur in diverse areas of physics, ranging from plasma dynamics in giant planets, white dwarfs and progenitors of super novae [113] to quark-gluon plasmas created in high energy ion collisions [114]. A controlled laboratory-scale creation of strongly coupled electron-ion plasmas and their investigation will greatly benefit these areas. The recent availability of X-ray free electron lasers opens a new window of opportunity for the systematic investigation of strongly coupled plasmas. This is demonstrated by the finding that absorption of electromagnetic radiation is dominated by a new mechanism termed many-body recombination heating. The resulting enhanced energy absorption is an order of magnitude more efficient than conventional inverse Bremsstrahlung heating, and explains the observation of unexpectedly high charge states in recent intense X-ray cluster interaction experiments performed at DESY. Many-body recombination heating might also be a key mechanism in other wavelength regimes, determining e.g. the damage threshold of the near-infrared laser induced breakdown of solids. This will be subject of future investigations.

Chapter 6

Conclusion and outlook

To conclude two numerical tools for the investigation of nanoplasmas have been introduced in this work. On the one hand, a microscopic particle in cell (MPIC) code which has been used to perform simulations with clusters of up to $N = 40.000$ atoms. On the other hand, a treecode which approximates the force of a group of distant particles by a low-order multipole expansion. Using a treecode, simulations of clusters with up to 1.000 atoms have been performed. Both of the introduced tools have their advantages and disadvantages. The MPIC code is more sensitive to numerical heating whereas the current limit of treecodes lies at a cluster size of $N = 1.000$, which is about 2 to 3 orders of magnitudes less than for MPIC codes.

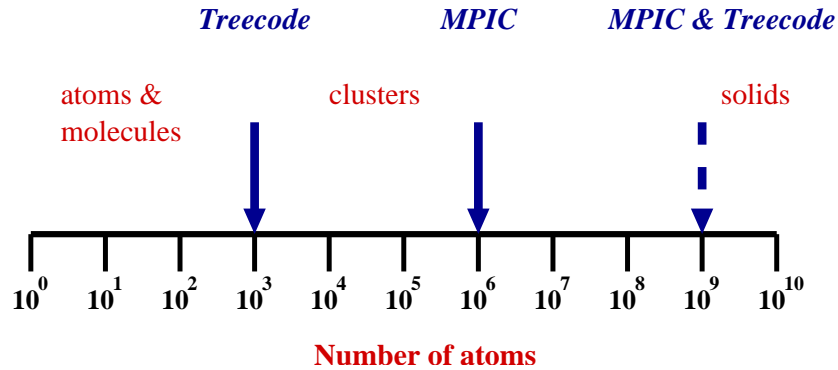


Figure 6.1: Schematic illustration of current limits of treecodes and MPIC codes regarding the number of particles which can be simulated. Recent studies and analyses show that a combination of treecode and MPIC code together with the fast growing computing power could shift this limitation to macroscopic systems with up to 10^9 atoms which means that solids can be simulated microscopically.

An extensive scope of work remains for the future, among it to combine the best features of MPIC codes and treecodes. Recent investigations show that a new algorithm using a treecode in near field and a MPIC approach in far field combined with the rapid development in computer processing power and high bandwidth and low latency interprocess communication will shift the limit of computable problems to systems with up to 10^9 atoms (see figure 6.1). This will be the next step towards the final goal which is to simulate dynamics of intense laser-induced phase transitions in macroscopic systems.

Appendix A

$N \log(N)$ -scaling of treecodes

According to Hernquist [115], the computational costs of tree simulations scale as $\sim \mathcal{O}(N \log(N))$. If N is the number of particles and as long as the fixed tolerance parameter $\Theta \gtrsim 0.3$. Hernquist demonstrates the $N \log(N)$ -scaling by using a simplified geometry. As described in chapter 2.2 the internal structure of a cell is ignored if

$$\frac{s}{d} \leq \Theta. \quad (\text{A.1})$$

Otherwise the criterion is recursively applied to the daughter cells. Figure A.1 shows a homogeneous sphere of particles which is subdivided in concentric shells. Each shell contains cells which obey the tolerance parameter for a particle at the center of the sphere. The cell size increases with the radius since the size is determined by equation A.1. According to figure A.1 equation A.1 can be rewritten as

$$\frac{s}{d} = \frac{r_i \Theta}{r_i} = \Theta. \quad (\text{A.2})$$

Assuming a homogeneous particle distribution the particle density can be obtained by

$$n = \frac{N}{\frac{4\pi}{3} R^3}, \quad (\text{A.3})$$

where R is the radius of the whole system. Considering a single particle at the center of a sphere the number of interactions can be estimated by the following expression

$$n_{tot} = n_0 + n_{cells}, \quad (\text{A.4})$$

where n_0 is the number of direct interactions resulting from particles inside the sphere with radius r_1 . n_{cells} is the number of cells, where the criterion is obeyed. According to figure A.1 n_{cells} is given by

$$n_{cells} = \sum_{shells} n_{sub}^i, \quad (\text{A.5})$$

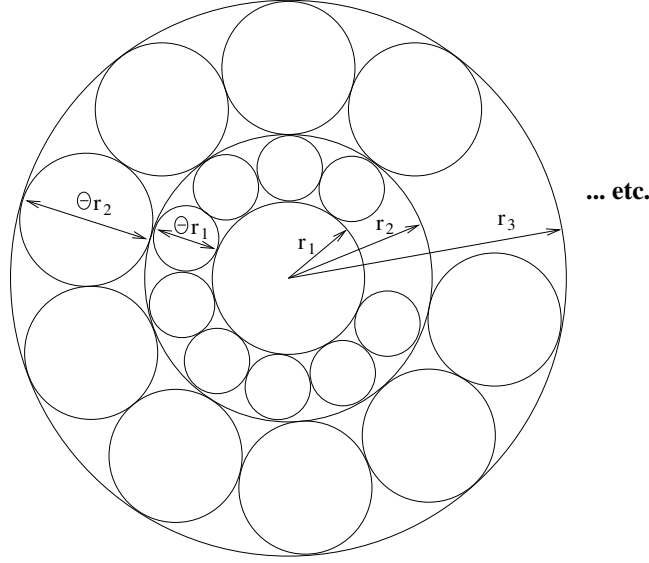


Figure A.1: Schematic representation of the force computation on a particle at the center of a homogeneous sphere of particles using a hierarchical method (from Hernquist [115]).

where n_{sub}^i is the number of cells per shell. n_{sub}^i is approximately given by

$$n_{sub}^i \approx \frac{4\pi r_i^3 \Theta}{\frac{4\pi}{3} \frac{1}{8} r_i^3 \Theta^3} = \frac{24}{\Theta^2}, \quad (\text{A.6})$$

Hence n_{tot} is roughly given by

$$n_{tot} \approx n_0 + \frac{24}{\Theta} n_{shells}, \quad (\text{A.7})$$

where n_{shells} is the total number of shells. The number of direct interactions in the sphere can be calculated by

$$n_0 = n \frac{4\pi}{3} r_1. \quad (\text{A.8})$$

Since r_1 is the radius at which clustering begins, it is approximately determined by

$$r_1 \approx n^{-1/3} / \Theta. \quad (\text{A.9})$$

Using equation A.9 we obtain

$$n_0 = \frac{4\pi}{3} \frac{1}{\Theta^3}. \quad (\text{A.10})$$

The next step is to determine the number of shells. The radius of a shell is

$$r_i = (1 + \Theta)r_{i-1} = (1 + \Theta)^{i-1}r_1, \quad (\text{A.11})$$

implying

$$\frac{r_{n_{shells}}}{r_1} = (1 + \Theta)^{n_{shells}-1}. \quad (\text{A.12})$$

Keeping in mind that the system radius R obeys

$$R = (1 + \Theta)r_{n_{shells}}, \quad (\text{A.13})$$

which gives the number of shells as follows

$$\begin{aligned} n_{shells} &= 1 + \log_{(1+\Theta)} \frac{r_{n_{shells}}}{r_1} \\ &= 1 + \log_{(1+\Theta)} \frac{R}{(1 + \Theta)r_1} \\ &= 1 + \log_{(1+\Theta)} \left(\frac{\Theta}{1 + \Theta} \left(\frac{3N}{4\pi} \right)^{1/3} \right). \end{aligned} \quad (\text{A.14})$$

Finally, the total number of interaction is

$$n_{tot} \approx \frac{24}{\Theta^2} \frac{\log \left[\Theta (3N/4\pi)^{1/3} \right]}{\log[1 + \Theta]} + \frac{4\pi}{3\Theta^3}. \quad (\text{A.15})$$

For systems of interest N is large enough that $\Theta \geq (4\pi/3N)^{1/3}$, which means that the dominant behavior of equation A.15 for $\Theta > 0$ is given

$$n_{tot} \sim \frac{\log(N)}{\Theta^2}, \quad (\text{A.16})$$

hence the computation time required to calculate the electric field strength acting on one particle scales as $\sim \mathcal{O}(\log N)$. The calculation of all N particles of the system will then scale as $\sim \mathcal{O}(N \log N)$. The $N \log N$ -scaling is typically well obeyed for systems with $0.3 \leq \Theta \leq 1.0$. The case $\Theta = 0$ is equivalent to the direct particle-particle interaction method and therefore scales as $\sim \mathcal{O}(N^2)$. The case $\Theta \rightarrow \infty$ represents the other extreme and is called the particle-pseudo-particle method. It scales as $\sim \mathcal{O}(N)$.

Note that the above considerations assume an idealized sphere of particles with a homogeneous particle density. The sphere has to be large enough that border effects can be neglected. According to Hernquist [115], the $N \log(N)$ -scaling is well obeyed for various density profiles and geometries. Still, anything that leads to an unbalanced tree data structure, as e.g. spatial density fluctuations or realistic geometries, deteriorates the scaling and thereby reduces the performance.

Appendix B

Derivation of vicinity probability

The quantification of the particle correlation of strongly coupled plasmas can be performed by comparing the probabilities to find electrons close to ions with the uncorrelated limit. The uncorrelated case is obtained by uniformly spreading the electrons over the plasma volume. The volume contains N_i ions and N_e electrons. First, the ratio of detection to total volume has to be determined. The detection volume is given by spheres with a detection radius dr surrounding the ions. It is assumed that the atomic cluster has an fcc structure with an interatomic distance ia . As shown in figure B.1 an fcc unit cell contains 4 atoms ($6 \times 1/2$ atom and $8 \times 1/8$ atom). The side length of an fcc unit cell is

$$a = \sqrt{2} ia. \quad (\text{B.1})$$

The ratio of detection volume to total volume, which is the probability \bar{p}_i that an electron is in the vicinity of an ion, is given as

$$\bar{p}_i = \frac{V_d}{V_t} = \frac{4 \frac{4\pi}{3} dr^3}{a^3}. \quad (\text{B.2})$$

Assuming that the detection radius $dr = ia/4$ and inserting equation B.1 the following probability is obtained

$$\bar{p}_i = \frac{4 \frac{4\pi}{3} \left(\frac{ia}{4}\right)^3}{a^3} \quad (\text{B.3})$$

$$= \frac{\pi}{24\sqrt{2}} \quad (\text{B.4})$$

$$= 0.0925. \quad (\text{B.5})$$

The probability \bar{p}_o that an electron is outside of the detection volume is

$$\bar{p}_o = 1 - \bar{p}_i. \quad (\text{B.6})$$

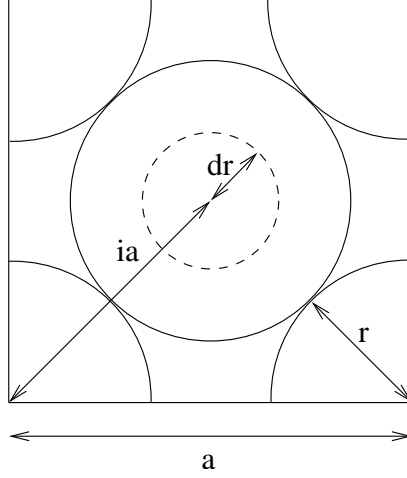


Figure B.1: Unit cell of an fcc structure with a side length a . The solid-line circle and quarter-circles represent the atoms. The dashed-line circle indicates the detection sphere. ia , r , and dr are the interatomic distance, the radius of an atom, and the detection radius, respectively.

The probability p_i that an electron is close to one particular ion is given as

$$p_i = \frac{\bar{p}_i}{N_i}. \quad (\text{B.7})$$

A decision tree as shown in figure B.2 can be used to derive the probability p_n that an electron is close to an ion which has $n - 1$ further electrons in its vicinity. At the root of the tree an electron has $N_i + 1$ possible paths. There are N_i ions it can be close to, which are indicated by $I1$ to IN_i , or it can be outside of all detection spheres. This path is labeled with O for *outside*. The probability to be close to a particular ion is p_i , the probability to be outside of all detection spheres is \bar{p}_o . The next electron starts one level deeper in the tree. This is shown by the combinations $I1I1, I1I2, \dots, I1IN_i, \dots, OIN_i, OO$. For a system with N_e electrons a tree with $(N_i + 1)^{N_e}$ leaves is created. In order to simplify the graphical representation a system containing 2 ions and 3 electrons is assumed. For each intermediate step the results obtained by this simple example are converted to a generalized form. Table B.1 shows all possible combinations of electrons and their locations. To get the number of electrons close to ion $I1$ which has no further electrons in its vicinity all rows with one and only one occurrence of $I1$ have to be found. The columns labeled with o indicate all these cases. The number of occurrences is given by the number of possible combinations $N_i^{N_e-1} = 2^2$ (which are $I1I2I2, I1I2O, I1OI2$, and $I1OO$) times the number of possible permutations for each combination which is $\binom{N_e}{n} = \binom{3}{1}$, where n stands for the number of electrons in the vicinity of the

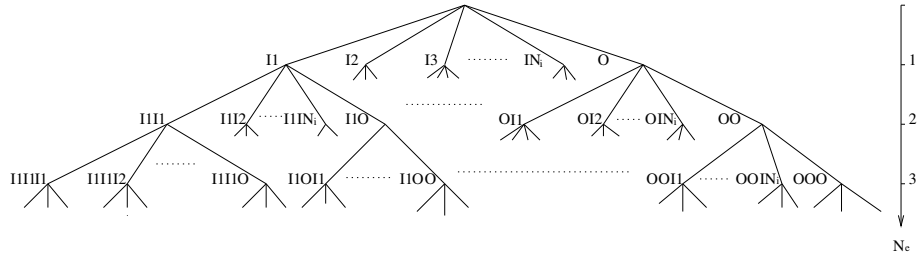


Figure B.2: Decision tree of a system containing N_i ions and N_e electrons. If an electron is close to an ion it walks one of the I -paths otherwise the O -path. The probability p_n can be calculated by evaluating all leaves of the tree.

considered ion. In order to get the total number for $(n = 1)$ -occurrences all ions have to be taken into account. This gives the number of occurrences as follows

$$o_n = N_i \binom{N_e}{n} N_i^{N_e-1} = N_i^{N_e} \binom{N_e}{n}. \quad (\text{B.8})$$

Table B.1: All possible leaves for a decision tree of a system with 2 ions and 3 electrons. The columns labeled with o indicate the occurrences of one and only one electron close to ion $I1$.

	o	1	2	3	o	1	2	3	o	1	2	3
		I1	I1	I1		I2	I1	I1		O	I1	I1
		I1	I1	I2	5	I2	I1	I2	9	O	I1	I2
		I1	I1	O	6	I2	I1	O	10	O	I1	O
		I1	I2	I1	7	I2	I2	I1	11	O	I2	I1
1		I1	I2	I2		I2	I2	I2		O	I2	I2
2		I1	I2	O		I2	I2	O		O	I2	O
		I1	O	I1	8	I2	O	I1	12	O	O	I1
3		I1	O	I2		I2	O	I2		O	O	I2
4		I1	O	O		I2	O	O		O	O	O

The above considerations did not take into account the probabilities of each occurrence. This can be easily done by examining all possible permutations and their probabilities as shown in Table B.2. As stated above, there are $\binom{N_e}{n}$ permutations per ion for a given n . In order to get the probability the number of permutations has to be multiplied by their probabilities and their number of occurrences. The probability of one occurrence as shown in Table B.2 is given as

$$p_i^n p_i^l \bar{p}_o^{N_e-n-l}, \quad (\text{B.9})$$

where l is the number of occurrences of electrons close to other ions and runs from 0 to $N_e - n$. All these probabilities have to be multiplied by the number of possible permutations and summed up

$$p_i^n \sum_{l=0}^{N_e-n} p_i^l \bar{p}_o^{N_e-n-l} (N_i-1)^l \binom{N_e-n}{l}. \quad (\text{B.10})$$

Taking into account that an n -occurrence contributes a fraction of n/N_e electrons to its probability the final equation for the probability is given as

$$p_n = \frac{n}{N_e} N_i \binom{N_e}{n} p_i^n \sum_{l=0}^{N_e-n} p_i^l \bar{p}_o^{N_e-n-l} (N_i-1)^l \binom{N_e-n}{l}. \quad (\text{B.11})$$

The evaluation of equation B.11 results in numbers which easily exceed the representation capability of regular programming languages. To overcome this obstacle the probability was calculated in Perl (Practical Extraction and Report Language) [116] using the modules `Math::Big`, `Math::BigInt` and `Math::BigFloat`, which can be downloaded from CPAN (Comprehensive Perl Archive Network) [117].

Table B.2: Permutations and their probabilities that one and only one electron is close to ion $I1$ for a system containing 2 ions and 3 electrons.

1	2	3			
I1	O	O	p_i	\bar{p}_o	\bar{p}_o
I1	I2	O	p_i	p_i	\bar{p}_o
I1	I2	I2	p_i	p_i	p_i

Appendix C

Common abbreviations

ADK	Ammosov-Delone-Krainov
ABI	Above Barrier Ionization
ATI	Above Threshold Ionization
CPAN	Comprehensive Perl Archive Network
CEI	Charge Enhanced Ionization
cgs	cm gramm second
CPU	Central Processing Unit
coc	Center of Charge
dc	direct current
DESY	Deutsches Elektronen-SYnchrotron
EII	Electron Impact Ionization
fcc	face centered cubic
FEL	Free electron laser
FORTTRAN	FORmular TRANslator
FWHM	Full Width Half Maximum
GHz	Giga Hertz
hcp	hexagonal closed packing
HPC	High Performance Computing
IBA	InfiniBand Architecture
IBH	Inverse Bremsstrahlung Heating
IBS	Inverse BremsStrahlung
IEEE	Institute of Electrical and Electronics Engineers
I/O	Input/Output
I_p	Ionization Potential
Laser	Light Amplification By Stimulated Emission of Radiation
LDH	Laser Dephasing Heating
MAC	Multipole Acceptance Criteria
MBR	Many-Body Recombination
MD	Molecular Dynamics
MHR	Many-body Recombination Heating

MPI	Message Passing Interface
MPIC	Microscopic Particle In Cell
NIST	National Institute for Standards and Technology
OFI	Optical Field Induced
OS	Operating System
PCI	Peripheral Component Interconnect
PEI	Polarization Enhanced Ionization
Perl	Practical Extraction and Report Language
PIC	Particle In Cell
SCI	Scalable Coherent Interconnect
SCP	Strongly Coupled Plasma
SI	System Internationale
SMP	Symmetric MultiProcessor
SPI	Single Photon Ionization
TOF	Time-of-Flight
UV	Ultra-Violet
VUV	Vacuum Ultra-Violet
XFEL	X-ray Free Electron Laser
XUV	eXtreme Ultra-Violet

Appendix D

Conversion table

	Atomic Units	SI
charge	1 a.u.	$1.6021917 \times 10^{-19}$ A s
mass	1 a.u.	9.109558×10^{-31} kg
length	1 a.u.	5.2918×10^{-11} m
time	1 a.u.	2.4189×10^{-17} s
electric potential	1 a.u.	27.210 V
electric field strength	1 a.u.	5.142×10^{11} V m ⁻¹
energy	1 a.u.	4.359×10^{-18} J
velocity	1 a.u.	2.1877×10^6 m s ⁻¹
momentum	1 a.u.	1.9926×10^{-24} kg m s ⁻¹
frequency	1 a.u.	4.1341×10^{16} s ⁻¹

	SI	cgs
charge	1 A s	2.998 statcoulomb
mass	1 kg	1000 g
length	1 m	100 cm
time	1 s	1 s
electric potential	1 V	1/299.8 statvolt
electric field strength	1 V m ⁻¹	1/29980 statvolt cm ⁻¹
energy	1 J	10 ⁷ erg
velocity	1 m s ⁻¹	100 cm s ⁻¹
momentum	1 kg m s ⁻¹	10 ⁵ g cm s ⁻¹
frequency	1 s ⁻¹	1 s ⁻¹

Appendix E

Physical constants

E.1 Atomic units

Constant	Symbol	Atomic Units
elementary charge	e	1 a.u.
electron rest mass	m_e	1 a.u.
Planck's constant	h	2π a.u.
Dirac's constant	\hbar	1 a.u.
velocity of light in free space	c	137.036 a.u.
permittivity of free space	ϵ_0	$1/(4\pi)$ a.u.
permeability of free space	μ_0	$4\pi/c^2$ a.u.
impedance of free space	Z_0	$4\pi/c$ a.u.

E.2 SI units

Constant	Symbol	SI
elementary charge	e	1.602×10^{-19} A s
electron rest mass	m_e	9.109×10^{-31} kg
Planck's constant	h	6.626×10^{-34} J s
Dirac's constant	\hbar	1.054×10^{-34} J s
Coulomb's constant	k_C	8.988×10^9 N m ² C ⁻²
velocity of light in free space	c	2.998×10^8 m s ⁻¹
permittivity of free space	ϵ_0	8.854×10^{-12} F m ⁻¹
permeability of free space	μ_0	$4\pi 10^{-7}$ H m ⁻¹
Boltzmann constant	k_B	1.381×10^{-23} J K ⁻¹
electron volt	eV	1.602×10^{-19} J
impedance of free space	Z_0	377 Ω

E.3 cgs units

Constant	Symbol	cgs	
elementary charge	e	4.803×10^{-10}	esu
electron rest mass	m_e	9.109×10^{-28}	g
Planck's constant	h	6.626×10^{-27}	erg s
Dirac's constant	\hbar	1.054×10^{-27}	erg s
velocity of light in free space	c	2.998×10^{10}	cm s ⁻¹
permittivity of free space	ϵ_0	1	(dimensionless)
permeability of free space	μ_0	1	(dimensionless)
Boltzmann constant	k_B	1.381×10^{-16}	erg K ⁻¹
electron volt	eV	1.602×10^{-12}	erg

List of Figures

1.1	Geometrical configuration of an Ar ₅₆₁ cluster.	4
1.2	Polarization of a spherical cluster in the presence of an electric field.	5
2.1	Position of electric and magnetic field values on a PIC grid box. .	9
2.2	Charged particles with square cross-section moving in simulation volume.	11
2.3	A moving particle creating an electric current on grid box surfaces.	12
2.4	Flow chart of a PIC simulation.	13
2.5	Schematic illustration of tunnel ionization.	14
2.6	Parallelizing MPIC-Code by dividing the simulation volume into equally sized subvolumes	16
2.7	2d point-to-point torus network	18
2.8	Flow chart of a treecode simulation.	20
2.9	Example of tree construction for a 2d simulation.	21
2.10	Fully constructed quad-tree according to figure 2.9 d.	22
2.11	Example of a recursive tree walk to update electric field strength.	23
2.12	Illustration of acceptance criterion.	24
2.13	Illustration of multipole expansion.	26
2.14	Displacement of multipole moments.	26
2.15	Idealized balanced binary tree showing the order of nodes for a non-recursive tree walk.	30
2.16	Comparison of a recursive and a non-recursive tree walk.	31
2.17	Box size depending shielding of MPIC codes.	34
2.18	Numerical heating in MPIC codes due to asymmetric potential energy.	35
3.1	Measured ion energy spectrum after Kumarappan et al. [87] . . .	38
3.2	Measured electron energy spectrum after Kumarappan et al. [88]	39
3.3	Electron and ion energy spectrum of an Ar ₁₀₀₀₀ cluster.	39
3.4	Electric field strength acting on the ions of an Ar ₁₀₀₀₀ cluster. . .	40
3.5	Illustration of polarization dephasing heating (PDH).	41
3.6	Charge state, position of ions, and electric field of an Ar ₁₀₀₀₀ cluster.	45
3.6	(continued)	46

4.1	Experimentally measured ion energy spectra for Ar ₄₀₀₀₀ clusters.	50
4.2	Comparison of experimentally and numerically obtained knee energies.	51
4.3	Simulated ion energy spectra for Ar ₄₀₀₀₀ clusters for different laser peak intensities.	52
4.4	Computed charge distribution of argon ions formed when Ar ₄₀₀₀₀ clusters are exposed to laser pulses with a pulse duration of 100fs and a wavelength of 806nm.	53
5.1	Schematic illustration of many-body recombination heating. . . .	57
5.2	Charge state distribution of a Xe cluster interaction with a XFEL pulse.	58
5.3	TOF mass spectra of ionization products of Xe ₁₅₀₀ clusters as a function of power density after Wabnitz et al. [103].	59
5.4	Plasma coupling parameters and ionized electrons as functions of time.	60
5.5	TOF mass spectra of ionization products for a power density of 2×10^{13} W/cm ² as a function of cluster size after Wabnitz et al. [103]	61
5.6	Schematic illustration of weakly and strongly coupled plasmas. . .	61
5.7	Electron vicinity probability for a Xe ₁₀₀₀ cluster.	62
5.8	Normalized electron vicinity probability for a Xe ₁₀₀₀ cluster. . . .	63
5.9	Energy absorption by Xe ₁₀₀₀ versus time for various heating mechanisms.	64
6.1	Current limits of treecodes and MPIC codes.	66
A.1	Illustration of $N \log(N)$ scaling of treecodes.	69
B.1	Unit cell of an fcc structure.	72
B.2	Decision tree of a system containing N_i ions and N_e electrons. . .	73

List of Tables

1.1	Classification of binding in clusters (from Reinhard and Suraud [10])	3
1.2	Structural data of condensed rare gases (from [14])	3
B.1	All possible leaves for a decision tree of a system with 2 ions and 3 electrons.	73
B.2	Permutations and probabilities for a system containing 2 ions and 3 electrons.	74

Bibliography

- [1] A. L. Schawlow and C. H. Townes. Infrared and Optical Masers. *Phys. Rev.*, 112:1940, 1958.
- [2] ECLIM European Conference on Laser Interaction with Matter, http://www.frascati.enea.it/XXVIIIEclim/the_eclim_conference.html.
- [3] S. Svanberg. Some applications of ultrashort laser pulses in biology and medicine. *Meas. Sci. Technol.*, 12:1777–1783, 2001.
- [4] S. Backus, C. G. Durfee III, M.M. Murnane, and H. C. Kapteyn. High power ultrafast lasers. *Rev. Sci. Instrum.*, 69:1207–1223, 1998.
- [5] D. Strickland and G. Mourou. Compression of amplified chirped optical pulses . *Optics Communications*, 56:219–221, 1985.
- [6] A. Fernandez, T. Fuji, A. Poppo, A. Fürbach, F. Krausz, and A. Apolonski. Chirped-pulse oscillators: a route to high-power femtosecond pulses without external amplification. *Optics Letters*, 29:1366–1368, 2004.
- [7] G. D. Reid, B. J. Whitaker, and K. Wynne. "Time Resolved Spectroscopy" in the "Handbook of Laser Technology". Institute of Physics Press, 2003.
- [8] Y. Jiang, L. Taewoo, and C. G. Rose-Petruck. Generation of ultrashort hard-x-ray pulses with tabletop laser systems at a 2-kHz repetition rate. *Optical Society of America Journal B*, 20:229–237, 2003.
- [9] K. W. Madison, P. K. Patel, M. Allen, D. Price, and T. Ditmire. Investigation of fusion yield from exploding deuterium-cluster plasmas produced by 100-TW laser pulses. *JOSA B*, 20:113–117, 2003.
- [10] P.-G. Reinhard and Eric Suraud. *Introduction to Cluster Dynamics*. John Wiley & Sons, Berlin; New York, 2004. ISBN 3-527-40345-0.
- [11] C. Jungreuthmayer, M. Geissler, Jürgen Zanghellini, and T. Brabec. Microscopic Analysis of Large-Cluster Explosion in Intense Laser Fields. *Phys. Rev. Lett.*, 92:133401, 2004.
- [12] J. Barnes and P. Hut. A hierarchical $O(N \log N)$ force-calculation algorithm. *Nature*, 324:446, 1986.

- [13] L. Bergmann, C. Schaefer, and W. Raith. *Lehrbuch der Experimentalphysik, Band 5, Vielteilchensysteme*. Walter de Gruyter, Berlin; New York, 1992. ISBN 3-110-10978-6.
- [14] J. Stapelfeldt. *CLULU: Ein neues Experiment für Fluoreszenzuntersuchungen an Edelgas-Clustern vom Dimer bis zum Mikrokristall*. PhD thesis, Universität Hamburg, 1990.
- [15] T. Brabec and F. Krausz. Intense few-cycle laser fields: Frontiers of nonlinear optics. *Rev. Mod. Phys.*, 72:545, 2000.
- [16] A. McPherson, T. S. Luk, B. D. Thompson, A. B. Borisov, O. B. Shiryaev, X. Chen, K. Boyer, and C. K. Rhodes. Multiphoton induced x-ray emission from Kr clusters on *M*-shell (~ 100 Å) and *L*-shell (~ 6 Å) transitions. *Phys. Rev. Lett.*, 72:1810, 1994.
- [17] T. Ditmire, J. Zweiback, V. P. Yanovsky, T. E. Cowan, G. Hays, and K. B. Wharton. Nuclear Fusion from Explosions of Femtosecond Laser-Heated Deuterium Clusters. *Nature (London)*, 398:489, 1999.
- [18] T. D. Donnelly, T. Ditmire, K. Neuman, M. D. Perry, and R. W. Falcone. High-order harmonic generation in atom clusters. *Phys. Rev. Lett.*, 76:2472, 1996.
- [19] I. Last and J. Jortner. Dynamics of coulomb explosion of large clusters in a strong laser field. *Phys. Rev. A*, 62:013201-1 – 013201-9, 2000.
- [20] <http://en.wikipedia.org/wiki/Plasma>.
- [21] V. P. Krainov and M. B. Smirnov. Cluster-beams in the super-intense femtosecond laser pulse. *Phys. Reports*, 370:237–331, 2002.
- [22] S. C. Rae and K. Burnett. Possible production of cold plasmas through optical-field-induced ionization. *Phys. Rev. A*, 46:2077, 1992.
- [23] N. H. Burnett and P. B. Corkum. Cold-plasma production for recombination extreme-ultraviolet lasers by optical-field-induced ionization. *J. Opt. Soc. Am. B.*, 6:1195, 1989.
- [24] P. Pulsifer, J. P. Apruzese, J. Davis, and P. Kepple. Residual energy and its effect on gain in a Lyman- α laser. *Phys. Rev. A*, 49:3958, 1994.
- [25] P. B. Corkum, N. H. Burnett, and F. Brunel. Above Threshold Ionization in the Long-Wavelength Limit. *Phys. Rev. Lett.*, 62:1259, 1989.
- [26] B. M. Penetrante and J. N. Bardsley. Residual energy in plasmas produced by intense subpicosecond lasers. *Phys. Rev. A*, 43:3100–3113, 1991.
- [27] M. V. Federov. *Atomic and Free Electrons in a Strong Light Field*. World Scientific Publishing Company, Singapore, 1998. ISBN 981022902X.

- [28] V. P. Krainov. Inverse stimulated bremsstrahlung of slow electrons under Coulomb scattering. *J. Phys. B: At. Mol. Opt. Phys.*, 33:1585–1595, 2000.
- [29] W. L. Kruer. *The Physics of Laser Plasma Interactions*. Addison-Wesley Publishing, 1998. ISBN 0-201-15672-5.
- [30] A. B. Langdon C. K. Birdsall. *Plasma Physics Via Computer Simulation*. Institute of Physics Publishing, Bristol; Philadelphia, 1991. ISBN 0-75030-117-1.
- [31] A. Pukhov. Three-dimensional electromagnetic relativistic particle-in-cell code vlpl (virtual laser plasma lab). *J. Plas. Phys.* 61, 61:425–433, 1999.
- [32] M. Eloy, R. Azambuja, J. T. Mendonça, and R. Bingham. High energy ions produced from cluster explosions. *Central Laser Facility Annual Report*, pages 67–70, 1999/2000.
- [33] J. Villasenor. Rigorous charge conservation for local electromagnetic field solvers. *Computer Physics Communications*, 69:306–316, 1992.
- [34] A. Taflove and S. C. Hagness. *Computational Electrodynamics: the finite-difference time-domain method*. Artech House, Norwood, MA 02062, 2nd edition, 2000. ISBN 1-58053-076-1.
- [35] Note that in the PIC/MPIC formalism a particle is represented by a finite sized box only for the calculation of the current density. For the solution of the relativistic equation of motion, particles are considered as point particles, represented by the center of gravity of their box.
- [36] J. D. Jackson. *Klassische Elektrodynamik*. Walter de Gruyter, Berlin; New York, 2nd edition, 1982. ISBN 3-11-009579-3.
- [37] M. V. Ammosov, N. B. Delone, and V. P. Krainov. Tunnel ionization of complex atoms and of atomic ions in an alternating electromagnetic field. *Sov. Phys.-JETP*, 64:1191, 1986.
- [38] X. M. Tong, Z. X. Zhao, and C. D. Lin. Theory of molecular tunneling ionization. *Phys. Rev. A*, 66:033402–1 – 033402–11, 2002.
- [39] G. L. Yudin and M. Y. Ivanov. Nonadiabatic tunnel ionization: Looking inside a laser cycle. *Phys. Rev. A*, 64:013409–1 – 013409–4, 2001.
- [40] P. Dietrich and P. B. Corkum. Ionization and dissociation of diatomic molecules in intense infrared laser fields. *J. Chem. Phys.*, 97:3187 – 3198, 1992.
- [41] M. Ya. Amusia: translation editor Ken Taylor. *Atomic Photoeffect*. Plenum Press, New York, NY, 1990. ISBN 0-306-43548-9.

- [42] W. Lotz. Electron-impact ionization cross-sections and ionization rate coefficients for atoms and ions from hydrogen to calcium. *Z. Phys.*, 216:241, 1968.
- [43] T. D. Märk and D. H. Gordon. *Electron Impact Ionization*. Springer Verlag, Vienna, 1985. ISBN 3-211-81778-6.
- [44] B. O'Rourke, F. J. Currel, H. Kuramoto, Y. M. Li, S. Ohtani, X. M. Tong, and H. Watanabe. Electron-impact ionization of hydrogen-like iron ions. *J. Phys. B: At. Mol. Opt. Phys.*, 34:4003–4013, 2001.
- [45] K. Ishikawa and Thomas Blenski. Explosion dynamics of rare gas clusters in an intense laser field. *Phys. Rev. A*, 62:063204–1 – 063204–11, 2000.
- [46] C. Rose-Petruck, K. J. Schafer, K. R. Wilson, and C. P. J. Barty. Ultrafast electron dynamics and inner-shell ionization in laser driven clusters. *Phys. Rev. A*, 55:1182–1190, 1997.
- [47] M. P. Allen and D. J. Tildesley. *Computer Simulation of Liquids*. Oxford University Press, Oxford, OX2 6DP, 1987. ISBN 0-19-855645-4.
- [48] G. C. Fox, R. D. Williams, and P. C. Messina. *Parallel computing works!* Morgan Kaufman Publishers Inc., San Francisco, CA, 1994. ISBN 1-558-60253-4.
- [49] M. Geissler. *Interaction of High Power Laser Pulses with Plasmas*. PhD thesis, Vienna University of Technology, 2000.
- [50] E. Langer. *Programmieren in Fortran*. Springer-Verlag, Wien; New York, 1993. ISBN 3-211-82446-4.
- [51] Fortran Standards Technical Committee. *Fortran77 and Fortran90 Standard*. <http://www.j3-fortran.org/>.
- [52] Message Passing Interface Forum, University of Tennessee, Knoxville, Tennessee. *MPI-2: Extensions to the Message-Passing Interface*, 1995-1997. <http://www.mpi-forum.org/>.
- [53] I. Foster. *Designing and building parallel programs: concepts and tools for parallel software engineering*. Addison-Wesly Publishing, 1995. ISBN 0-201-57594-9.
- [54] F. Hoffman. Using Derived Datas with MPI. *Linux Magazine*, April:42, 2003. available at <http://www.linuxmagazine.com/>.
- [55] F. Hoffman. MPI Communicators and Groups. *Linux Magazine*, May:42, 2003. available at <http://www.linuxmagazine.com/>.
- [56] F. Hoffman. MPI Communicators and Groups, Part 2. *Linux Magazine*, July:46, 2003. available at <http://www.linuxmagazine.com/>.

- [57] Top500.org. *Top500 List*, 1993-. <http://www.top500.org/>.
- [58] IEEE. *Std. 1596-1992 IEEE Standard for scalable coherent interconnect (SCI)*. http://standards.ieee.org/reading/ieee/std_public/description/busarch/1%596-1992_desc.html.
- [59] B. Finkbeiner. Knoten Kommunikation: High-Performance-Interconnects im Vergleich. *Linux Magazin*, Sonderheft 2:96–100, 2004. <http://www.linux-magazin.de>.
- [60] InfiniBand Trade Organisation, <http://www.infinibandta.org/>.
- [61] A.W. Appel. An efficient program for many-body simulation. *SIAM J. Sci. Stat. Comput.*, 85:85–103, 1985.
- [62] S. Pfalzner and R. Gibbon. *Many-body tree methods in physics*. Cambridge University Press, 40 West 20th Street, New York, NY 10011-4211, USA, 1996. ISBN 0-521-49564-4.
- [63] J. K. Salmon and M. S. Warren. Skeletons from the treecode closet. *J. Comp. Phys.*, 111:136–155, 1994.
- [64] G. A. Korn and T. M. Korn. *Mathematical handbook for scientists and engineers*. Dove Publications, Mineola, N. Y. 11501, 2000. ISBN 0-486-41147-8.
- [65] R. W. Hockney. The potential calculation and some applications. *Methods comput. Phys.*, 9:136–211, 1970.
- [66] J. E. Barnes. A modified tree code: don't laugh; it runs. *J. Comp. Phys*, 87:161–170, 1990.
- [67] L. Hernquist. Vectorization of tree traversals. *J. Comp. Phys.*, 87:137–147, 1990.
- [68] J. Makino. Vectorization of a treecode. *J. Comp. Phys.*, 87:138–160, 1990.
- [69] <http://www.ifa.hawaii.edu/~barnes/treecode/>.
- [70] G. M. Amdahl. Validity of the Single Processor Approach to Achieving Large-Scale Computing Capabilities. In *AFIPS Conference Proceedings*, volume 30, pages 483–485, Atlantic City, N.J., April 1967. AFIPS Press, Reston.
- [71] N. Milosevic, P. B. Corkum, and T. Brabec. How to Use Lasers for Imaging Attosecond Dynamics of Nuclear Procoesses. *Phys. Rev. Lett.*, 92:013002, 2004.
- [72] HPCVL, High Performance Computing Virtual Laboratory, <http://www.hpcvl.org>.

- [73] <http://www-unix.mcs.anl.gov/mpi/mpich/>.
- [74] LAM/MPI Parallel Computing, Indiana University, <http://www.lam-mpi.org/>.
- [75] D. Turner, S. Selvarahan, and X. Chen and W. Chen. The mp.lite message-passing library. In *Fourteenth IASTED International Conference on Parallel and Distributed Computing and Systems*, Cambridge Massachusetts, November 2002.
- [76] AMES Laboratory, http://www.scl.ameslab.gov/Projects/MP_Lite/.
- [77] National Institute for Standards and Technology, <http://physics.nist.gov/> and http://physics.nist.gov/cgi-bin/AtData/levels_form/.
- [78] T. A. Carlson, C. W. Nestor, N. Wasserman, and J. D. McDowell. Calculated ionization potentials for multiply charged ions. *Atomic Data*, 2:63, 1970.
- [79] A. V. Philippov, V. M. Povshev, A. A. Sadovoy, V. P. Shirkov, G. D. Shirkov, E. G. Vasina, and V. V. Vatulin. *Electron-Impact Ionization Cross Sections of Ti, Kr, Sn, Ta and U Atoms and their Ions in the Electric Energy Range from the Threshold up to 200 keV, Part 2*. Joint Institute for Nuclear Research, 2002.
- [80] K. Yamakawa, Y. Akahane, Y. Fukuda, M. Aoyama, N. Inoue, and H. Ueda. Ionization of many-electron atoms by ultrafast laser pulses with peak intensities higher than 10^{19}W/cm^2 . *Phys. Rev. A*, 68:065403, 2003.
- [81] H. Tawara and T. Kato. Ionization by electron impact. *Atomic Data Nuclear Data Tables*, 36:167, 1987.
- [82] Y. L. Shao, T. Ditmire, J. W. G. Tisch, E. Springate, J. P. Marangos, and M. H. R. Hutchinson. Multi-keV Electron Generation in the Interaction of Intense Laser Pulses with Xe Clusters. *Phys. Rev. Lett.*, 77:3343, 1996.
- [83] J. Kou, V. Zhakhovskii, S. Sakabe, K. Nishihara, S. Shimizu, S. Kawato, M. Hashida, K. Shimizu, S. Bulanov, Y. Izawa, Y. Kato, and N. Nakashima. Anisotropic Coulomb explosion of C_{60} irradiated with a high-intensity femtosecond laser pulse. *J. Chem. Phys.*, 112:5012, 2000.
- [84] C. Siedschlag and J. M. Rost. Electron Release of Rare-Gas Atomic Clusters under an Intense Laser Pulse. *Phys. Rev. Lett.*, 89:173401, 2002.
- [85] T. Ditmire, T. Donnelly, A. M. Rubenchick, R. W. Falcone, and M. D. Perry. Interaction of intense laser pulses with atomic clusters. *Phys. Rev. A*, 53:3379, 1996.
- [86] H. M. Milchberg, S. J. McNaught, and E. Parra. Plasma hydrodynamics of the intense laser-cluster interaction. *Phys. Rev. E*, 64:056402, 2001.

- [87] V. Kumarappan, M. Krishnamurthy, and D. Mathur. Asymmetric high-energy ion emission from argon clusters in intense laser fields. *Phys. Rev. Lett.*, 87:085005, 2001.
- [88] V. Kumarappan, M. Krishnamurthy, and D. Mathur. Asymmetric emission of high-energy electrons in the two-dimensional hydrodynamic expansion of large xenon clusters irradiated by intense laser fields. *Phys. Rev. A*, 67:043204, 2003.
- [89] M. Lezius, S. Dobosz, D. Normand, and M. Schmidt. Explosion Dynamics of Rare Gas Clusters in Strong Laser Fields. *Phys. Rev. Lett.*, 80:261, 1998.
- [90] T. Seideman, M. Yu. Ivanov, and P. B. Corkum. Role of Electron Localization in Intense-Field Molecular Ionization. *Phys. Rev. Lett.*, 75:2819, 1995.
- [91] T. Zuo and A. D. Bandrauk. Charge-resonance-enhanced ionization of diatomic molecular ions by intense lasers. *Phys. Rev. A*, 52:R2511, 1995.
- [92] T. Ditmire, R. A. Smith, J. W. G. Tisch, and M. H. R. Hutchinson. High Intensity Laser Absorption by Gases of Atomic Clusters. *Phys. Rev. Lett.*, 78:3121–3124, 1997.
- [93] V. Kumarappan, M. Krishnamurthy, and D. Mathur. Two-dimensional effects in the hydrodynamic expansion of xenon clusters under intense laser irradiation. *Phys. Rev. A*, 66:033203, 2004.
- [94] V. Kumarappan, M. Krishnamurthy, D. Mathur, and L. C. Tribedi. Effect of laser polarization on x-ray emission from Ar_n ($n = 200 - 10^4$) clusters in intense laser fields. *Phys. Rev. A*, 63:023203, 2001.
- [95] T. Ditmire, J. W. G. Tisch, E. Springate, M. B. Mason, N. Hay, R. A. Smith, J. Marangos, and M.H. R. Hutchinson. High-energy ions produced in explosions of superheated atomic cluster. *Nature (London)*, 386:54–56, 1997.
- [96] M. Schnürer, Ch. Spielmann, P. Wobrauschek, C. Streli, N. H. Burnett, C. Kan, K. Ferencz, R. Koppitsch, Z. Cheng, T. Brabec, and F. Krausz. Coherent 0.5-keV X-Ray Emission from Helium Driven by a Sub-10-fs Laser. *Phys. Rev. Lett.*, 80:3236–3239, 1998.
- [97] Ph. Zeitoun, G. Faivre, S. Sebban, T. Mocek, A. Hallou, M. Fajardo, D. Aubert, Ph. Balcou, F. Burgy, D. Douillet, S. Kazamias, G. de Lachze-Murel, T. Lefrou, S. le Pape, P. Mercere, H. Merdji, A. S. Morlens, J. P. Rousseau, and C. Valentin. A high-intensity highly coherent soft X-ray femtosecond laser seeded by a high harmonic beam. *Nature (London)*, 431:426–429, 2004.

- [98] S. Sebban, T. Mocek, D. Ros, L. Upcraft, Ph. Balcou, R. Haroutunian, G. Grillon, B. Rus, A. Klisnick, A. Carillon, G. Jamelot, C. Valentin, A. Rousse, J. P. Rousseau, L. Notebaert, M. Pittman, and D. Hulin. Demonstration of a Ni-Like Kr Optical-Field-Ionization Collisional Soft X-Ray Laser at 32.8 nm. *Phys. Rev. Lett.*, 89:253901, 2002.
- [99] M. Krishnamurthy, V. Kumarappan, and D. Mathur. Anisotropic "charge-flipping" acceleration of highly charged ions from clusters in strong optical fields. *Phys. Rev. A*, 69:033202, 2004.
- [100] Y. Fukuda, K. Yamakawa, Y. Akahane and M. Aoyama, N. Inoue, H. Ueda, and Y. Kishimoto. Optimized energetic particle emissions from Xe clusters in intense laser fields. *Phys. Rev. A*, 67:061201, 2003.
- [101] M. Hirokane, S. Shimizu, M. Hashida, S. Okada, S. Okihara, F. Sato, T. Iida, and S. Sakabe. Energy distributions of ions emitted from argon clusters Coulomb-exploded by intense femtosecond laser pulses. *Phys. Rev. A*, 69:063201, 2004.
- [102] G. Gibson, T. S. Luk, and C. K. Rhodes. Tunneling ionization in the multiphoton regime. *Phys. Rev. A*, 41:5049, 1990.
- [103] H. Wabnitz, L. Bittner, A. R. B. de Castro, R. Döhrmann, P. Gürtler, T. Laarmann, W. Laasch, J. Schulz, A. Swiderski, K. Von Haefen, T. Möller, B. Faatz, A. Fateev, J. Feldhaus, C. Gerth, U. Hahn, E. Saldin, E. Schneidmiller, K. Sytchev, K. Tiedtke, R. Treusch, and M. Yurkov. Multiple ionization of atom clusters by intense soft X-rays from a free-electron laser. *Nature*, 420:482, 2002.
- [104] T. Laarmann, A. R. B. de Castro, P. Gürtler, W. Laasch, J. Schulz, H. Wabnitz, and T. Möller. Interaction of Argon Clusters with Intense VUV-Laser Radiation: The Role of Electronic Structure in the Energy-Deposition Process. *Phys. Rev. Lett.*, 92:143401, 2004.
- [105] R. Santra and C. H. Greene. Xenon Clusters in Intense VUV Laser Fields. *Phys. Rev. Lett.*, 91:233401, 2003.
- [106] C. Siedschlag and J.-M. Rost. Small Rare-Gas Clusters in Soft X-Ray Pulses. *Phys. Rev. Lett.*, 93:043402-1, 2004.
- [107] S. Ichimura. *Basic principles of plasma physics*. Addison-Wesley Publishing, 1980.
- [108] A. Müller and A. Wolf. Production of antihydrogen by recombination of p with e^+ what can we learn from electron-ion collision studies? *Hyperfine Interactions*, 109:233, 1997.
- [109] F. Robicheaux and D. Hanson. Simulation of the Expansion of an Ultra-cold Neutral Plasma. *Phys. Rev. Lett.*, 88:055002, 1997.

- [110] S. Bergeson and T. Killian. Ultracold plasmas and Rydberg gases. *Physics World*, 16:37, 2003.
- [111] G. Zwicknagel, C. Toepffer, and P.-G. Reinhard. Molecular dynamic simulation of ions in electron plasmas at strong coupling. *Hyperfine Interactions*, 99:285, 1996.
- [112] private communication Thomas Möller.
- [113] D. G. Yakovlev, O. Y. Gnedin, and A. Y. Potekhin. Strongly coupled Coulomb and nuclear plasma in inner crusts of neutron stars. *Contrib. Plasma Phys.*, 41:227, 2001.
- [114] I. Zahed. The quark-gluon plasma at strong coupling. *J. Phys. G*, 30:S1267, 2004.
- [115] L. Hernquist. Hierarchical N -Body methods. *Comp. Phys. Commun.*, 48:107–115, 1988.
- [116] <http://www.perl.org/>.
- [117] <http://www.cpan.org/>.

Curriculum Vitae

EUROPEAN CURRICULUM VITAE FORMAT



PERSONAL INFORMATION

Name	Christian JUNGREUTHMAYER
Address	Gugitzgasse 6/12/2, Wien, A-1190, Austria, EU
Telephone	+43-1-320 65 87
E-mail	christian.jungreuthmayer@tuwien.ac.at
Nationality	Austrian
Date of Birth	25. August 1972

WORK EXPERIENCE

- Dates (from-to) March 2002 - present
- Name and address of employer Photonics Institute, Vienna University of Technology
Gusshausstrasse 27/387, A-1040 Wien, Austria, EU
- Occupation or position held Ph.D. student
- Dates (from-to) September 2002 - December 2004
- Name and address of employer Department of Physics, University of Ottawa
150 Louis Pasteur, Ottawa, ON, K1N 6N5, Canada
- Occupation or position held Research Associate
- Dates (from-to) April 1999 - April 2002
- Name and address of employer PSE, Siemens AG Österreich
Gudrunstrasse 11, A-1100, Wien, Austria, EU
- Occupation or position held Project Manager and Software Designer
- Dates (from-to) April 1998 - March 1999
- Name and address of employer FZA, Telekom Austria AG
Arsenal, Object 24, A-1030 Wien, Austria, EU

- Occupation or position held | System Engineer
 - Dates (from-to) | October 1991 - May 1992
- Name and address of employer | Sozialhilfeverband Grieskirchen
Manglborg 14, A-4710 Grieskirchen, Austria, EU
- Occupation or position held | Civil Service

EDUCATION AND TRAINING

- Dates (from-to) | March 2002 - present
 - Name and type of organization providing education and training | Vienna University of Technology, Austria
Faculty of Electrical Engineering and Information Technology
 - Principal subjects | Ph.D. student, numerical physics
- Dates (from-to) | October 1992 - December 1997
 - Name and type of organization providing education and training | Vienna University of Technology, Austria
Faculty of Electrical Engineering and Information Technology
 - Principal subjects | Automation Technology and Control Engineering
 - Title of qualification awarded | *Dipl.-Ing.* (MSc) in electrical engineering
- Dates (from-to) | February 1997 - August 1997
 - Name and type of organization providing education and training | University of Liverpool, UK
Faculty of Mechanical Engineering
 - Principal subjects | Rapid Prototyping
- Dates (from-to) | September 1986 - July 1991
 - Name and type of organization providing education and training | *HTL* (High School for Technology), Braunau/Inn, Austria
 - Principal subjects | Communication Engineering and Computer Science
 - Title of qualification awarded | *Matura* (school leaving examination)

ADDITIONAL INFORMATION

Publications

Book Chapters

A. Pegarkov, J. Zanghellini, C. Jungreuthmayer, and T. Brabec
Ionization dynamics of multi-electron systems in strong laser pulses
Chapter for 'Focus on Laser and Electro-Optics Research', edited by
W. Arkin (Nova Science Publishers, to be published 2005).

Scientific Journals

C. Jungreuthmayer, L. Ramunno, J. Zanghellini, and T. Brabec
Plasma physics in the strong coupling regime:
Intense soft x-ray cluster interaction
Physical Review Letters, submitted

M. Krishnamurthy, J. Jha, D. Mathur, C. Jungreuthmayer,
L. Ramunno, J. Zanghellini, and T. Brabec
*Charge state distribution of ions formed in Coulomb explosions of
Argon clusters in intense laser fields*
Physical Review A, submitted

J. Zanghellini, C. Jungreuthmayer, A. Pegarkov, and T. Brabec
Multi-electron signatures of high harmonic generation
Physical Review Letters, submitted

M. Kitzler, J. Zanghellini, C. Jungreuthmayer, M. Smits,
A. Scrinzi, and T. Brabec
Ionization dynamics of extended multielectron systems
Physical Review A, Vol 70, 041401, 2004

C. Jungreuthmayer, M. Geissler, J. Zanghellini, and T. Brabec
*Microscopic analysis of large-cluster explosion in intense laser
fields*
Physical Review Letters, Vol 92, pp. 133401-1, 2004

Conference Proceedings

C. Jungreuthmayer, N. Milosevic, and T. Brabec
Atoms and Clusters in Relativistic Laser Fields
Proceedings of the International Symposium for Topical Problems of
Nonlinear Wave Physics 2003
NWP 2003, Nizhny Novgorod, Russia
<http://www.nwp.sci-nnov.ru/>

P. Erasenthiran, C. Jungreuthmayer, R. Ball, W. O'Neill,
and W. M. Steen
Laser step shaping for laminated object manufacturing parts
Proceedings of the 1997 Laser Materials Processing Conference,
ICALEO'97. Part 2 (of 2), Vol 82, pp.E84-E92
San Diego, CA, USA. 19971117-19971120
http://home.att.net/~edgrenda/p98/p98_126.htm

P. Erasenthiran, C. Jungreuthmayer, W. O'Neill, and W.M. Steen
*An Investigation of Step Shaping Using Nd:YAG Laser for Parts
Produced by Laminated Object Manufacturing*
Proc. of Laser Assisted Net Shape Engineering 2 (LANE'97),
Erlangen, Germany, 1997, pp.541-554.
[http://www.lft.uni-erlangen.de/SEITEN/LANE/
1997/lane97_inhalt.shtml](http://www.lft.uni-erlangen.de/SEITEN/LANE/1997/lane97_inhalt.shtml)

Poster Presentations

M. Krishnamurthy, J. Jha, C. Jungreuthmayer, L. Rammuno,
J. Zanghellini, T. Brabec, and D. Mathur
*Charge state distribution of ions formed in Coulomb explosions
of clusters in intense laser fields*
International Symposium of Ultrafast Intense Laser Science 3
September 16-20, 2004, Palazzo Steri and Citta del Mare, Sicily, Italy
<http://www.isuils.jp>

Oral Presentations

C. Jungreuthmayer, J. Zanghellini, L. Ramunno, and T. Brabec
*Plasma physics in the strong coupling regime: Intense soft x-ray
cluster interaction*
High-Field Attosecond Physics
January 9-15, 2005, Obergurgl, Austria
<http://www.mbi-berlin.de/heraeus340/>

L. Ramunno, C. Jungreuthmayer, and T. Brabec
Classical many particle dynamics: from clusters to solids
2004 Cross Border Workshop on Laser Science:
From Nonlinear Optics to Biophotonics
May 2004, Ottawa, Canada
<http://www.crossborderworkshop.org/sched.html>

C. Jungreuthmayer, N. Milosevic, and T. Brabec
Canadian Association of Physicists Annual Congress 2003
June 2004, Charlottetown, Prince Edward Island, Canada
<http://www.cap.ca/andhttp://www.upei.ca/~cap2003/>

C. Jungreuthmayer, M. Geissler, and T. Brabec
Laser Induced Plasma Physics
High Performance Computing Virtual Laboratory (HPCVL) Symposium
November 2002, Ottawa, Canada
http://www.hpcvl.org/announcements/symp_ann_301102.html